

ABRASIVE TOOL WEAR IN METAL FORMING PROCESSES

Marc Masen

The research in this thesis is sponsored within the framework of the Innovation Directed Research Programme on Surface Technology (IOP-Oppervlaktetechnologie), by the Netherlands Ministry of Economic Affairs.

De promotiecommissie is als volgt samengesteld:

prof.dr.ir. H.J. Grootenboer, Universiteit Twente, voorzitter en secretaris
prof.dr.ir. D.J. Schipper, Universiteit Twente, promotor
dr.ir. M.B. de Rooij, Universiteit Twente, assistent promotor
prof.dr.ir. A. de Boer, Universiteit Twente
prof.dr.ir. R. Akkerman, Universiteit Twente
prof.dr. L. Katgerman, Technische Universiteit Delft
prof.dr.ir. M. Vermeulen, Universiteit Gent

Masen, Marc Arthur
ABRASIVE TOOL WEAR IN METAL FORMING PROCESSES
Ph.D. Thesis, University of Twente, Enschede, The Netherlands
September 2004

ISBN 90-365-2061-4

Keywords:

tribology, surface technology, metal forming, abrasive wear, coatings,
tailor welded blanks, deep drawing

Copyright © 2004 by M.A. Masen, Hengelo, The Netherlands
Printed by Febo druk B.V., Enschede, The Netherlands

ABRASIVE TOOL WEAR IN METAL FORMING PROCESSES

PROEFSCHRIFT

ter verkrijging van
de graad van doctor aan de Universiteit Twente,
op gezag van de rector magnificus,
prof. dr. F.A. van Vught,
volgens besluit van het College voor Promoties
in het openbaar te verdedigen
op woensdag 15 september 2004 om 15.00 uur

door

Marc Arthur Masen

geboren op 28 december 1975
te Hengelo

Dit proefschrift is goedgekeurd door:

de promotor: prof. dr. ir. D.J. Schipper

de assistent promotor: dr. ir. M.B. de Rooij

Samenvatting

De standtijd van een gereedschap is een belangrijke parameter bij industriële metaal-omvorm processen. De standtijd wordt bepaald door de eisen aan het product; wanneer het uiteindelijke product vormafwijkingen vertoont of de oppervlaktekwaliteit onvoldoende is, dient het gereedschap gerepareerd of vervangen te worden. Recente ontwikkelingen, waaronder het omvormen van niet-conventionele materialen en het verminderd gebruik van smeermiddelen, veroorzaken een zware belasting van het gereedschap en daarmee een reductie van de standtijd. Een voorbeeld is abrasieve slijtage van het gereedschap tijdens het omvorm proces als gevolg van het ploegen en krassen van harde deeltjes van het te vervormen material door het gereedschap.

In dit werk is een model beschreven dat deze abrasieve slijtage van het gereedschap kwantificeert. Het model is opgebouwd vanuit het niveau van oppervlakteruwheid. De micro-geometrie van zowel het abrasieve oppervlak als het gereedschap wordt gemeten, bijvoorbeeld met een interferometer. Op basis van deze data wordt de geometrie in elk van de micro-contacten benaderd met behulp van een kegelvormig danwel paraboloïdevormig lichaam. Het gedrag van zo'n asperity, of ruwheidstop, in contact met een deformerend tegenlichaam is beschreven in een elastisch-elastoplastisch-plastisch contactmodel. Met behulp van experimenten is de abrasieve slijtage van model-ruwheidstoppen bestudeerd, en deze resultaten zijn vastgelegd in een empirisch model. De sommatie van alle ruwheidstoppen in het contact geeft vervolgens de abrasieve slijtage in het contact tussen ruwe oppervlakken.

Het ontwikkelde model onderscheidt zich van conventionele slijtagemodellen door nieuwe elementen, zoals het elastisch-elastoplastisch-plastische model voor glijdende contacten en de deterministische modellering van micro-contacten, waardoor het groeien en fuseren van ruwheidstoppen met toenemende belasting wordt beschreven. De deterministische benadering is ook noodzakelijk voor het correct beschrijven van het abrasieve slijtage proces.

Het model is toegepast op de slijtage van gietijzeren gereedschappen bij het omvormen van tailor welded blanks. De resultaten van het model komen overeen met experimentele resultaten. Tevens is aangetoond dat het toepassen van een harde oppervlaktelaag op het gereedschap niet noodzakelijkerwijs leidt tot een verbetering van de weerstand tegen slijtage. Het toegepaste gereedschapsmateriaal bij dieptrekken, nodulair gietijzer, is namelijk slecht te coaten. Het toepassen van tussenlagen kan de weerstand tegen slijtage verhogen. Het ontwikkelde model kan tevens toegepast worden op andere processen waarbij abrasieve slijtage een belangrijke rol speelt, bijvoorbeeld bij extrusie van aluminium en magnesium legeringen.

Summary

Tool-life is an important parameter in industrial metal forming processes and is determined by demands and requirements of the product; when the final product shows deviances in shape or the surface quality is insufficient, the tool needs to be refurbished or replaced. Recent developments, among other things the processing of non-conventional materials and the reduced use of lubricants result in a more severe load on the tool and therefore in a decrease of the tool-life. An example is abrasive wear of the tool during the forming operation hard particles of the deforming product plough and scratch through the tool surface.

In this work a model is presented that quantifies this abrasive tool wear. The foundation of the model is on the level of surface roughness. The surface micro-geometry of both the abrasive surface and the wearing tool are measured using an interferometer. Based on this data, the surface geometry in each of the micro-contacts is represented using a so-called asperity. Such an asperity has either a conical or a paraboloidal shape and is fitted through the surface geometry. The behaviour of an asperity, or summit, in contact with a deforming counter surface is described in an elastic-elastoplastic-plastic contact model. Using experiments, the abrasive wear of model-summits is studied. These results are embedded in an empirical model. The summation over all the summits in contact finally results in the abrasive wear behaviour in the contact of rough surfaces.

The developed model distinguishes itself from conventional abrasive wear models by new elements, such as the elastic-elastoplastic-plastic model for sliding contacts and the deterministic modelling of micro-contacts, which enables describing the growth and merger of asperities with increasing load. Furthermore, the deterministic approach is required for a correct description of the abrasive wear process.

The model is applied to the wear of cast iron tools in the processing of tailor welded blanks. The results of the model agree with experimental results. Also it is shown that the application of a hard surface layer does not necessarily result in an increased resistance to abrasive wear, as the applied tool material in deep drawing operations is inhomogeneous and therefore quite difficult to apply a coating to. The application of intermediate layers can increase the wear resistance. The developed model can as well be applied to other processes where abrasive wear plays a significant role, for example in extrusion of aluminium and magnesium alloys.

Contents

Chapter 1	Introduction	1
1.1	Wear	1
1.2	Sheet-metal forming.....	2
1.3	Deep drawing.....	3
1.4	Tool life in deep drawing.....	4
1.5	Extending tool life	7
1.6	Objective of this research.....	8
1.7	This thesis	8
Chapter 2	Deep Drawing and Tribology	11
2.1	Tribological system	11
2.2	Systems approach in Tribology.....	15
2.3	Tribology: contact, friction, lubrication and wear.....	16
2.4	Tribology of the deep drawing process	24
Chapter 3	Single Asperity Contact	27
3.1	Introduction.....	27
3.2	Static versus sliding contact.....	28
3.3	Discussion and conclusions.....	48
Chapter 4	Single Asperity Abrasive Wear	53
4.1	Introduction.....	53
4.2	Modelling abrasive wear	54
4.3	SEM experiments.....	62
4.4	Implementation.....	77
4.5	Discussion.....	81
Chapter 5	Modelling Contact and Abrasive Wear of Real Surfaces.....	83
5.1	Introduction.....	83
5.2	Contact of rough surfaces	84
5.3	Deterministic approach.....	85
5.4	Results of the deterministic model.....	91
5.5	Discussion.....	107
Chapter 6	Abrasive Wear in Deep Drawing of Tailor Welded Blanks	109
6.1	Introduction.....	109
6.2	Deep drawing simulations	109
6.3	Improving the wear resistance in deep drawing	115
6.4	Discussion.....	120
Chapter 7	Conclusion.....	123
7.1	Introduction.....	123
7.2	Overview of the developed model	123
7.3	Conclusions.....	124
7.4	Recommendations	127

Appendix A	Material properties.....	133
Appendix B	Contact.....	137
B.1	Static contact	137
B.2	Explicit equations for sliding contact	152
B.3	Greenwood and Williamson parameters	157
Appendix C	Photographic impressions of the experimental set-ups.....	159
C.1	SEM tribo-system	159
C.2	Deep drawing simulator.....	161

Symbols

Roman symbols

A	Contact area	[m ²]
A_n	Nominal or apparent contact area	[m ²]
A_r	Real contact area	[m ²]
A_f	Frontal area	[m ²]
A_g	Frontal area of wear groove	[m ²]
A_s	Frontal area of shoulders	[m ²]
a	Contact radius	[m]
C	Number of contacting asperities	[-]
c	Shape factor	[-]
D_p	Asperity degree of penetration	[-]
d	Indentation depth	[m]
E_i	Young's modulus of solid i	[Pa]
E_*	Reduced Young's modulus	[Pa]
E_c	Effective Young's modulus	[Pa]
E	Elliptic integral of the second kind	
f	Fraction of asperities	[-]
f_r	Relative contact shear strength	[-]
H	Hardness	[Pa]
h	Separation between surfaces in contact	[m]
I_0	Weighing function for effective Young's modulus	[-]
I_1	Weighing function for effective Young's modulus	[-]
J_2	Equivalent Von Mises stress	[Pa]
K	Archard wear coefficient	[-]
K	Elliptic integral of the first kind	
k	Specific wear rate	[m ³ ·N ⁻¹ ·m ⁻¹]
k	Average contact pressure factor	[-]
k	Bulk shear strength of soft surface	[Pa]
L	Sliding distance	[m]
m	Elliptic integral parameter	[-]
N	Normal contact load	[N]
n	Asperity density	[m ²]

Roman symbols, continued

p	Pressure	[Pa]
p_0	Nominal contact pressure	[Pa]
R	Asperity radius	[m]
R_a	CLA surface roughness parameter	[m]
R_q	RMS surface roughness parameter	[m]
S_{ep}	Relative size of elastoplastic deformation regime	[-]
T	Tangential load	[N]
t	Layer thickness	[m]
V	Volume	[m ³]
V_i	Volumetric wear due to i-th asperity	[m ³]
v	Velocity	[m·s ⁻¹]
W	Work involved in plastic deformation	[N·m]
w	Width of wear groove	[m]
x'	Sliding direction	[-]
z	Surface micro-geometry height	[m]

Greek symbols

α	Dimensionless radius of contact spot	[-]
β	Orientation of asperity w.r.t. the sliding direction	[rad]
Γ	Relative depth of layer	[-]
γ	Dimensionless normal approach of two bodies	[-]
δ	Relative elastoplastic indentation depth	[-]
ε	Strain	[-]
ζ	Elastoplastic recovery angle	[rad]
η	Dynamic viscosity	[Pa·s]
θ	Asperity top angle	[-]
κ	Ellipticity ratio or aspect ratio of contact area	[-]
λ	Gap curvature ratio	[-]
μ	Coefficient of friction	[-]
ν	Poisson's ratio	[-]
Ξ	Rule of mixtures coefficient	[-]
ξ	Asperity degree of wear	[-]
ρ	Density	[kg·m ⁻³]
σ	Asperity standard deviation	[m]
σ	Stress	[Pa]
σ_u	Ultimate stress	[Pa]

Greek symbols, continued

σ_y	Yield stress	[Pa]
τ	Shear strength of the interface	[Pa]
τ	Shear stress	[Pa]
φ	Asperity attack angle	[-]
$\varphi(s)$	Asperity height distribution	[m]
Ψ	Volumetric wear per unit sliding distance	[m ³ ·m ⁻¹]
ψ	Elliptic integral parameter	[-]

Other symbols

L	Dimensionless lubrication number	[-]
\mathcal{A}	Surface deformation index	[-]

Suffixes

asp	single asperity contact
avg	average value
calc	calculated result
c	cutting model of wear
det	deterministic model
dyn	dynamic or sliding contact
e	elastic
ep	elastoplastic
e,trans	transition, limit of pure elastic behaviour and onset of plasticity
exp	experimentally obtained result
i	<i>i</i> -th asperity
m	micro-contact
max	maximum value
min	minimum value
p	plastic
p	ploughing type of wear
p,trans	transition, onset of fully plastic material behaviour
st	calculated using statistic model
stat	static
w	wedge formation type of wear
x	in x-direction
y	in y-direction
*	combined parameter, composed of multiple parameters

Abbreviations

BL	Boundary Lubrication
CVD	Chemical Vapour Deposition
CrN	Chromium Nitride
DLC	Diamond Like Carbon
EHL	Elasto-Hydrodynamic Lubrication
FEM	Finite Element Method
FFL	Full Film Lubrication
GW	Greenwood-Williamson
MC	Metal-Carbon
ML	Mixed Lubrication
PHL	Plasto-Hydrodynamic Lubrication
PVD	Physical Vapour Deposition
SEM	Scanning Electron Microscope
St	Stellite®, Cobalt based alloy
TiN	Titanium Nitride
Ult	Ultimet®, Cobalt based alloy

Chapter 1

Introduction

1.1 Wear

A famous Dutch saying goes "*Zo oud als de weg naar Rome*". Its verbatim translation would be "As old as the road to Rome" which literally applies to wear and wear processes. This is indicated in Fig. 1.1(a) showing cart tracks worn into a paved Roman road in the ancient city of Pompeii. Although historians argue that sometimes tracks might be intentionally carved in the pavement to provide guidance of the vehicles, it is well known that the wheels of carts were covered with metal hoops or nails to prevent them from wearing (see e.g. Dowson [33] and Landels [69]).



(a)
cart tracks in an ancient Roman road,
from Klischat [67]



(b)
nail-studded wheel, 2500 B.C.,
from Dowson [33]

Fig. 1.1: Wear of road pavement due to wear protection on wheels.

An uninvited consequence of these metal wheel reinforcements, as shown in Fig. 1.1(b), was the resulting wear of the pavement of the road. Dowson [33] notes that in the middle ages some vehicles were banned from towns because the hard metal wheels abraded the roads.

Abrasive wear can be defined as the wear of a body due to the sliding interaction with a harder body. This harder body can be either a rough counter surface, like a rock that (hopefully not) cuts through the rope of a mountaineer, a particle that is entrapped in the contact, for instance soot between the liner and the piston in a combustion engine or a large collection of hard particles such as the teeth of ground-displacement machines after some period of use. Abrasion is also used in manufacturing processes as in filing, sanding and grinding, where the hard tool removes material from the work piece.

This thesis focuses on the abrasive wear of tools used in sheet-metal forming processes. In the first two chapters some basic concepts and backgrounds concerning this topic are presented.

1.2 Sheet-metal forming

Sheet-metal forming is the generic term for a number of manufacturing processes in which a product is formed by plastic deformation of a sheet, without any material removal. Some examples of sheet-metal forming processes are stretch forming, bending, hydro-forming and deep drawing. In comparison with manufacturing processes as casting, powder metallurgy and forging, sheet-metal forming processes offer the possibility of a comparatively complex product geometry, a high production rate and relatively low product weight against low costs. This explains the popularity of sheet-metal forming processes in modern series production.



Fig. 1.2: Two examples of sheet-metal products: a soup can (painted by Andy Warhol) and the body-work of a Mercedes 300SL.

Sheet-metal forming techniques were already applied in ancient times, for instance in the manufacturing of knight's suits of armour. Industrial sheet-metal forming finds its origin in the mid-eighteen hundreds, when stamping of tin plate for the production of food containers was the first large scale application of sheet-metal [97]. During the twentieth century the ever increasing production of automobiles, domestic appliances like refrigerators and washing machines and the packaging industry (see Fig. 1.2) led to a rapid growth of the sheet-metal forming industry.

1.3 Deep drawing

One of the most common sheet-metal forming processes is deep drawing. The principle of the deep drawing process is illustrated in Fig. 1.3, showing the forming of a simple cylindrical cup. As deep drawing products usually are characterised by a relatively complex geometry, this simple shape involves a rather coarse approximation, however it facilitates an explanation of the principle of the deep drawing process.

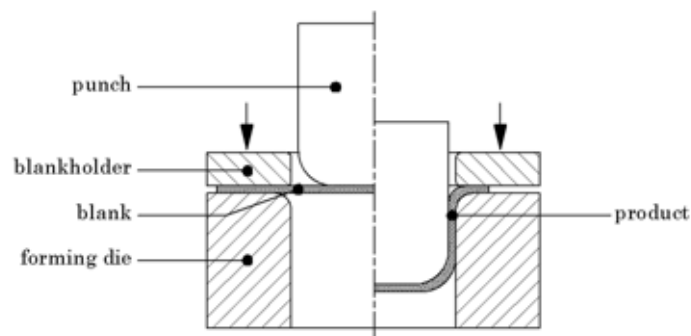


Fig. 1.3: Principle of the deep drawing process.

In deep drawing the final product is formed using three tools: a punch, a forming die and a blank holder. The geometry of the product is contained in the punch and the forming die. The flat blank is placed between these tools and is held in position using the blankholder, which prevents wrinkling of the sheet. As the punch closes, the blank is forced into the die cavity and a cup is formed.

Because the product geometry is contained in the tools, for each product a unique set of tools is required, making deep drawing unsuited for relatively small series. In most deep drawing operations the complex geometry of the final product requires a sequence of draws. A typical car body-panel is manufactured on a press line of about five presses, where loading, transport and unloading of the sheets is automated using robot arms.



Fig. 1.4: Schematic illustration of a deep drawing press line.

1.4 Tool life in deep drawing

Inherent to the deep drawing process is the repeated sliding contact between the blank and the tools. This results in friction and energy losses, as well as in wear of both the blank and the tools. The latter might result in inferior surface finish of the final product. Besides that, geometrical deviations of the final product may occur in advanced stages of tool wear.

After a number of formed products, the tool wear exceeds a certain tolerated level and the tool needs to be refurbished. The number of products manufactured before tool maintenance is required is called the tool life. It needs no explanation that a long tool life is economically interesting, as it decreases press down time and overhaul costs.

Recent developments in industrial deep drawing lead to an increased severity of the contact conditions or decreased wear resistance of the tool materials and hence a decrease in tool life. Some examples of these trends are:

- The reduced use of lubricants
- The application of alternative tool materials
- The forming of products with a relatively hard surface

1.4.1 Reduced use of lubricants

Plain sheet-metal is protected against corrosion by a layer of corrosion preventive oil. Prior to the deep drawing process this protective layer is removed and the surface of the blank is covered with deep drawing oil, which ensures a well lubricated contact between blank and tools during the forming process. Subsequently, after the forming process, the lubricant is removed and a new layer of corrosion preventive is applied to the sheet surface. A recent trend is a change to so-called pre-lubes, i.e. corrosion preventive oils that also have some lubrication properties and therefore do not require the application of an additional deep drawing oil. As a result, the cleaning steps can be eliminated, which means a decrease in costs. Furthermore the use of environmentally harmful detergents is reduced, making the application of

pre-lubes interesting from an economical as well as an ecological point of view. However, the downside is an increased severity of the contact situation, as the lubrication performance of these pre-lubed corrosion preventive oils is not as good as that of real deep drawing oils.

1.4.2 Alternative tool materials

In general, deep drawing tools are made of high grade nodular cast iron, a material that excels in impact resistance and wear resistance, but is difficult to cast without inclusions or porosity. Furthermore the machinability of nodular cast iron is not very good. Therefore these cast iron tools are quite expensive. As deep drawing is particularly suited for application in mass production, the high costs of the deep drawing tool can be divided over a large number of products, making the tooling costs per product relatively low.

Nowadays, car manufacturers tend to produce a larger diversity of models and versions, resulting in a larger number of smaller volume series. Therefore tools that are made of more inexpensive materials become economically interesting and moreover, as these series are produced during a smaller time span, tool materials enabling shorter tool development times are required.

Examples of such alternative tool materials are low grade cast iron, wood, plaster, plastics and metals with a low melting point, see also van der Heide et al. [106],[107], Müller and Sladojevic [81] and Nakagawa [82]. A problem with these alternative materials is their lower wear resistance under deep drawing conditions.

1.4.3 Forming of products with relatively hard surface layers

Another development in sheet-metal forming practice that results in increased wear of the tool material is the processing of materials with a relatively hard surface layer. During the forming operation of the sheet product, hard asperities on the sheet penetrate into and scratch through the softer tool material, causing wear. Some examples relating to practical industrial applications are:

- Aluminium sheet
Because of its high strength to weight ratio, aluminium is becoming more popular in the automotive industry. Aluminium sheet is covered with a dense layer of aluminium-oxide (Al_2O_3), which has a high hardness of about 15 GPa. Well known product examples are the full aluminium body Audi A2 and A8. Also other car manufacturers are increasingly applying aluminium body panels.
- Hot rolled sheet
Like aluminium sheet, hot rolled sheet is covered with a hard oxide layer, that scratches through the softer tool. Typical applications of hot rolled sheet are in the manufacturing of pressure vessels, tanks and silo's.

- Galvanealed sheets
Galvanealed sheets have a relatively soft zinc surface layer, in which hard particles are embedded. Again, these hard particles penetrate into the tool and cause scratching. Automotive body parts are often galvanealed.
- Tailor welded blanks
Tailor welded blanks or pre-welded blanks are blanks that are composed of several smaller blanks, which may differ in properties, like sheet thickness or material. Two examples are shown in Fig. 1.5, representing (a) the left and right hand side inner wheelhouse of a car [104] and (b) the inner front of a door. The wheel housing blank is composed of four sheets that are welded together. The housing itself is made of relatively thin sheet material, while some parts are reinforced using thicker sheets. The front part of the door as shown in Fig. 1.5(b) also is composed of two sheets with a different thickness.

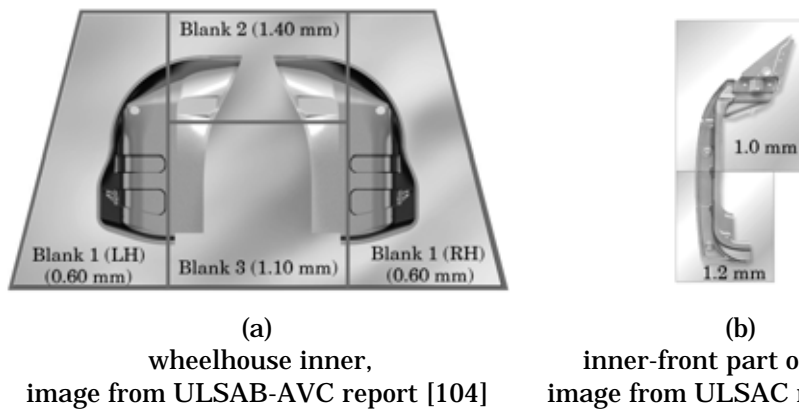


Fig. 1.5: Examples of a tailor welded blanks in automotive applications.

The application of tailor welded blanks leads to a weight reduction of the final product, as otherwise the entire product should be made of the thicker sheet. Other possibilities of pre-welded blanks are controlled collapse by creating buckling points in car crumple zones, enhanced corrosion protection by application of dissimilar materials and a reduction of the assembly costs due to a decrease in the number of parts. Unfortunately the weld joining the blanks has an increased surface roughness, as illustrated in Fig. 1.6(a). Furthermore, the weld and the surrounding heat affected zone show increased hardness. This combination of increased roughness and hardness can result in excessive wear by abrasion of the deep drawing tool, as shown in Fig. 1.6(b).

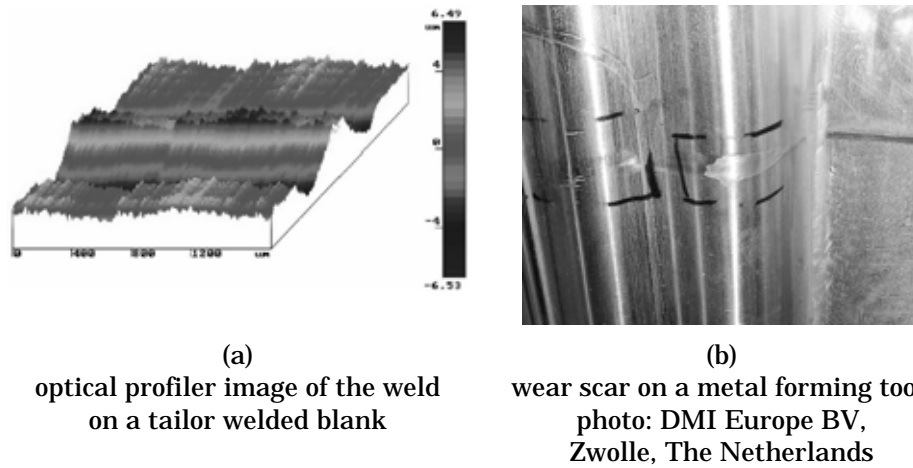


Fig. 1.6: Wear due to the processing of tailor welded blanks.

1.5 Extending tool life

In the preceding it was stated that tool wear is the result of the sliding contact between the tool and a harder rough surface. To prevent this abrasive wear from happening, the tool can be heat treated and a hard surface layer can be applied. Fallböhmer et al. [36] indicate that a substantial part of the dies manufactured have some kind of coating.

Commonly applied surface treatments and coating techniques for sheet-metal forming tools are heat treatments, nitriding and hard chromium plating. These surface treatments meet the demands of most conventional sheet-metal forming applications. However, layers applied with these methods will fail when the contact conditions become more severe, e.g. in poor lubricated sheet-metal forming as mentioned before.

Alternative surface treatments include vapour deposition techniques, hard facing (e.g. laser cladding and fusion welding), and chemical diffusion techniques. However, applying such a coating on a sheet-metal forming tool is not as straightforward as it appears to be. Particularly in automotive applications the tool material usually is relatively ductile, which makes it unsuitable for direct application of a thin hard layer. Cracking of the thin surface layer due to this difference in hardness and elastic properties might be prevented by application of one or more intermediate layers. Furthermore, as discussed by Mitterer et al. [78] a commonly applied coating technique as Chemical Vapour Deposition (CVD) requires a relatively high process temperature, causing loss of substrate hardness and a possible dimensional change of the tool. In Physical Vapour Deposition (PVD) processes the size

and weight of the tool can be problematic as movement of the substrate is required in order to deposit a uniform layer [78]. Finally, optimisation of the tribological system is difficult as the costs of the tools are extremely high [78]. Despite all these problems, several researchers (e.g. de Rooij [26], van der Heide [109], Mitterer et al. [78], Pesch et al. [85]) present results indicating increased wear resistance using these, for sheet-metal forming tools, non-conventional coating techniques.

1.6 Objective of this research

The developments in industrial sheet-metal forming operation, as discussed in the preceding, lead to wear of the forming tools and consequently an increase in scrap, press down time due to maintenance and failure and hence an increase in manufacturing costs.

This research focuses on the abrasive wear of sheet-metal forming tools due to the processing of tailor welded blanks. As indicated, a possible solution to this abrasive tool wear problem is the application of (a combination of) protecting surface layers on the tools. Due to the high costs involved in the manufacturing of the forming tools, tribological process optimisation is difficult. To be able to achieve the most optimal solution, a mathematical model for the abrasive wear of deep drawing tools will be required. The objective of the research described in this thesis is the development of a mathematical model that describes the abrasive wear of deep drawing tools.

1.7 This thesis

This thesis focuses on the abrasive wear of cast-iron tooling equipment due to the contact with a tailor welded blank. The studied mechanism of abrasive wear is that of hard surface roughness asperities on the weld of a tailored blank scratching through the relatively soft tool material.

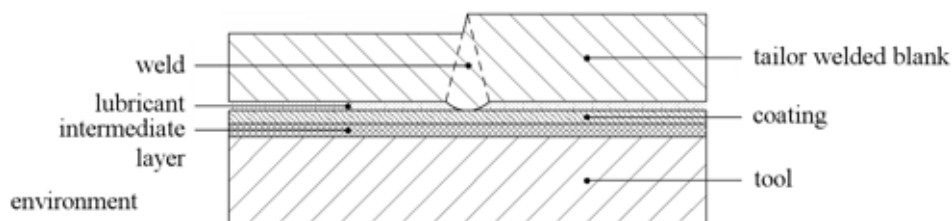


Fig. 1.7: Tribological system.

In Fig. 1.7 the tribological system under consideration in this thesis is shown. It is composed of a (coated) deep drawing tool, a tailored blank, a lubricant

and an environment. However, by analysing this tribo-system at different "magnifications" properties of the system can change considerably. At a large magnification the contact situation is that of a single hard roughness asperity scratching through a soft material, while on a larger scale the tribo-system is composed of the macroscopic contact between an industrial tailor welded blank and a deep drawing tool.

The chapter layout of this thesis as shown in Fig. 1.8 is based on the classification of the different levels of a tribological system. These levels are discussed in more detail in Chapter 2.

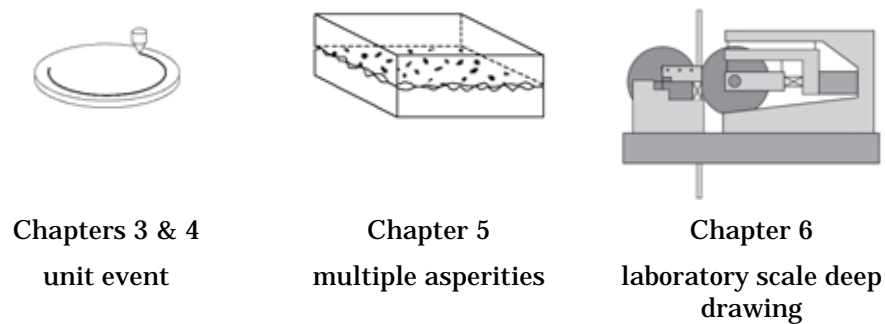


Fig. 1.8: Layout of the contents of this thesis.

As (two body) abrasive wear is initiated at asperity level, the analysis is started with a study of the elementary contact between a single hard asperity and a soft flat in Chapter 3. A contact model is developed for the elastic-elastoplastic-plastic contact between an ellipsoidal shaped asperity and a smooth surface. In Chapter 4, based on single indenter scratch experiments, an asperity abrasivity map is constructed. By combining this abrasivity map and the contact model the volumetric wear due to a single scratching asperity can be calculated. Subsequently, in Chapter 5 this unit event is extended to the contact and wear behaviour of rough surfaces, where a rough surface is assumed to be composed of a large collection of asperities. Chapter 6 describes the contact situation that occurs in practical deep drawing processes. The experiments on the deep drawing simulator are discussed. Furthermore, the developed contact and wear model is applied to practical deep drawing, i.e. the contact between the forming tool and the weld on the blank. Finally, in Chapter 7 conclusions for this research are drawn and some recommendations for future research are made.

Chapter 2

Deep Drawing and Tribology

This chapter provides a brief introduction to the theory of friction, lubrication and wear of deep drawing processes. In the first section the tribological system under investigation in this thesis is discussed. Subsequently some general aspects of tribology, including the contact between rough surfaces, lubrication regimes and possible wear mechanisms are discussed. Finally, attention is paid to the tribology of the deep drawing process.

2.1 Tribological system

The science of tribology studies the contact between interacting surfaces in relative motion. In such a contact several mechanical, chemical and physical processes occur simultaneously, leading to friction in the contact and wear of one or more of the contacting surfaces. The contact behaviour cannot be expressed in a single material property like the Young's modulus or the hardness, but depends on the ensemble of the materials in contact, the lubricant and the environment. Together, these components form the tribological system.

A schematic illustration of the tribo-system under consideration in this work is shown in Fig. 1.7 in the previous chapter. It is composed of a tailored blank, a sheet-metal forming tool with one or more hard surface layers, a lubricant and an environment. In the following sections, the components shown in the figure will be elucidated.

2.1.1 The tool

The tool material under consideration in this thesis is a spheroidal graphite cast iron, which is commonly applied for sheet-metal forming tools. The material is designated EN-GJS-700-2 after the European Standard DIN EN 1563 [32] and has a perlitic structure. The material is also known as GGG70L and has increased strength and ductility in comparison to most other grey cast irons. The surface of an industrial deep drawing tool generally is ground to a surface roughness R_q of about $0.1 \mu\text{m}$. According to the DIN standard the Brinell hardness of the material ranges between 225 HB and 305 HB, which can be converted approximately 2400 MPa to 3200 MPa Vickers. However, the Vickers hardness of the specimens used in the experiments was measured on several hardness testers and found to be slightly higher, 3350 MPa.

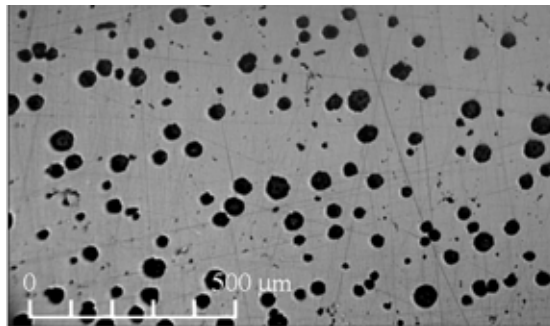


Fig. 2.1: Microscope image of a nodular cast iron surface.

The surface of the tool material, as shown in the microscope image of Fig. 2.1, is covered with a large number of spherical shaped carbon nodules, which range in diameter from several micrometers to about $80 \mu\text{m}$. These carbon spheres can cause difficulties with respect to the adherence of coatings and surface layers. Some material properties for EN-GJS-700-2 are listed in Appendix A.1.

Surface Layers

To prevent hard rough asperities on a surface from penetrating into a softer counter surface, the softer surface can be covered with (a combination of) surface layers with a higher hardness than the asperities. A range of such hard surface layers is considered in this thesis. All surface layers used in this work are commercially available. Based on the manufacturing process they can be divided into three classes:

- Physical vapour deposition layers
- Electrolytic layers
- Laser clad layers

Physical Vapour Deposition (PVD)

In PVD processes the coating material (the reactant) is evaporated in a high vacuum chamber (10^{-1} - 10^{-4} Pa) at a temperature ranging between 200°C and 500°C. By means of a plasma the reactant is transported to the substrate where it condenses. Using PVD processes it is possible to deposit atomically thin layers on a substrate. This layer is uniform in thickness, so the application of a PVD layer to a surface does not affect the surface roughness characteristics. Examples of surface coatings that are deposited using a PVD process are Chromium Nitride (CrN), Titanium Nitride (TiN) and Metal-Carbon (MC) layers. Because of their high hardness the latter are also known as Diamond Like Carbon (DLC) coatings.

Often these coatings are applied as duplex layers, consisting of at least two layers with different properties. A common example is the use of an intermediate layer to ensure proper adherence of the top layer to the substrate. More complex duplex layers can consist of as many as 20 thin layers. On relatively soft and ductile substrates the application of a duplex coating may be required in order to provide a more gentle transition in physical properties and to prevent cracking of the thin hard coating due to the deformation of the substrate (the egg-shell phenomenon). This also applies to the EN-GJS-700-2 tool material used in this work as the material is ductile, but also because of the very soft carbon nodules. Some typical hardness values of PVD coatings are presented in Table 2.1.

Table 2.1: Typical properties of some hard surface layers.

Coating	Coating process	Hardness [GPa]	Thickness [μm]
Titanium Nitride (TiN)	PVD	28	1-5
Metal-Carbon (MC)	PVD	10-25	1-10
Chromium Nitride (CrN)	PVD	20	1-8
Hard Chromium (HCr)	Electroplating	8-11	> 3
Cobalt based alloy A (St6)	Laser cladding	4	> 100
Cobalt based alloy B (Ult)	Laser cladding	3	> 100

Electrochemical deposition

In electrochemical deposition or electrolytic chrome plating the substrate is submerged into a chromium-acid solution and negatively charged. A high current flows from the inert anode to the work piece, resulting in deposition of the chromium from the solution to the cathode. Common current densities are in the order of 1.2×10^4 A/m². A large range of layer thicknesses is possible,

from several micrometers to more than a millimetre. An example of a surface layer deposited using an electrochemical process is a hard chromium layer.

Laser cladding

In laser cladding the surface layer is composed of a powder that is fed onto the surface of the substrate. A laser beam melts both the powder and a top layer of the substrate, resulting in a good bond between the coating and the substrate and limited dilution. Common layer thicknesses range from tenths of millimetres for single layers to several millimetres for stacked layers. Typical powder materials are tungsten alloys and cobalt alloys. After application of the layer a surface finishing operation like grinding or polishing is required. Some properties for two commonly applied cobalt based clad layers are listed in Table 2.1.

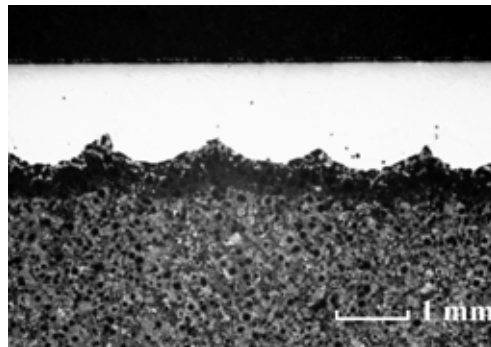


Fig. 2.2: Cross-section of a laser clad surface.

2.1.2 The blank

The tailor welded blank is composed of at least two sheets that are joined by a weld, as discussed before. The sheet material is designated in DIN EN 10130 [31] as DC05 extra deep drawing quality sheet-metal. Material properties for DC05 can be found in Appendix A.3.1.

The weld complies to quality level B, "stringent" of the European Standard EN ISO 13919-1:1996 [52]. In this standard the quality of the weld is defined by 18 imperfection designations. To determine the quality levels of the weld on the tailor welded samples, some of the samples were sliced at multiple positions and the geometry of the weld was measured. Results of this analysis are shown in Appendix A.3.2.

The surface micro-geometry of the weld on the tailor welded blank, as shown in Fig. 2.3, is highly anisotropic and shows a v-shaped or fish bone shaped pattern. The welding direction is from left to right. The hardness of the weld

is about 2000 MPa, which is lower than that of the tool material. However, the weld is covered with a very thin, hard oxide layer. This layer causes abrasion of the tool.

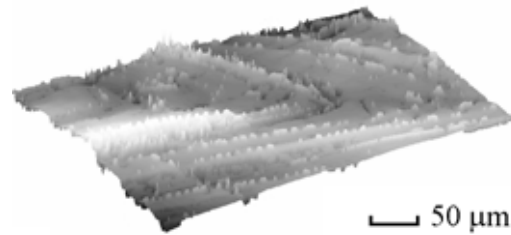


Fig. 2.3: Surface micro-geometry of a weld.

2.1.3 Lubricants

The lubricant applied is Quaker Ferrocote® N6130 conservation oil. This corrosion preventive oil is often applied in the automotive industry. The lubricant has a dynamic viscosity of 55 mPa·s at 22° C.

2.2 Systems approach in Tribology

When analysing a tribological system, taking every possible variable into account leads to an abundance of interacting parameters and hence to complex relations. This was observed by Czichos [24], who introduced the systems approach to tribology. In this approach the tribological contact situation is extracted from the application by the definition of a systems envelope: a clear demarcation of the elements that are taken into account in the tribological analysis. According to DIN 50322 [30] for every tribological process a range of systems envelopes and accompanying analysis levels can be distinguished.

The objective of this research is to develop a model that describes the abrasive wear of the tool in deep drawing operations. The results of the model should have a good correlation with industrial reality and therefore the type of analysis that is best suited is a field test. However, overlooking the fact that experimental validation of such a model will be quite expensive, the abrasive wear mechanism is initiated at the scale of surface roughness and can not be described at this macroscopic level. Therefore the approach followed in this work is first to gain a more profound understanding of the abrasive wear process at a microscopic scale. Subsequently the model is extended to describe abrasive wear between rough surfaces. Finally the model will be applied to the deep drawing process and the results will be compared with experiments

on a laboratory scale deep drawing simulator. As a consequence in each of the following chapters a different systems envelope is chosen, as was already indicated in Fig. 1.8 in the previous chapter, showing the layout of this thesis.

2.3 Tribology: contact, friction, lubrication and wear

The following section covers some basic principles concerning the contact between surfaces. Firstly the dry, or unlubricated contact between bodies is discussed. Subsequently the possible lubrication regimes are treated and some attention is given to wear processes that might occur in these tribological contacts.

2.3.1 Contact between rough surfaces

2.3.1.1 Contact

When two bodies are in contact and deform elastically, the resulting contact pressure, contact area and deformations of the bodies in contact can be calculated using the theory of Hertz [47], assuming that the total deformation is small compared to the geometry of the contacting bodies and that the bodies are continuous frictionless elastic half-spaces.

2.3.1.2 Surface roughness

In Hertz' theory both surfaces are supposed to be smooth. However, engineering surfaces are never perfectly smooth and inside the macroscopic or apparent contact, real surface to surface contact only occurs at localised spots. Thus the real area of contact covers merely a fraction of the apparent area, as illustrated in Fig. 2.4.

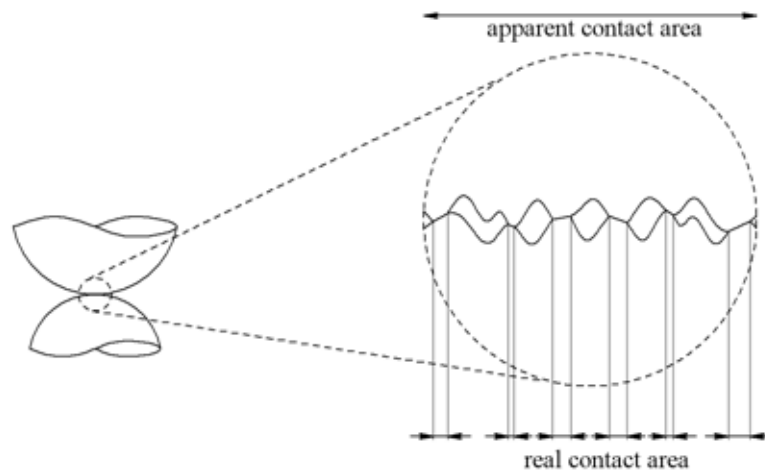


Fig. 2.4: Apparent and real area of contact.

The surface height distribution of an engineering surface usually can be approximated by a Gaussian probability function. Accordingly, the roughness of a surface commonly is expressed using statistical parameters of the surface height data, like the arithmetic mean (R_a) and the root mean square (R_q). From a given dataset $z(x)$ containing surface height data, these parameters can be calculated using eq. (2.1) and eq. (2.2), in which z_0 represents the reference value of the dataset.

$$R_a = \frac{1}{L} \cdot \int_{x=0}^L |z(x) - z_0| dx \quad (2.1)$$

$$R_q = \sqrt{\frac{1}{L} \cdot \int_{x=0}^L |z(x) - z_0|^2 dx} \quad (2.2)$$

Because these roughness parameters are statistical, they give average information about the surface topography. Anisotropy of the micro-geometry or any local features are not represented. Therefore, surfaces that have equal statistical roughness parameters can show a completely different surface micro-geometry. This is illustrated in Fig. 2.5, where the surface topography of two surfaces is shown. In this picture roughness valleys are shown in black, while peaks are represented by light colours. Surface A has an isotropic surface micro-geometry and surface B is highly anisotropic, whereas the statistical roughness parameters R_a and R_q of the two surfaces have almost the same values.

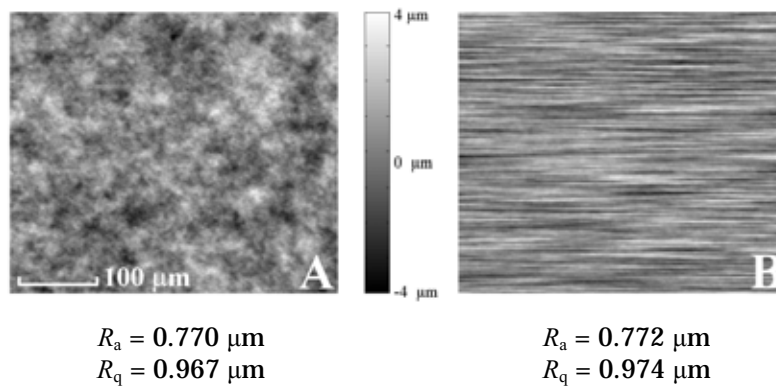


Fig. 2.5: Rough surfaces with equal statistical roughness.

Besides this, the value of statistical roughness parameters depends on the measurement technique and is heavily scale dependent. Settings like the resolution of the roughness measurement and the cut-off length affect the outcome of the measurement significantly. Therefore measurement techniques and methods are standardised, see for instance DIN 4768 [28].

2.3.1.3 Micro-contacts

In the previous it was shown that actual contact between rough surfaces occurs at the micro-contacts: the locations where surface roughness protuberances touch. The size of the micro-contacts depends on the contact load; with increasing load new micro-contacts are formed while existing micro-contacts grow and merge with neighbouring micro-contacts. In Fig. 2.6 this process is illustrated for three values of the separation between the surfaces d . The solid line in Fig. 2.6(a) shows a section of the micro-geometry of a rough surface. The dotted lines represent a flat and smooth counter surface that approaches the rough surface. In the first situation ($h = h_1$) only a small micro-contact exists. With increasing approach the contact size increases and at $h = h_2$ the contact consists of two neighbouring micro-contacts. At $h = h_3$ these two micro-contacts have merged, forming a relatively large micro-contact. Deformation processes in surface topography are quite complex and the process as illustrated in Fig. 2.6 is a simplification.

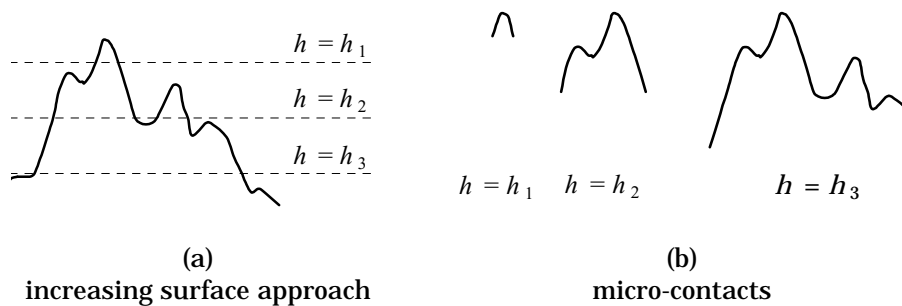


Fig. 2.6: Changing micro-contact with changing surface separation.

Another factor that complicates the analysis of micro-contacts is the large range of length scales contained in the problem. The contact area between two surfaces can be several square millimetres, while the length scale of surface roughness is in the order of micrometres and on this surface micro-geometry even smaller nanometre-scale irregularities can be observed, as illustrated in Fig. 2.7.

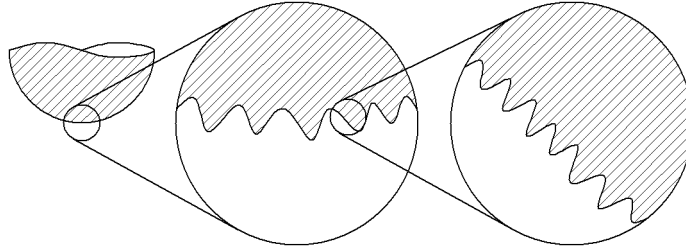


Fig. 2.7: Schematic illustration of scales of surface roughness on a body.

2.3.2 Friction and lubrication

The previous section discusses the unlubricated contact between rough surfaces. However, the interacting bodies in a tribological system are usually in some degree separated by a lubricant. Lubricants are applied in order to decrease the coefficient of friction and to prevent wear of the contacting bodies. However, to what extent a lubricant has these desired effects depends on the operating conditions of the tribological contact. In a generalised Stribeck diagram, the coefficient of friction is plotted against these operating conditions, collected in the dimensionless lubrication number L , defined by Schipper [93] as:

$$L = \frac{\eta \cdot v^+}{p_0 \cdot R_a} \quad (2.3)$$

In this, η represents the dynamic lubricant viscosity, v^+ the sum velocity of the two surfaces, p_0 the nominal contact pressure and R_a the arithmetic mean of the combined surface roughness.

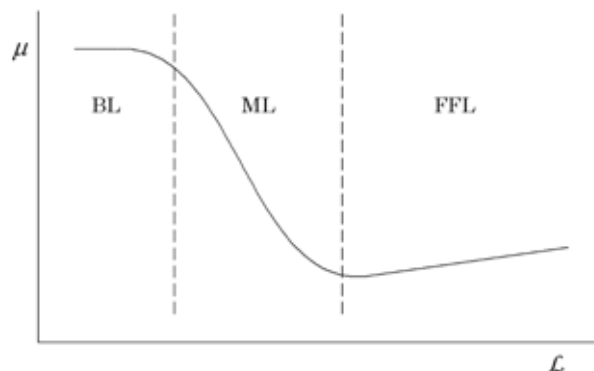


Fig. 2.8: Generalised Stribeck diagram

With increasing lubrication number three lubrication regimes can be distinguished in the Stribeck diagram, each with a characteristic level of the coefficient of friction: Boundary Lubrication (BL), Mixed Lubrication (ML) and Full Film Lubrication (FFL).

Full film lubrication occurs at high values of the lubrication number, i.e. a highly viscous lubricant, a high velocity, a low contact pressure and/or a low surface roughness. In this situation a relatively thick lubricant film is formed that completely separates the two surfaces in the contact and entirely carries the contact load. In this regime, difference in velocity of the two surfaces results in shear of the lubricant film, leading to a very low coefficient of friction, in the order of 10^{-3} ~ 10^{-2} . In relatively lightly loaded contacts and in contacts between conformal surfaces the contact pressure is low, resulting in a negligible deformation of the surfaces. This type of full film lubrication is called hydrodynamic lubrication (HL) and occurs for example in journal bearings and in the contact between tape and head in magnetic recording. In highly loaded applications as gears and ball bearings the elastic deformation of one or both contacting surfaces is substantial and therefore can not be neglected anymore. This lubrication regime is referred to as elasto-hydrodynamic (EHL). In plasto-hydrodynamic lubrication (PHL) one of the bodies deforms plastically while a full fluid film is maintained. This situation can occur in some metal forming processes, like rolling, wire drawing and extrusion and is generally unwanted, as it might lead to poor surface finish due to cushioning of entrapped lubricant (see Schey [92]).

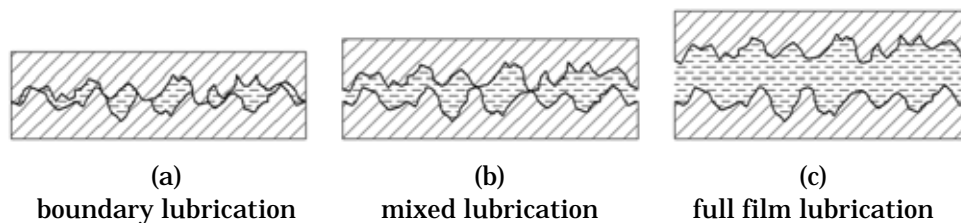


Fig. 2.9: Lubrication regimes.

In the boundary lubrication regime physical contact between the interacting surfaces occurs and the contact load is carried entirely by surface roughness asperities that are in contact. The difference in velocity of the two surfaces leads to shear in the boundary layers on the surfaces, resulting in a relatively high coefficient of friction: typical values range from 0.1 to about 0.25. The primary benefits of lubricants in boundary lubrication are heat dissipation from the contact, the formation of protecting boundary layers and the removal of possible third bodies out of the contact.

The mixed lubrication regime covers the transition between boundary and full film lubrication. In this regime part of the contact load is carried by the micro-contacts and part by the lubricant. Consequently, the coefficient of friction has a value between 10^{-2} and 10^{-1} .

Under mixed-lubrication and boundary lubrication conditions it is possible that full film lubrication occurs at a local scale in the micro-contacts. This situation of micro-EHL or micro-PHL might again lead to low values of the coefficient of friction.

2.3.3 Wear

Wear is defined as the loss of material from the surface of a solid body evoked by the contact and relative motion with a solid, liquid or gaseous counter body. In general, wear of technical components has a negative effect on the functioning of an assembly and reduces the value of the component. However, sometimes wear mechanisms are required for smooth operation of a tribo-system, for instance in running-in. Wear manifests itself in changes in shape and composition of the surface as well as in small wear particles that are detached from the surface. In the German standard DIN 50320 [29] four wear mechanisms are classified:

- Tribochemical wear
- Surface fatigue
- Adhesive wear
- Abrasive wear

Tribochemical wear occurs when one or both of the two surfaces chemically reacts with constituents in the lubricant or the environment. Once in contact, the layer of reaction products that is accordingly formed on the surface might be removed and a cycle of continuous formation, removal and reformation of a layer of reaction products occurs, resulting in progressive material loss.

Surface fatigue wear or delamination is the process of crack formation, crack growth and particle detachment of a surface caused by cyclic stress variations in the contact. It is characterised by an incubation period: the actual wear process only starts after some period of use. Typical applications that are subject to surface fatigue are ball bearings and railway wheels and tracks.



Fig. 2.10: Adhesive wear: transferred zinc lumps on a tool surface.

Adhesive wear occurs in a contact when the junction between the two contacting bodies due to solid phase welding is stronger than the atomic bond inside one of the solid bodies. Therefore adhesive wear is a major problem in aerospace applications: usually a metal surface is covered with a thin oxidation layer that decreases the adhesion between two surfaces, but in the vacuum environment of space no oxidation occurs and the adhesive forces between two contacting surfaces can become quite high, resulting in severe adhesive wear. Another example occurs in deep drawing of zinc coated sheet, where the soft zinc adheres to the tool material, forming lumps (see Fig. 2.10 and the work of de Rooij [26] and van der Heide [109]). These lumps grow and might cause abrasive wear of the processed sheets, resulting in scratches on the formed product.

Abrasive wear is the result of scratching and micro-cutting of a surface by hard protuberances on the counter surface or by hard particles in the contact. Generally, abrasive wear is divided into two sub-categories: two body and three body abrasive wear, depending on the body that causes the scratching action. In three body abrasion, hard particles are trapped between the two bodies but free to move with respect to both surfaces, while in two body abrasion these hard particles are embedded into one of the surfaces, which restrains free movement of the particles. Two body abrasion also occurs if one of the two contact partners is rough and significantly harder than the other, enabling surface roughness asperities to penetrate and scratch through the softer surface.

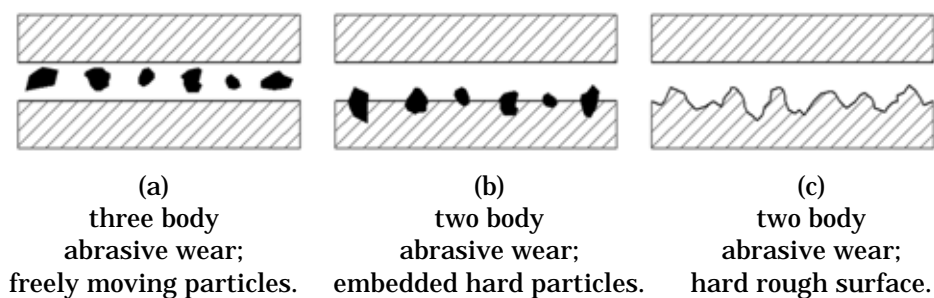


Fig. 2.11 Abrasive wear modes.

The wear particles in three body abrasion can have many origins, like environmental (sand or atmospheric dust), from the machine (wear particles from another contact or soot) or from the contact itself. A rule of thumb for abrasive wear to occur is that the abrasive body has a hardness that is at least 20% higher than the abraded surface (see Torrance [100]).

Two body abrasive wear is the investigated wear mechanism in this thesis and is therefore discussed in some more detail. Fig. 2.12 illustrates the abrasive action of a hard asperity in contact with a softer flat. The hard asperity has a conical shape with front angle or 'attack angle' φ and scratches through the soft material. In the ideally plastic situation the contact is semi-circular with radius a . Since the indenter moves, the load is carried by its front half.

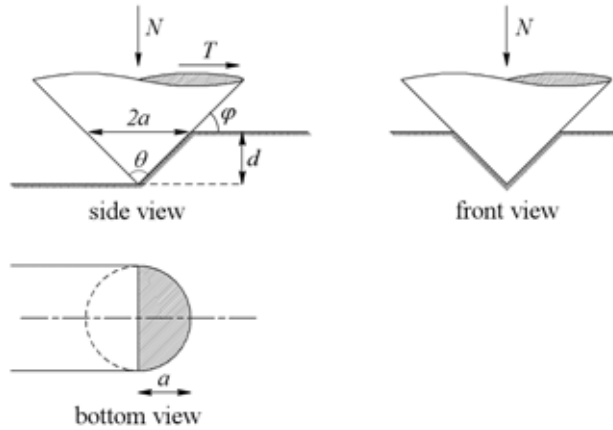


Fig. 2.12: Geometry of contact between a conical abrasive and a smooth deforming flat.

The contact load is expressed by eq. (2.4), with p_0 the average contact pressure and a and d the contact radius and indentation depth of the asperity respectively, as defined in the figure.

$$N = p_0 \cdot \frac{1}{2} \cdot \pi \cdot a^2 = \frac{1}{2} \cdot p_0 \cdot \pi \cdot \frac{d^2}{\tan^2(\varphi)} \quad (2.4)$$

The frontal area of the cone equals $A_f = \frac{1}{2} \cdot 2 \cdot a \cdot d = a \cdot d = d^2 \cdot \tan^{-1}(\varphi)$. If a fraction ζ of the material displaced from the groove is actually removed from the surface as wear debris, the volumetric wear per unit sliding distance Ψ is:

$$\Psi = \xi \cdot A_f = \xi \cdot d^2 \cdot \tan^{-1}(\varphi) \quad (2.5)$$

By solving eq. (2.4) for d and assuming that the contact pressure is equal to the hardness of the deforming material H , eq. (2.5) reduces to:

$$\Psi = \frac{2 \cdot \xi \cdot N}{\pi \cdot H} \cdot \tan(\varphi) \quad (2.6)$$

From this it can be concluded that the volumetric abrasive wear depends on the effectiveness of the abrasive process, expressed in the parameter ξ , the load on the contact N , the hardness H of the deforming material and the shape of the abrasive body, contained in the attack angle φ .

2.4 Tribology of the deep drawing process

During a deep drawing operation the punch pushes the blank into the die cavity and a product is formed. Throughout the deformation process the surface of the blank is in sliding contact with the forming tools, resulting in friction and wear in the contact.

The coefficient of friction in the deep drawing process has a large influence on the formability of the sheet and therefore on the optimisation of the manufacturing process. Wear of both the tool and the final product should be minimised, as they might result in poor surface finish and geometrical deviances.

2.4.1 Contact situations in deep drawing

Between the components in a deep drawing operation (punch, die, blank and blank holder) three different contacts arise:

- the contact between punch and blank
- the contact between tool and blank
- the contact between blank holder and blank

In these three tool-work piece contacts, a total of five contact zones with separate properties can be distinguished. In Fig. 2.13 these zones are shown for the deep drawing process of a simple axi-symmetric cup. The contact between punch and blank, as marked ①, ② and ③, is characterised by a low relative sliding velocity, in the order of 10^{-4} m/s. This means that the punch and the blank are moving at almost the same velocity. Any difference in velocity is caused by the deformation of the blank: at the punch nose ① the blank is in a biaxial stretching state, at the punch radius ② a combination of

bending and stretching occurs and in the unsupported zone between punch and blank ③ so-called free drawing takes place.

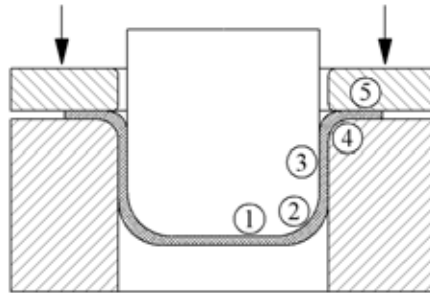


Fig. 2.13: Contact zones in deep drawing.

In the contacts between forming die and blank ④ and between blank holder and blank ⑤ the sliding velocity is of order $10^{-3} \sim 10^{-1}$ m/s, which is relatively high. In these contacts the sliding velocity is mainly determined by the velocity of the punch. At the radius of the die ④ a combination of stretching and bending occurs, while in the blank holder – blank contact ⑤ the diameter is reduced, leading to circumferential compression in the blank. In the blank holder region contact pressures are relatively low, between 1 and 10 MPa, while at the die radius, the contact pressure can exceed 100 MPa. The contact conditions are most severe in the contact zones marked ④ and ⑤ where the predominant lubrication regimes are boundary lubrication and mixed lubrication (ter Haar [99]). Hence these zones are interesting for studying tribological aspects of the deep drawing process.

Contact and friction in sheet-metal forming processes are discussed by a number of authors. An extensive overview is given by Schey [92]. Ter Haar [99] focussed on the development of a model for friction in sheet-metal forming for application in finite element code as well as on the development of an experimental set-up for the validation of the developed friction model. The work on a model for friction in the deep drawing process was extended by Emmens [34], who investigated flattening of surface roughness asperities and Westeneng [113], who developed an improved contact model for sheet-metal forming applications, taking both local and global plasticity into account.

2.4.2 Wear in deep drawing

In the automotive industry, sheet-metal parts usually are covered with a soft zinc layer, intended for corrosion protection of the final product. During the forming of such sheet, small zinc particles adhere to the tool, forming lumps that eventually cause scratches on the product. As a result, traditionally wear research in sheet-metal forming processes focuses on this galling phenomenon.

Van der Heide [109] described the initiation of adhesive wear of the blank on the scale of surface roughness, due to local thermal lubricant failure. De Rooij [26] described the growth of these lumps due to galling and developed a method for experimental observation of such micro-scale adhesive processes using image processing techniques. Other work on the galling in sheet-metal forming includes Schedin [90], Schedin and Lehtinen [91], Andreasen [3] and van der Heide et al. [108].

As discussed before, recent trends in industrial deep drawing cause an increase in abrasive severity of the contact, manifesting itself in abrasive wear of the tool. Therefore only recently research is initiated at the abrasive wear of the tools. Some examples are Vermeulen [111] who investigated abrasive wear of the tool induced by the processing of tailor welded blanks and Sniekers [95] and Eriksen and Wanheim [35] who discuss the prevention of abrasive tool wear by optimising the geometry of the tool.

2.4.3 Tribological characteristics of deep drawing processes

Summarising, this work focuses on the abrasive wear of deep drawing tools in the processing of tailor welded blanks. The studied tribological system satisfies the following conditions and restrictions:

- The system is composed of a tool, a sheet, a lubricant and an environment.
- The material of the tool is smooth and relatively soft.
- The tool may be covered with a hard surface layer.
- The bulk of the sheet deforms plastically.
- The sheet is rough and relatively hard.
- The surface of the sheet and the weld is virginal.
- The lubricant is a commercially available conservation oil with some lubricating properties.
- The environmental conditions are atmospheric and at room temperature.

Chapter 3

Single Asperity Contact

3.1 Introduction

In any contact between two rough contact partners, actual surface to surface contact only occurs at localised spots, the so-called micro-contacts. In non-lubricated and boundary lubricated systems, i.e. when there is no hydrodynamic action in the contact, these micro-contacts transmit the load carried by the contact from one surface to the other, see Fig. 3.1. Sliding wear processes might arise in the micro-contacts when there is relative motion between the two contact partners. An example of such a sliding wear process is abrasive wear, which may occur in the case of a significant difference in hardness between the contacting surfaces [100]. Roughness protuberances on the harder surface penetrate into the softer one and the sliding motion may cause material to be removed from the softer contact partner. This is also the case in the investigated contact situation of a hard and rough weld of a tailor welded blank against a softer tool. To understand the abrasive wear process of surfaces in contact, both the contact and the wear mechanisms arising in micro-contacts have to be studied. The contact behaviour is investigated in the current chapter. Subsequently, Chapter 4 focuses on the determination of the abrasive wear behaviour of a single micro-contact.

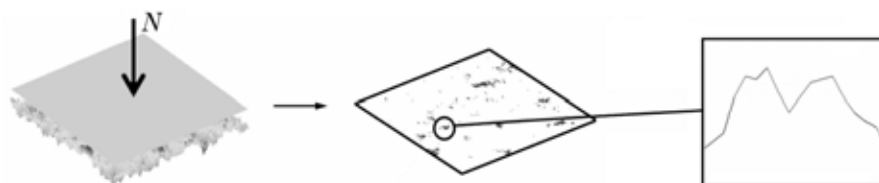


Fig. 3.1: Surface roughness and single micro-contact.

In the tool-tailor welded blank contact, a micro-contact consists of a rigid protuberance on the weld in contact with a deforming smooth tool surface. The shape of this protuberance can be approximated by a simple geometrical body, of which the size and shape are determined by curve fitting of the surface micro-geometry inside the micro-contact. This simplification enables a description of the contact using relatively straightforward equations. In the following, the simple geometrical body representing the surface micro-geometry will be called an asperity. Two basic shapes of asperities are studied (see Fig. 3.2): elliptic cones and paraboloids. These shapes might be interpreted as a first order respectively a second order approximation of the actual surface micro-geometry of the roughness protuberance.

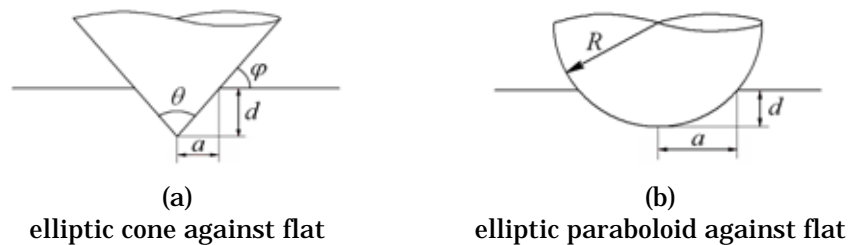


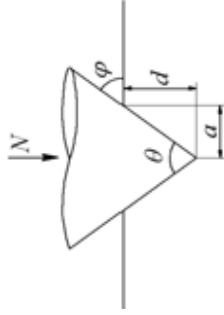
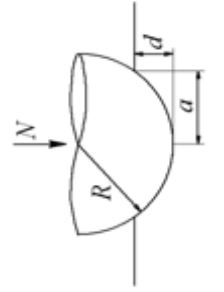
Fig. 3.2: Single asperity contacts.

The analysis is started for conically shaped asperities. First the equations for the axi-symmetric body, i.e. a cone with a circular base, are derived after which the model is extended to the more general situation of a cone with an elliptic base. This ellipticity of asperities enables incorporating anisotropy of the abrasive body. Next, equations are derived for paraboloidal shaped asperities. Furthermore, the effects of hard surface layers on the contact behaviour are discussed. Finally some examples of application of the contact model in practical situations are given.

3.2 Static versus sliding contact

Table 3.1 presents equations describing the static contact between a conical shaped respectively a paraboloidal shaped asperity and a smooth, flat counter surface. In this contact situation, which is extensively discussed in Appendix B.1, the contact load only has a normal component. For modelling abrasive wear the behaviour in sliding contact is of interest. In sliding contact the load is composed of both a normal component and a tangential or frictional component. Throughout this chapter the derived equations are illustrated with calculations using a reference system. This reference system consists of a cast iron flat body in contact with a diamond indenter. In the discussion of coated surfaces the cast iron body is covered with a $5\ \mu\text{m}$ TiN coating. Mechanical properties of this tribo-system are listed in Appendix A.

Table 3.1: Summary of equations for the static contact situation.

		
elastic	n.a.	$A_e = 2 \cdot \pi \cdot R_* \cdot \alpha_x \cdot \alpha_y \cdot \gamma^{-1} \cdot d$ $N_e = \frac{4}{3} \cdot d^{1.5} \cdot \gamma^{-1.5} \cdot E_* \cdot \sqrt{2 \cdot R_*}$
transition	n.a.	$d_{e,trans} = \frac{9}{8} \cdot \pi^2 \cdot \alpha_x^2 \cdot \alpha_y^2 \cdot \gamma \cdot R_* \cdot k^2 \cdot E_*^{-2} \cdot H^2$
elastoplastic	$A_{ep} = \pi \cdot (d \cdot \tan^{-1}(\varphi_*))^2$ $N_{ep} = \frac{2 \cdot \pi \cdot H}{9 \cdot \tan^2(\varphi_*)} \left\{ 1 + \ln \left[\frac{\left(\frac{3 \cdot E}{H} \cdot \tan(\varphi_*) + 4 \cdot (1 - 2 \cdot \nu) \right)}{6 \cdot (1 - \nu)} \right] \right\} \cdot d^2$	$A_{ep} = A_e + (A_p - A_e) \cdot (-2 \cdot \delta^3 + 3 \cdot \delta^2)$ $N_{ep} = \left\{ A_e + (A_p - A_e) \cdot (-2 \cdot \delta^3 + 3 \cdot \delta^2) \right\} \times \left[H - H \cdot (1 - k) \cdot \frac{\ln d_{p,trans} - \ln d}{\ln d_{p,trans} - \ln d_{e,trans}} \right]$
transition	$\varphi_{p,trans} = \text{atan} \left\{ \frac{H}{3 \cdot E_*} \cdot \left(6 \cdot (1 - \nu) \cdot e^{\frac{7}{2}} - 4 \cdot (1 - 2 \cdot \nu) \right) \right\}$	$d_{p,trans} = 400 \cdot k \cdot \frac{\sqrt{\lambda}}{1 + \lambda} \cdot \frac{E(1 - \kappa^2)}{\kappa \cdot K(1 - \kappa^2)} \cdot d_{e,trans}$
fully plastic	$A_p = \pi \cdot [d \cdot \tan^{-1}(\varphi_*)]^2$ $N_p = A_p \cdot H$	$A_p = 2 \cdot \pi \cdot \sqrt{R_x \cdot R_y} \cdot d$ $N_p = A_p \cdot H$

3.2.1 Deformation modes

As in static contact, in the sliding contact between a single rigid asperity and a smooth flat three deformation modes can occur: elastic, elastoplastic and fully plastic. Fig. 3.3 illustrates these three modes for a conical indenter. In this figure N indicates the normal load, while the tangential load is represented by the symbol T . Similar situations occur with a spherical indenter.

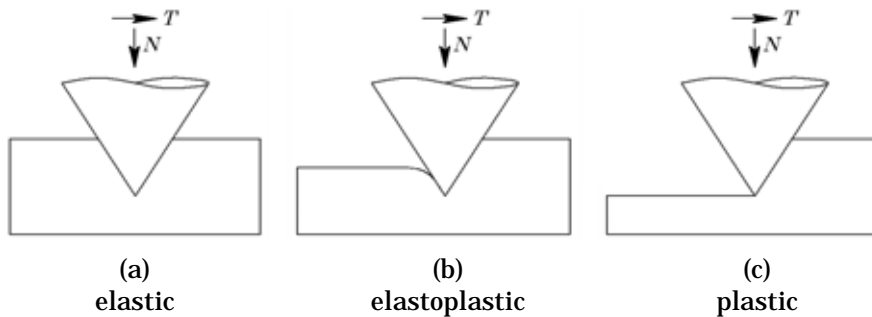


Fig. 3.3: Schematic illustration of deformation modes.

The elastic deformation mode, as shown in Fig. 3.3(a), is characterised by full recovery of the deforming body after the indenter has passed. In the fully plastic mode (Fig. 3.3(c)) the sliding motion of the indenter results in the formation of a groove. In this case elastic recovery of the deforming body can be neglected and depending on the wear mode the material from the groove is either transferred to the side ridges or removed as wear debris. The elastoplastic mode of Fig. 3.3(b) is a combination of elastic and plastic deformation, with some elastic recovery at the back side of the indenter as well as the formation of a groove.

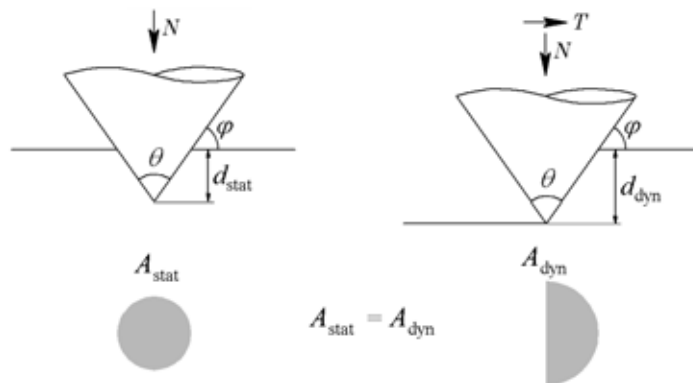


Fig. 3.4: Fully plastic static and sliding contact at a fixed normal load.

A plastic component in the deformation results in the formation of a groove in the softer surface. Therefore the contact load is only carried by the front part of the asperity. Because in plastic deformation the contact pressure equals the hardness of the deforming material, the penetration depth of a moving asperity at an equal normal load will be larger than that of a static asperity, as illustrated in Fig. 3.4. Schematically this is also shown in Fig. 3.5, which illustrates the relation between the contact area and the indentation depth of an asperity.

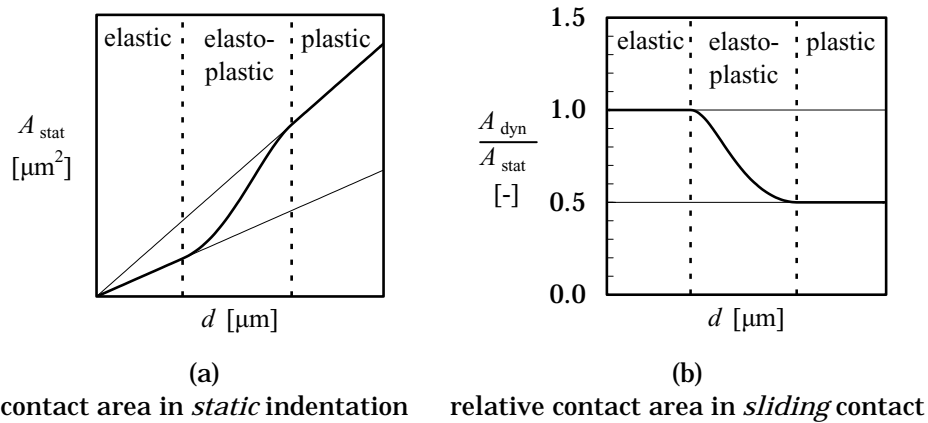


Fig. 3.5: Schematic illustration of the contact area as a function of the deformation mode and indentation depth d .

Fig. 3.5(a) shows this relation for static contact, as discussed by Zhao, Maietta and Chang [118]. The elastic and plastic deformation modes fix the asymptotes, while in the elastoplastic mode a transition between these asymptotes occurs. Fig. 3.5(b) illustrates the relative contact area in sliding as a function of the indentation depth. This relative contact area is defined as the contact area in sliding divided by the contact area in static indentation at a fixed indentation. The elastic mode is characterised by full material recovery after the indenter has passed, hence this ratio equals one. In fully plastic deformation only the front half of the asperity is in contact with the counter surface and the relative contact area in sliding equals 0.5. In the elastoplastic deformation mode, again, a transition can be observed.

In the following sections, the equations shown schematically in Fig. 3.5(a) and (b) describing the contact between conical or paraboloidal asperities and a flat are derived.

3.2.2 Asperities with a conical shape

3.2.2.1 Axisymmetric cone

For a rigid conical shaped asperity the deformation mode depends on the geometry of the indenter and the material properties of the indented material. As explained in Appendix B.1, pure elastic deformation only occurs when the indenting conical body is extremely blunt. Therefore this deformation mode is neglected. In the case of fully plastic deformation the contact spot is semi-circular and the relation between the plastic contact area A_p and the indentation depth d follows from the geometry of the asperity, and is given by eq. (3.1). In pure plastic deformation the contact pressure by definition equals the hardness of the deforming material, resulting in eq. (3.2) for the contact load N_p . Because for a given conical asperity the attack angle φ is fixed, only the indentation depth d will influence the contact area and load.

$$A_p = \frac{\pi}{2} \cdot \left(\frac{d}{\tan(\varphi)} \right)^2 \quad (3.1)$$

$$N_p = \frac{\pi}{2} \cdot H \cdot \left(\frac{d}{\tan(\varphi)} \right)^2 \quad (3.2)$$

An approximation of the contact area in elastoplastic scratching can be obtained from the results of Bucaille, Felder and Hochstetter [11]. They performed numerical simulations on polymer materials and found that due to elastic recovery of the material in the groove the contact spot has the shape of a backwards moving "Pac-man"-figure and hence part of the contact load is carried by the rear part of the indenter. The size of this rear part is expressed using the elastoplastic recovery angle ζ as illustrated in Fig. 3.6.

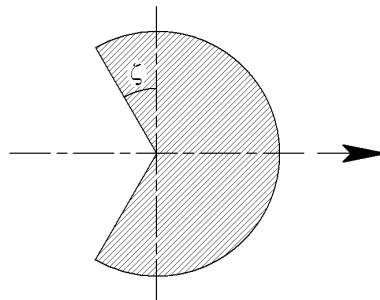


Fig. 3.6: Elastoplastic recovery in the elastoplastic deformation mode.

Values for ζ were calculated in [11] using numerical simulations on a wide range of material parameters. The contact area including elastoplastic recovery can be expressed as:

$$A_{ep} = \left(\frac{\pi}{2} + \zeta \right) \cdot \left(\frac{d}{\tan(\varphi)} \right)^2 \quad (3.3)$$

The table next to Fig. 3.7 lists the values of the recovery angle reported by Bucaille et al. for several contact situations. In this table, $E/H \cdot \tan(\varphi)$ can be seen as a viscoplastic factor of the system that includes both the geometry of the indenter and material properties of the deforming material. Fitting a least squares curve through the data results in eq. (3.4) for the elastoplastic recovery angle in radians. This curve is shown as the line in Fig. 3.7.

$$\zeta = 0.7 \cdot \left(\frac{E}{H} \cdot \tan(\varphi) \right)^{-0.6} \quad (3.4)$$

$\frac{E}{H} \cdot \tan(\varphi)$	ζ (°)
0.33	78
1.67	33
3.33	17
6.67	13
10	12
>20	≈ 0

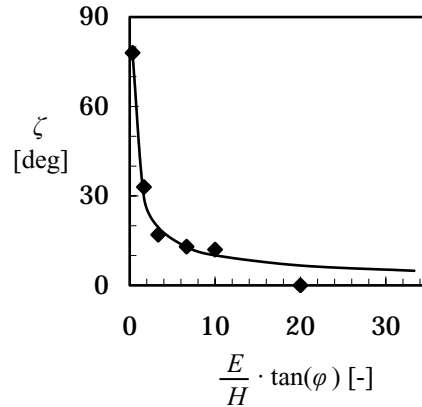


Fig. 3.7: Elastoplastic recovery angle ζ reported by Bucaille et al. [11].

Substitution of eq. (3.4) into eq. (3.3) results in eq. (3.5) describing the elastoplastic contact area. As the elastoplastic recovery angle approaches zero for larger values of the attack angle, this relation can also be applied to describe the plastic contact area:

$$A_{ep} = \left[\frac{\pi}{2} + 0.7 \cdot \left(\frac{E}{H} \cdot \tan(\varphi) \right)^{-0.6} \right] \cdot \left(\frac{d}{\tan(\varphi)} \right)^2 \quad (3.5)$$

The elastoplastic recovery angle ζ according to eq. (3.4) approaches infinity for asperities with a very small attack angle. Obviously ζ can not exceed 90° , which limits the applicability of eq. (3.4). The limiting attack angle can be obtained by inserting the material parameters of nodular cast iron and solving this equation, which results in a minimum asperity attack angle of 0.24° , or a cone angle of 179.5° .

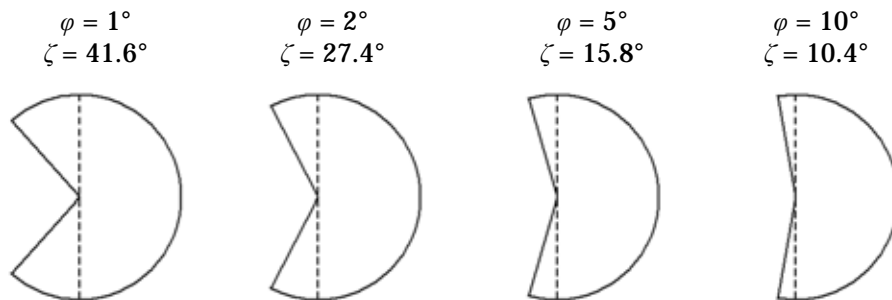


Fig. 3.8: Elastoplastic contact area as a function of the asperity attack angle for the sliding contact of a conical, rigid indenter with nodular cast iron ($E/H = 53$).

A graphical impression of the contact area according to eq. (3.4) for several rigid asperities in contact with nodular cast iron is shown in Fig. 3.8. Particularly when the attack angle of the asperity is small, the elastoplastic recovery is substantial. Furthermore, the figure shows that the elastoplastic recovery angle ζ approaches zero for asperities with a large attack angle φ .

Fig. 3.9 shows the relative contact area in sliding. This relative contact area is defined as the contact area in sliding, denoted by A_{dyn} , divided by the contact

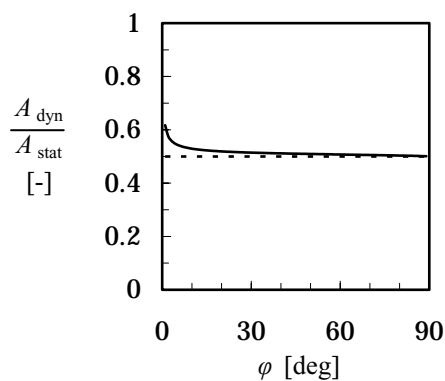


Fig. 3.9: Relative contact area as a function of the attack angle for a sliding rigid conical asperity in contact with a nodular cast iron body.

area in static indentation A_{stat} . For large attack angles the deformation is fully plastic and the contact area in sliding equals half the contact area in static indentation. For smaller attack angles the contact area is larger because of the elastic recovery.

Because of the extensive plastic deformation involved in groove formation at the leading edge of the indenter, the contact pressure in the front semicircle of the contact equals the hardness of the deforming material. At the trailing edge or tail of the contact, where the material is elastically recovered, the contact pressure is lower, however unknown. It is assumed that in the tail the pressure drops from $p = H$ at the centre line of the contact spot (the dashed lines in Fig. 3.8) to $p = 0$ at the edge of the tail. In that case the average contact pressure in the tail equals $p = \frac{1}{2}H$, leading to eq. (3.6) for the elastoplastic contact load.

$$N_{\text{ep}} = \left[\frac{\pi}{2} + 0.35 \cdot \left(\frac{E}{H} \cdot \tan(\varphi) \right)^{-0.6} \right] \cdot \frac{H}{\tan^2(\varphi)} \cdot d^2 \quad (3.6)$$

The contact load for a conically shaped asperity as a function of the asperity attack angle as calculated using this elastoplastic contact model is shown in Fig. 3.10. The y-axis of this plot covers several orders of magnitude, from $0.1 \mu\text{N}$ to 0.1kN . This is a result of the large range of possible indenter geometries on the x-axis: an attack angle of 0° corresponds to an infinitely wide punch, for which the load will approach infinity. An attack angle of 90° is an infinitely sharp needle, where even a very small load causes a large indentation. It can be seen that for a given asperity with fixed attack angle φ , the contact load increases with the square of the indentation depth.

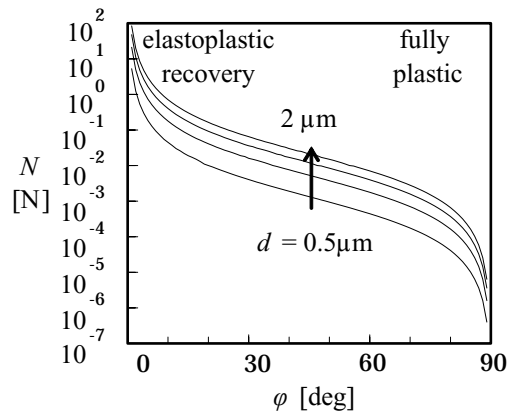


Fig. 3.10: Contact load as a function of the attack angle for various indentation depths of a rigid conical asperity into a nodular cast iron body.

3.2.2.2 Cone with an elliptic cross-section

For a conical shaped asperity with an elliptic cross-section again a representative cone with a spherical base is applied. The volume of this representative cone equals that of the original cone. Provided $\varphi_x \neq 0$ and $\varphi_y \neq 0$ the representative attack angle φ_* is given by:

$$\varphi_* = \text{atan} \left\{ \sqrt{\tan(\varphi_x) \cdot \tan(\varphi_y)} \right\} \quad (3.7)$$

Taking also into account the elasticity of the indenter, incorporated in the reduced Young's modulus E_* (eq. (3.8)) the elastoplastic equations become:

$$E_* = \left(\frac{1-\nu_1^2}{E_1} + \frac{1-\nu_2^2}{E_2} \right)^{-1} \quad (3.8)$$

$$A_{\text{ep}} = \left[\frac{\pi}{2} + 0.7 \cdot \left(\frac{E_*}{H} \cdot \tan(\varphi_*) \right)^{-0.6} \right] \cdot \left(\frac{d}{\tan(\varphi_*)} \right)^2 \quad (3.9)$$

$$N_{\text{ep}} = \left[\frac{\pi}{2} + 0.35 \cdot \left(\frac{E_*}{H} \cdot \tan(\varphi_*) \right)^{-0.6} \right] \cdot \frac{H}{\tan^2(\varphi_*)} \cdot d^2 \quad (3.10)$$

3.2.3 Asperities with a paraboloidal shape

3.2.3.1 Axisymmetric paraboloid

In the case of an axisymmetric paraboloidal shaped indenter, the load-displacement relations for the fully elastic sliding contact are described by the theory of Hertz. Strictly this is only correct for bodies with identical elastic properties, but Johnson [58] and Bhushan [5],[6] indicate that the error made by this simplification is negligible. The elastic contact area and contact load are given by eq. (3.11) and eq. (3.12) respectively.

$$A_e = \pi \cdot R \cdot d \quad (3.11)$$

$$N_e = \frac{4}{3} \cdot E_* \cdot R^{\frac{1}{2}} \cdot d^{\frac{3}{2}} \quad (3.12)$$

With R the radius of the indenting paraboloid. In the case of fully plastic static indentation the contact area is obtained by truncation of the spherical cap (eq. (B.17)). In pure plastic sliding only the front half of the indenter contacts the counter surface and the contact spot has a semi-spherical shape. From the geometry of the asperity a relation for the contact area is simply obtained:

$$A_p = \pi \cdot R \cdot d \quad (3.13)$$

Multiplying this plastic contact area with the average contact pressure, which in fully plastic deformation equals the hardness of the deforming material, gives eq. (3.14) for the fully plastic contact load.

$$N_p = \pi \cdot R \cdot H \cdot d \quad (3.14)$$

In the elastoplastic deformation mode the contact spot slowly transforms from circular to semi circular, i.e. the contact spot is crescent shaped. As the elastoplastic regime extends from the onset of plastic deformation at $d_{e,trans}$ to the beginning of fully plastic deformation at $d_{p,trans}$, the relative elastoplastic indentation depth δ can be defined as:

$$\delta = \frac{d - d_{e,trans}}{d_{p,trans} - d_{e,trans}} \quad (3.15)$$

Similar to the static case the contact area and load can be described by eq. (3.16) and eq. (3.17), from Zhao, Maietta and Chang [118]:

$$A_{ep} = A_e + (A_p - A_e) \cdot (-2 \cdot \delta^3 + 3 \cdot \delta^2) \quad (3.16)$$

$$N_{ep} = \left\{ A_e + (A_p - A_e) \cdot (-2 \cdot \delta^3 + 3 \cdot \delta^2) \right\} \times \left[H - H \cdot (1 - k) \cdot \frac{\ln d_{p,trans} - \ln d}{\ln d_{p,trans} - \ln d_{e,trans}} \right] \quad (3.17)$$

In which k represents the average contact pressure factor as introduced by Tabor [98].

It might be suggested that eq. (3.16) for the elastoplastic contact area is redundant, because the relations between A_c and the indentation depth d as given by eq. (3.11) and A_p and d according to eq. (3.13) are identical, causing the most right term in eq. (3.16) to vanish. However, this is only the case for the special situation of an axi-symmetric paraboloidal or spherical shaped indenter. For paraboloidal shaped asperities with an elliptic base, eqs. (3.11) and (3.14) do not coincide, as will be shown in section 3.2.3.3.

Fig. 3.11 shows the normalised pressure in the contact between a spherical indenter and a flat. At low indentation depths the contact is ideally elastic. With increasing penetration depth the contact pressure starts to deviate from the elastic asymptote. For relatively large indentation depths the plastic asymptote is reached and the contact pressure equals the hardness of the deforming material. The figure clearly shows that the elastoplastic regime provides a smooth transition between the elastic and fully plastic asymptotes.

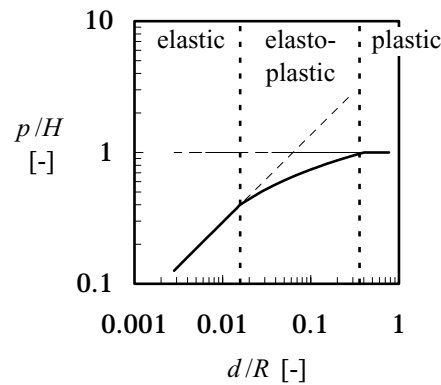


Fig. 3.11: Normalised pressure in sliding as a function of the normalised indentation depth for an elastic-elastoplastic-fully plastic sphere.

3.2.3.2 Transitions

The stress distribution in a sliding contact is quite different from that in a static contact. Explicit equations describing the contact between a sliding spherical indenter and a flat are presented by Hamilton [43]. These equations are reproduced in Appendix B.2. Some results for the equivalent Von Mises stress are shown in Fig. 3.12 for three values of the coefficient of friction. These graphs show the subsurface stress distribution along the centre line of the contact. The x-axis represents the sliding direction of the indenter while the y-axis represents the depth into the material, both normalised with respect to the contact radius a . In the graphs it can be seen that with increasing coefficient of friction μ the location of the maximum stress moves to the front of the indenter and towards the surface.

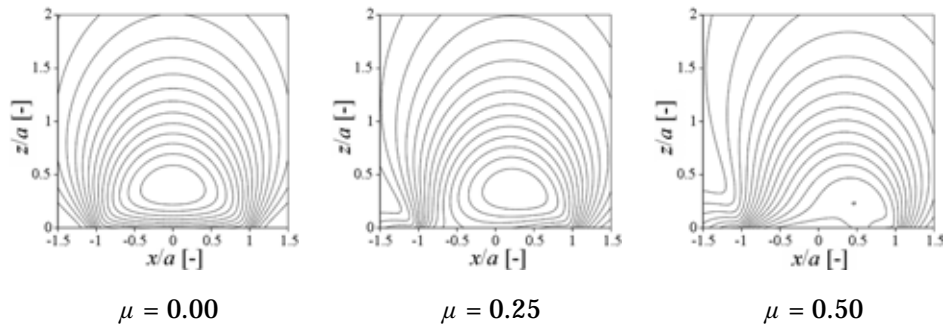


Fig. 3.12: Sub-surface Von Mises stress in sliding contact.

Not only the location but also the absolute value of the maximum Von Mises stress changes with changing coefficient of friction. Consequently, at a higher coefficient of friction, yielding will occur at a lower normal load. The maximum Von Mises stress occurring in the contact as a function of the coefficient of friction as well as the locations of these maxima are plotted in Fig. 3.13(a) and (b). A clear transition is visible: for low values of the coefficient of friction the maximum Von Mises stress is subsurface. When the coefficient of friction surpasses 0.3 the location of the maximum stress is on the surface. Furthermore, in Fig. 3.12 an 'on surface' high-stress region develops at the back of the contact. According to Hamilton this region dominates the stress field when $\mu > 0.25$.

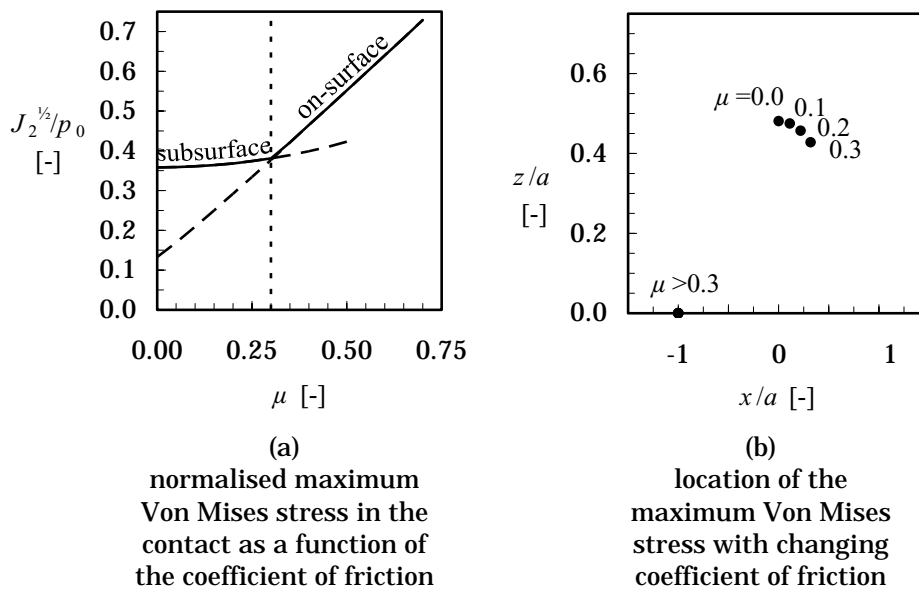


Fig. 3.13: Von Mises stress in the contact.

Similar to the static situation, the transition from pure elastic to the elastoplastic regime occurs at first yield, i.e. when the Von Mises yield parameter $\sqrt{J_2}$ equals $\sqrt{1/3}$ times the yield stress in simple tension.

$$\sqrt{J_2} = \frac{Y}{\sqrt{3}} \quad (3.18)$$

or, with $H = 3 \cdot Y$:

$$\sqrt{J_2} = \frac{H}{3\sqrt{3}} \quad (3.19)$$

Hence, in the case of a sliding paraboloid there is no straightforward solution for the indentation depth at which first yield occurs. The procedure to determine the elastic to elastoplastic transition starts with the calculation of the Von Mises stress. Subsequently, the yield parameter $\sqrt{J_2}$ gives the load at which yield occurs, and using the Hertzian contact model the indentation depth at yield $d_{e,trans}$ can be determined. Fig. 3.14 shows the dimensionless indentation depth $d_{e,trans} / R$ as a function of the coefficient of friction for the contact between a spherical diamond indenter with a radius $R = 25 \mu\text{m}$ and nodular cast iron. A high level of friction in the contact causes an early onset of plastic deformation. It should also be noted that the transition from fully elastic to elasto-plastic deformation occurs at a very low indentation depth. Therefore, in the investigated situation, most contacting asperities will operate in the elastoplastic or fully plastic regime, while the fully elastic regime is relatively unimportant.

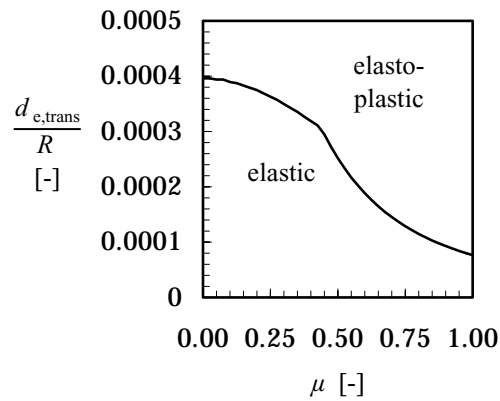


Fig. 3.14: Transitional indentation depth as a function of the coefficient of friction.

In static contact Johnson observed that the contact load at the onset of fully plastic material behaviour equals 400 times the contact load at first yield. Identically, in sliding contact the transition from elastoplastic to fully plastic material behaviour, is assumed to occur when the contact load reaches 400 times the load at initial yield. The load at initial yield is calculated from the $\sqrt{J_2}$ yield criterion after which the elastoplastic to fully plastic transitional indentation depth follows from eq. (3.14).

3.2.3.3 Paraboloid with an elliptic cross-section

The elastic contact between a paraboloidal shaped asperity and a deforming flat is described by eqs. (3.20) and (3.21) (see Hertz [47] and Johnson [58]).

$$A_e = 2 \cdot \pi \cdot R_* \cdot \frac{\alpha_x \cdot \alpha_y}{\gamma} \cdot d \quad (3.20)$$

$$N_e = \frac{4}{3} \cdot \left(\frac{d}{\gamma} \right)^{\frac{3}{2}} \cdot E_* \cdot \sqrt{2 \cdot R_*} \quad (3.21)$$

The reduced radius R_* , the dimensionless radii of the contact spot in x- and y-direction (α_x and α_y respectively) and the dimensionless approach between the two bodies (γ) are defined in eq. (3.22), after Reussner [89] and Moes [79]:

$$\begin{aligned} R_* &= \left(\frac{1}{R_x} + \frac{1}{R_y} \right)^{-1} \\ \alpha_x &= \kappa^{\frac{1}{3}} \cdot \left[\frac{2}{\pi} \cdot \mathbf{E}(1 - \kappa^2) \right]^{\frac{1}{3}} \\ \alpha_y &= \kappa^{-\frac{2}{3}} \cdot \left[\frac{2}{\pi} \cdot \mathbf{E}(1 - \kappa^2) \right]^{\frac{1}{3}} \\ \gamma &= \kappa^{\frac{2}{3}} \cdot \left[\frac{2}{\pi} \cdot \mathbf{E}(1 - \kappa^2) \right]^{\frac{1}{3}} \cdot \frac{2}{\pi} \cdot \mathbf{K}(1 - \kappa^2) \end{aligned} \quad (3.22)$$

with \mathbf{K} and \mathbf{E} the complete elliptic integrals of the first and second kind according to eq. (3.23) and $\kappa = \alpha_x / \alpha_y$ the ellipticity ratio of the contact area.

$$\mathbf{K}(m) = \int_0^{2\pi} \left(1 - m \cdot \sin^2(\psi)\right)^{\frac{1}{2}} d\psi \quad (3.23)$$

$$\mathbf{E}(m) = \int_0^{2\pi} \left(1 - m \cdot \sin^2(\psi)\right)^{\frac{1}{2}} d\psi$$

An approximate relation (Moes [79]) between κ and the gap curvature ratio $\lambda = R_x / R_y$ is given by eq. (3.24):

$$\kappa \approx \left[1 + \sqrt{\frac{\lambda}{2} \cdot \ln(16 \cdot \lambda)} - \sqrt{\ln(4)} + \ln(\lambda^{-0.16}) \right]^{-1} \quad (3.24)$$

for $0 < \lambda \leq 1$

In the case of fully plastic material behaviour the contact area is again obtained from the geometry of the asperity, by truncation of the paraboloidal contacting cap. This extension to paraboloidal shaped asperities results in:

$$A_p = \pi \cdot \sqrt{R_x \cdot R_y} \cdot d \quad (3.25)$$

$$N_p = \pi \cdot \sqrt{R_x \cdot R_y} \cdot H \cdot d \quad (3.26)$$

And similar to the axisymmetric situation, the transitional elastoplastic material behaviour is given by eqs. (3.27) and (3.28).

$$A_{ep} = A_e + (A_p - A_e) \cdot (-2 \cdot \delta^3 + 3 \cdot \delta^2) \quad (3.27)$$

$$N_{ep} = \left\{ A_e + (A_p - A_e) \cdot (-2 \cdot \delta^3 + 3 \cdot \delta^2) \right\} \times \left[H - H \cdot (1 - k) \cdot \frac{\ln d_{p,trans} - \ln d}{\ln d_{p,trans} - \ln d_{e,trans}} \right] \quad (3.28)$$

3.2.3.4 Transitions

Similar to the axisymmetric situation, first yield occurs when the normalised Von Mises yield parameter equals:

$$\sqrt{J_2} = \frac{H}{3\sqrt{3}} \quad (3.29)$$

And again it is assumed that full plasticity is reached when the contact load equals 400 times the load at first yield.

$$N_{p,trans} = 400 \cdot N_{e,trans} \quad (3.30)$$

The plot shown in Fig. 3.15 illustrates the effect of ellipticity of the asperity on the contact area. In all cases the indenter has a reduced radius of $R_* = 25 \mu\text{m}$. Asperities with an ellipticity ratio $\lambda > 0.5$ behave similar to the axisymmetric ($\lambda = 1$) asperity. Only for highly anisotropic asperities the contact behaviour clearly deviates. The filled dots represent the indentation depth at which the elastoplastic to fully plastic material transition occurs. This transitional depth also remains approximately constant when $\lambda < 0.5$. For more elliptic asperities the transition occurs at a smaller indentation depth. It can be concluded that, as long as the asperity is not extremely elliptic, the ellipticity only has a marginal effect.

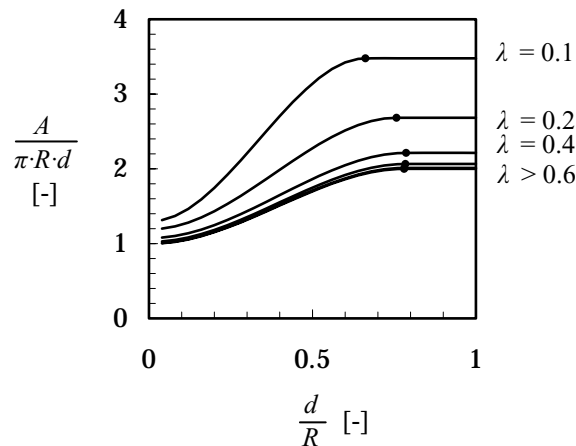


Fig. 3.15: Contact area as a function of indentation depth for anisotropic asperities.

3.2.4 Layered surfaces

Often hard surface layers are applied to increase the wear resistance of a component. The contact behaviour of such a coated system is determined by the combination of substrate and layers. To describe the contact behaviour, the material parameters should be extended to incorporate these layers.

Below, both the effective Young's modulus and the effective hardness for coated substrates are discussed. The altered contact behaviour due to a coating is illustrated with some calculations on nodular cast iron with a 5 μm TiN coating.

3.2.4.1 Young's modulus

The elastic behaviour of both contact partners in a tribological system is enclosed in the reduced Young's modulus E_* which is repeated below for the contact between a tool and an asperity:

$$E_* = \left(\frac{1-\nu_{\text{asp}}^2}{E_{\text{asp}}} + \frac{1-\nu_{\text{tool}}^2}{E_{\text{tool}}} \right)^{-1} \quad (3.31)$$

For a tool covered with a number of hard surface layers, E_{tool} is composed of the elastic properties of the substrate and the surface layers. Visscher [112] follows the approach suggested by Gao et al. [38] for the effective Young's modulus E_{eff} of a substrate s covered with n thin layers, with $i = 1$ for the top layer and $i = n$ for the bottom layer.

$$\frac{1-\nu_{\text{eff}}^2}{E_{\text{eff}}} = \frac{1 - \left(\nu_s + \sum_{i=1}^{n-1} \{I_1 \cdot (\nu_i - \nu_{i+1})\} - I_1 \cdot (\nu_n - \nu_s) \right)}{\frac{E_s}{1+\nu_s} + \sum_{i=1}^{n-1} \left\{ I_0 \cdot \left(\frac{E_i}{1+\nu_i} - \frac{E_{i+1}}{1+\nu_{i+1}} \right) \right\} + I_0 \cdot \left(\frac{E_n}{1+\nu_n} - \frac{E_s}{1+\nu_s} \right)} \quad (3.32)$$

in which I_0 and I_1 are defined as:

$$I_0 = \frac{2}{\pi} \cdot \text{atan}(\Gamma_i) + \frac{1}{2 \cdot \pi \cdot (1-\nu_l)} \cdot \left\{ (1-2 \cdot \nu_l) \cdot \Gamma_i \cdot \ln \frac{1+\Gamma_i^2}{\Gamma_i^2} - \frac{\Gamma_i^2}{1+\Gamma_i^2} \right\} \quad (3.33)$$

$$I_1 = \frac{2}{\pi} \cdot \text{atan}(\Gamma_i) + \frac{1}{\pi} \cdot \Gamma_i \cdot \ln \frac{1+\Gamma_i^2}{\Gamma_i^2} \quad (3.34)$$

where ν_l represents the average Poisson's ratio of all layers and Γ_i is a parameter indicating the relative depth of layer i , according to eq. (3.35), in which t represents the thickness of the layer and a_x the contact radius. I_0 and I_1 are plotted in Fig. 3.16.

$$\Gamma_i = \sum_{k=1}^i \frac{t_k}{a_x} \quad (3.35)$$

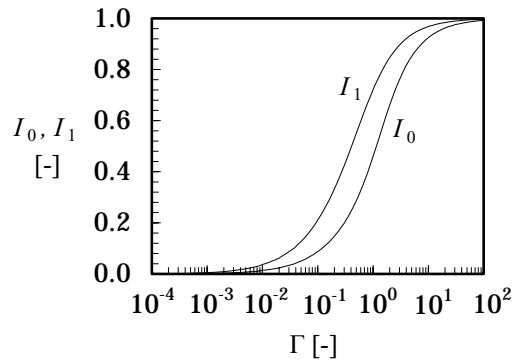


Fig. 3.16: Weighing functions I_0 and I_1 as a function of the Γ parameter.

Fig. 3.17 shows the effective Young's modulus as a function of the relative layer thickness. This relative layer thickness is defined as the ratio of the thickness of the layer t and the indentation depth d . For low indentation depths the contact behaviour is dominated by the top-layer. With increasing depth the more compliant substrate becomes important, causing the effective Young's modulus to drop. At a very large indentation depth the effective Young's modulus approaches the asymptote $E_s/(1-\nu_s^2)$ given by the substrate.

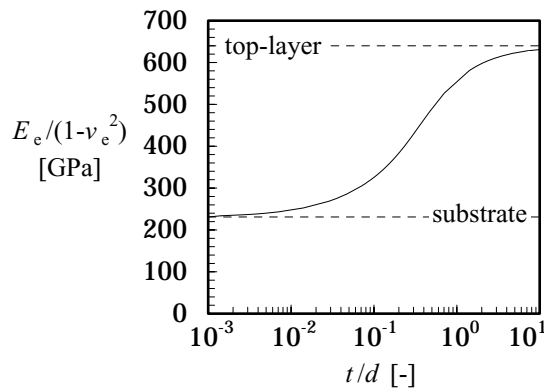


Fig. 3.17: Effective Young's modulus as a function of the relative indentation depth for a nodular cast iron substrate with a 5 μm TiN layer.

3.2.4.2 Hardness

Generally, the effective hardness H_{eff} is calculated by combining the hardness of the substrate (H_s) and the hardness of the coating (H_c) using some kind of rule of mixtures.

$$H_{\text{eff}} = \Xi_s \cdot H_s + \Xi_c \cdot H_c \quad (3.36)$$

In this relation the coefficients Ξ_s and Ξ_c represent the share of the substrate and the coating respectively, and their sum equals 1. An example of this is the work of Jönsson and Hogmark [59], who suggested these fractions to depend on the ratio of thickness of the coating and radius of the indentation. Several other models exist, see for instance the overview article by Puchi-Cabrera [86].

Fig. 3.18 shows several models for the effective hardness of a single coated surface as a function of the ratio of coating thickness t and indentation depth d . The left part of the x-axis shows the region where t/d is small, i.e. the indentation depth is significantly larger than the thickness of the coating. In this case the effective hardness of the body equals the hardness of the substrate. On the right hand side of the x-axis the coating thickness is larger than the indentation depth and the substrate only has a small influence. The models marked (a) and (b) clearly are developed for large indentation depths, they fail when the coating thickness and the indentation depth are of the same order of magnitude. The models designated (c), (d) and (e) show a gradual transition from pure dependency of the layer to solid substrate behaviour with decreasing t/d ratio.

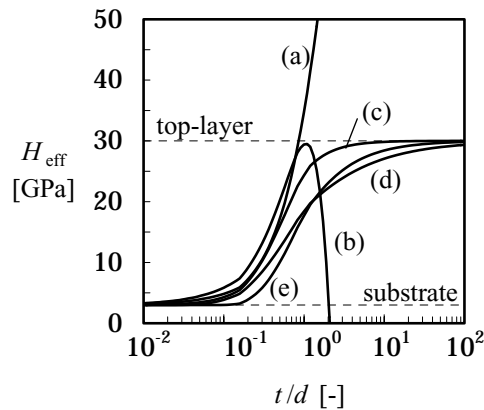


Fig. 3.18: Effective hardness of a single layered body.
 (a) Burnett and Rickerby [12],[13], (b) Jönsson [59]
 (c) Tuck, Korsunsky and Bull [103], (d) Puchi-Cabrera [86]
 (e) Malzbender, De With and Den Toonder [74]

In this research a relatively simple model, based on the work of Malzbender, De With and Den Toonder [74] is applied. The effective hardness calculated using this model is given by eq. (3.37). The effective hardness H_{eff} is described by an exponential curve between the hardness of the substrate H_s and that of the coating H_c . The factor 0.65 is obtained by Malzbender et al. using curve fits of experimental results. The relation between H_{eff} and t/d is plotted as line (e) in Fig. 3.18.

$$H_{\text{eff}} = H_s + (H_c - H_s) \cdot e^{-0.65 \cdot \frac{d}{t}} \quad (3.37)$$

3.2.4.3 Subsurface stresses

The elastic stress field in the contact between a spherical indenter and a layered body can only be solved analytically when the substrate and the layer have the same Young's modulus. When this is not the case a least squares iterative approach for the quasi-static sliding contact can be applied, see O'Sullivan and King [84]. From their work it can be concluded that the stress field depends on the ratio $E_{\text{layer}} / E_{\text{substrate}}$. A relatively compliant coating results in a low value of the maximum Von Mises stress in the contact. Therefore, coatings with a low Young's modulus are beneficial in many engineering contacts. However, usually coating materials having the required high hardness also are relatively stiff, causing an increase of the maximum Von Mises contact stress and therefore an earlier onset of plastic deformation. This is illustrated in the work of Michler and Blank [77], who developed failure maps for several hard coatings on steel substrates. They conclude that the application of a layer with a high stiffness is only beneficial when the layer is relatively thick.

3.2.5 Summary of sliding contact

In Table 3.2 the equations for the sliding contact situation between a cone with an elliptic cross-section or a paraboloidal shaped asperity and a deforming semi-infinite body are summarised. In Fig. 3.19, Fig. 3.20 and Fig. 3.21 the contact behaviour of conical and of paraboloidal shaped asperities is compared by means of some calculations using the material parameters of nodular cast iron. The conical shaped asperities have attack angles ranging from $\varphi_* = 2^\circ, 10^\circ$ and 40° while the paraboloidal shaped asperities have a reduced radius $R_* = 5 \mu\text{m}, 10 \mu\text{m}$ and $25 \mu\text{m}$. The figures show that for small indentation depths both the load carried by the spherical indenters as well as the contact area exceed the values obtained for conical indenters. However, the rate at which the area and load change with increasing penetration depth is higher for conical shaped asperities, causing the contact conditions to intensify more rapidly. Fig. 3.20 and Fig. 3.21 show the influence of coatings.

Applying a hard surface layer results in an increased contact load at given indentation depth. This means that the load bearing capacity is increased. This aspect is clearly visible for paraboloidal shaped asperities in the fully plastic deformation regime.

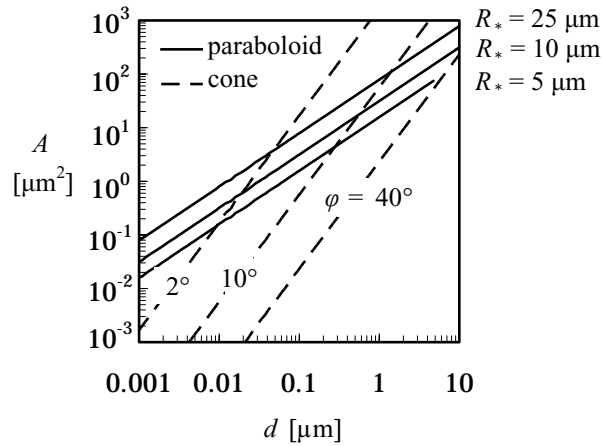


Fig. 3.19: Contact area-displacement relations for some conical and paraboloidal shaped asperities.

3.3 Discussion and conclusions

3.3.1 Deformation modes

In this chapter a model for the micro-level contact between a single sliding indenter or asperity and a semi-infinite deforming layered flat body is derived. The relations between contact load and indentation depth are derived for both elliptic-conical and paraboloidal shaped asperities. In a single asperity contact three deformation modes can be distinguished: pure elastic, elastoplastic and fully plastic. In the investigated situation of metal forming the pure elastic deformation mode is of minor importance. It only occurs for extremely blunt conical indenters and for paraboloidal shaped asperities at very small indentation depths. The elastoplastic deformation regime provides a smooth transition between the pure elastic and fully plastic asymptotes. In this regime the material behaviour of the contact partners is a combination of elastic and plastic processes. When there is a plastic component in the deformation mode, at least a part of the total deformation is permanent and a scratch is drawn in the softer material. In the fully plastic mode the contact pressure equals the hardness of the deforming material.

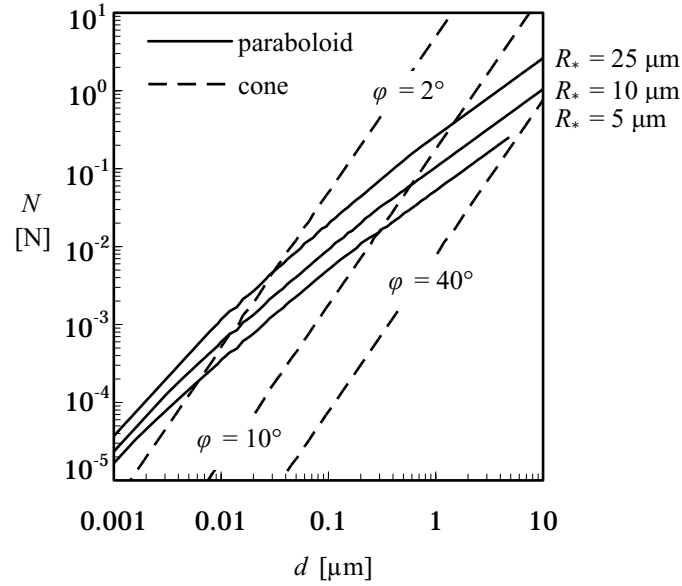


Fig. 3.20: Load-displacement relation for some conical and paraboloidal shaped asperities in contact with an uncoated cast iron substrate.

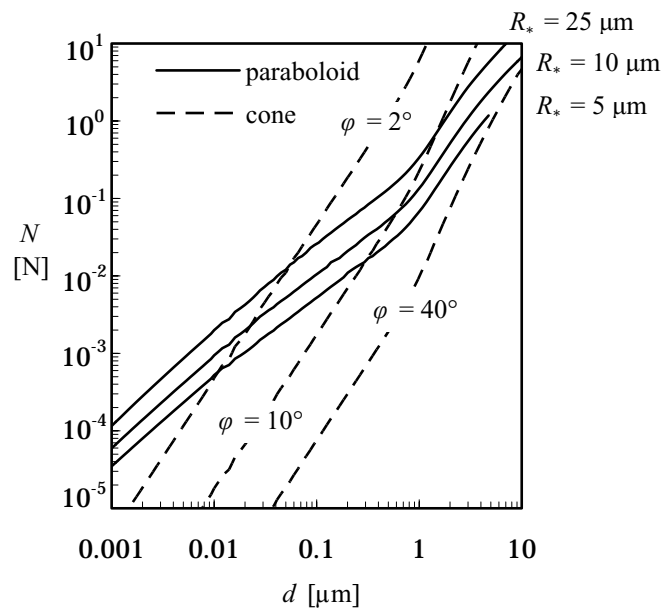
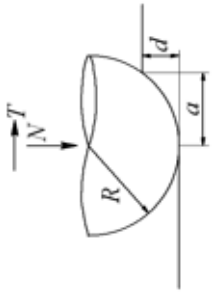
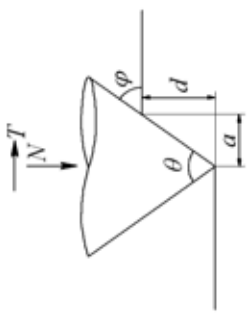


Fig. 3.21: Load-displacement relation for some conical and paraboloidal shaped asperities in contact with a $5 \mu\text{m}$ TiN coated cast iron substrate.

Table 3.2: Summary of equations for the sliding contact situation.

		
elastic		n.a.
transition	n.a.	n.a.
elastoplastic	$A_{ep} = \left[\frac{\pi}{2} + 0.7 \cdot \left(\frac{E_*}{H} \cdot \tan(\varphi_*) \right)^{-0.6} \right] \cdot \left(\frac{d}{\tan(\varphi_*)} \right)^2$ $N_{ep} = \left[\frac{\pi}{2} + 0.35 \cdot \left(\frac{E_*}{H} \cdot \tan(\varphi_*) \right)^{-0.6} \right] \cdot \frac{H}{\tan^2(\varphi_*)} \cdot d^2$	$A_e = 2 \cdot \pi \cdot R_* \cdot \alpha_x \cdot \alpha_y \cdot d \cdot \gamma^{-1}$ $N_e = \frac{4}{3} \cdot \left(\frac{d}{\gamma} \right)^{\frac{3}{2}} \cdot E_* \cdot \sqrt{2 \cdot R_*}$
transition	n.a.	$N_{p,trans} = 400 \cdot N_{e,trans}$
fully plastic	$A_p = \frac{\pi}{2} \cdot \left[d \cdot \tan^{-1}(\varphi_*) \right]^2$ $N_p = A_p \cdot H$	from $\sqrt{J_2}$ criterion $A_{ep} = A_e + (A_p - A_e) \cdot (-2 \cdot \delta^3 + 3 \cdot \delta^2)$ $N_{ep} = \left\{ A_e + (A_p - A_e) \cdot (-2 \cdot \delta^3 + 3 \cdot \delta^2) \right\} \times \left[H - H \cdot (1 - k) \cdot \frac{\ln d_{p,trans} - \ln d}{\ln d_{p,trans} - \ln d_{e,trans}} \right]$ $A_p = \pi \cdot \sqrt{R_x \cdot R_y} \cdot d$ $N_p = A_p \cdot H$

3.3.2 Asperity geometry and ellipticity

In all results presented in this chapter a large influence of the asperity geometry on the contact behaviour is observed. For conical shaped asperities the contact load scales with the square of the tangent of its top angle. In the case of paraboloidal shaped asperities the plastic contact load increases with the square root of the indenter geometry while the relation between size and elastic load is linear. Therefore, an accurate determination of the asperity geometry is very important.

Ellipticity of the asperities only has a minor effect on the contact behaviour. The equations describing the contact are altered somewhat by taking a representative asperity which is axisymmetric. Also on the transitions between the contact modes ellipticity only has a small influence. For highly elliptic paraboloidal shaped asperities the transition to fully plastic deformation occurs at a lower indentation depth. However, the ellipticity of the asperity should be taken into account because in Chapter 4 it will be shown that there is a significant influence of the ellipticity on the wear behaviour.

3.3.3 Surface layers

The application of a thin hard surface layer on a substrate increases the load bearing capacity of the body, provided that the layer has sufficient thickness. This means that the indentation depth of an asperity into a coated body will be smaller at an equal load. Additionally, many materials commonly applied as hard surface layers show low shear stresses at the interface, causing a decrease in the coefficient of friction in the tribological system which results in a smaller sliding component in subsurface stress and therefore a lower value of the maximum Von Mises stress. However, a stiff layer causes the maximum Von Mises stress in the body to increase.

When the indentation depth is small compared to the layer thickness, the contact behaviour is dominated by the hard top layer. For larger indentation depths the material behaviour depends on the combination of substrate and layer. The results presented confirm the rule of thumb that the combined layer-substrate material behaviour should be included in the contact analysis when the indentation depth surpasses ten percent of the layer thickness.

Chapter 4

Single Asperity Abrasive Wear

4.1 Introduction

In the previous chapter a model for the contact between a sliding rigid asperity and a softer deforming body was derived. When the contact pressure is high enough for elastoplastic or fully plastic deformation to occur, the sliding action results in a groove in the deforming surface, as shown in Fig. 4.1. This chapter focuses on the abrasive wear in a single asperity contact. The abrasive action of a single asperity is described, depending on the scratched material, the dimensions of the asperity and the indentation depth, with the aim to extend this model to rough surfaces, as will be discussed in Chapter 5.

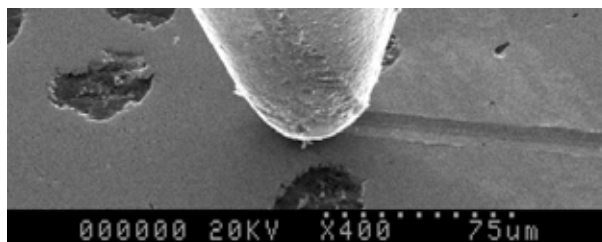


Fig. 4.1: SEM photograph of the sliding action of a single asperity.

The material behaviour in scratching is rather complicated and involves dynamic contact phenomena, large plastic strains and fracture. Several models have been developed that describe the groove formation by a single asperity that scratches through a softer surface. These models range from analytical models (e.g. Challen and Oxley [17] and Zum Gahr [121]) to finite element models (Dillingh [27] and Kral and Komvopoulos [68]).

4.2 Modelling abrasive wear

4.2.1 Geometry of a wear scar

Due to the single pass scratching action of an asperity a groove is formed in the softer surface. Fig. 4.2 shows a schematic illustration of the cross-section of a wear scar.

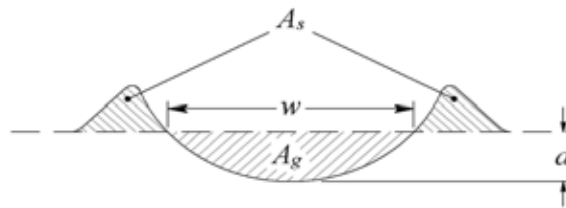


Fig. 4.2: Schematic illustration of the cross-section of a wear scar.

The wear scar consists of a groove flanked by two shoulders. Part of the material from the groove is transferred to these shoulders while the rest is actually removed from the surface as wear debris. The proportion of actually removed material is characterised by the degree of wear parameter ζ defined in eq. (4.1).

$$\zeta = \frac{A_g - A_s}{A_g} \quad (4.1)$$

4.2.2 Slip-line models

Challen and Oxley [17] described the two-dimensional sliding contact between a rigid wedge and a softer perfectly plastic deforming surface using slip-line models. According to their theory, the three different situations depicted in Fig. 4.3 and Fig. 4.4 can occur:

- Rubbing: the hard wedge slides or rubs over the softer material.
- Wearing: a wave is formed in front of the wedge, like a prow.
- Cutting: the hard wedge cuts through the material and a chip is formed.

The rubbing model as shown in Fig. 4.3 describes the sliding contact between a hard wedge shaped asperity and a softer one. The surfaces slide along interface ED and although there is contact and hence friction, in this model no material removal occurs. The input variables are a geometrical parameter, e.g. the asperity attack angle φ , the normal load on the contact and the interfacial friction factor f_w , a parameter representing the strength of the interface between the hard asperity and the softer material. When the rubbing model

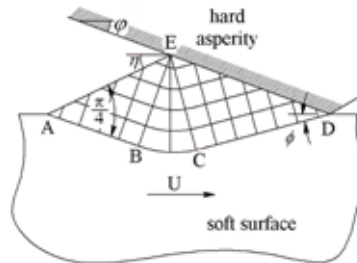


Fig. 4.3: Challen and Oxley's rubbing model [17].

can not be applied, e.g. when the geometrical constraints are not satisfied anymore, one of the alternatives is that a prow is formed in front of the hard asperity. This behaviour is described by the so-called wear model of Fig. 4.3(b). During sliding the prow increases in size until it breaks away and the formation of a new prow begins. The cycle of formation, growth, fracture and removal as a wear particle is a non-steady state dynamic process and hence no velocity field for this situation can be modelled. However, by neglecting a velocity field, it is possible to model the stresses and strains using a slip-line field. The difference with the rubbing model is that sliding occurs along the (former) interface AD instead of the interface ED. The third possibility is the cutting regime, as shown in Fig. 4.3(c). Cutting occurs when the rubbing model is not applicable and the asperity attack angle φ exceeds 45° . In this situation a chip is actually removed from the soft surface, resulting in severe abrasive wear.

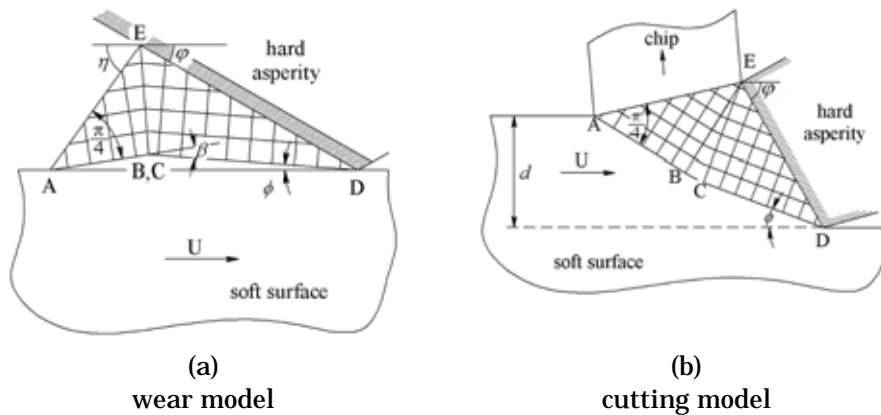


Fig. 4.4: Challen and Oxley's [17] slip-line models with material removal.

Based on the initial paper [17] in which two-dimensional rigid wedges were discussed, Challen, Oxley and co-workers presented a series of extensions ([18] - [22]), for example by including work hardening [18] and cylindrical shaped asperities using chord models [19].

Slip-line models are also discussed by a number of other researchers, see for instance Black et al. [8], [9], Bressan et al. [10] and Busquet and Torrance [14], [15]. The (quasi-) upperbound solution given by slip-line models generally provides an accurate prediction of the forces and the energy that is involved in the wear process. However, the geometrical predictions of upperbound models are known to fail significantly, see for instance Williams [115]. This is also illustrated in Fig. 4.5, which is a graphical representation of data presented by Xie and Williams [117]. In this figure the specific wear rate k_{calc} as calculated using slip-line models is compared to experimental wear rates k_{exp} obtained by Torrance and d'Art [101]. It appears that slip-line models underestimate the volumetric wear significantly.

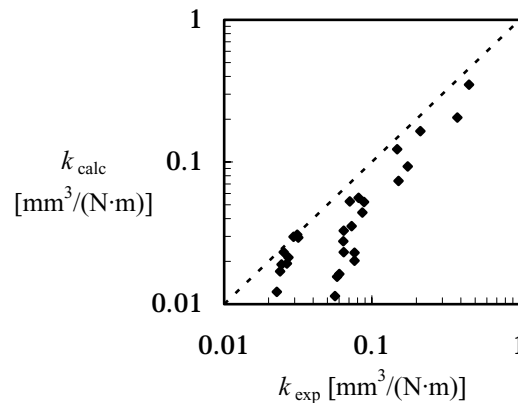


Fig. 4.5: Comparison between experimentally obtained wear rates and the values calculated using a slip-line model.

4.2.3 Abrasive wear mode map

Although the geometrical results of slip-line models are not accurate, the models clearly define the possible abrasive wear regimes and the transitions between them. In a series of papers, Kato and co-workers ([48]-[50],[61],[64]) translated the results obtained for the two-dimensional wedges modelled by Challen and Oxley for application on three-dimensional hemispherical asperities. They replaced the wedge attack angle φ by the degree of penetration D_p , defined according to eq. (4.2) as the indentation depth d of the asperity divided by the contact radius a , see also Fig. 4.6.

$$D_p = \frac{d}{a} \quad (4.2)$$

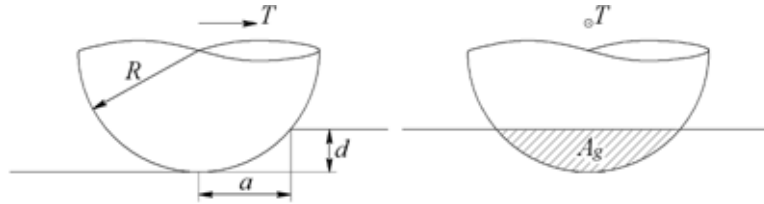


Fig. 4.6: Scratching hemispherical asperity.

Based on single asperity scratch experiments on several materials, Kato and Hokkirigawa [61] constructed the abrasive wear mode map shown in Fig. 4.7. In this diagram the three possible abrasive wear modes, ploughing, wedge formation and cutting, are mapped as a function of the adhesive properties of the contact, represented by the relative strength of the interface f_{tr} and the severity of contact, quantified by the degree of penetration D_p . f_{tr} is defined according to eq. (4.3) as the quotient of the shear strength of the interface τ and the shear strength of the deforming contact partner k .

$$f_{tr} = \frac{\tau}{k} \quad (4.3)$$

The transitions between the wear modes are calculated from Challen and Oxley's slip-line models, by assuming $D_p = c \cdot \tan(\varphi)$. A good correlation between the calculated transitions and the experimental results was found by taking $c = 0.8$. Ploughing, wedge formation and cutting are the three-dimensional equivalents of the rubbing, wearing and cutting regimes modelled by Challen and Oxley.

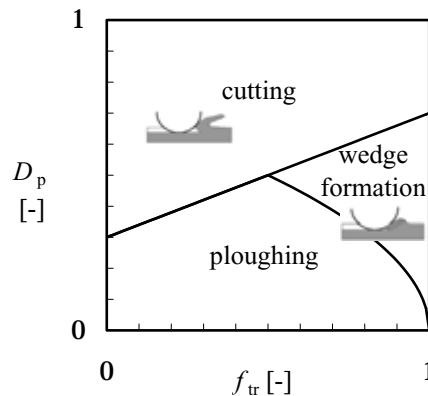


Fig. 4.7: Abrasive wear mode map, from Kato and Hokkirigawa [61].

4.2.4 Degree of wear

According to Zum Gahr [120], each of the three abrasive wear regimes results in a characteristic cross-section of the wear scar in the deforming surface, as schematically shown in Fig. 4.8. In the ploughing regime of Fig. 4.8(a) no volumetric wear occurs, i.e. all material from the scratch is transferred to the side ridges. The corresponding value for the degree of wear $\zeta = 0$. The wedge formation regime is an intermediate stage where a prow is formed in front of the indenter. As discussed before, the repeated formation, growth and removal of the prow in this regime is an unsteady dynamic process, resulting in a wide spread of values for ζ and a wear scar with some shoulders is formed, as shown in Fig. 4.8(b). In cutting most of the material from the wear groove is removed from the surface and ζ approaches 1, as shown in Fig. 4.8(c). Hokkirigawa and Kato [49] reported the values for the degree of wear ζ listed in Table 4.1. Because the values show a relatively large spread, they suggest application of the average values.

Table 4.1: Values for the degree of wear in the abrasive wear modes [49].

Wear mode	Degree of wear ζ [-]	
	Range	Average value
Ploughing	0	0
Wedge formation	0.20 – 0.80	0.50
Cutting	0.80 – 0.95	0.875

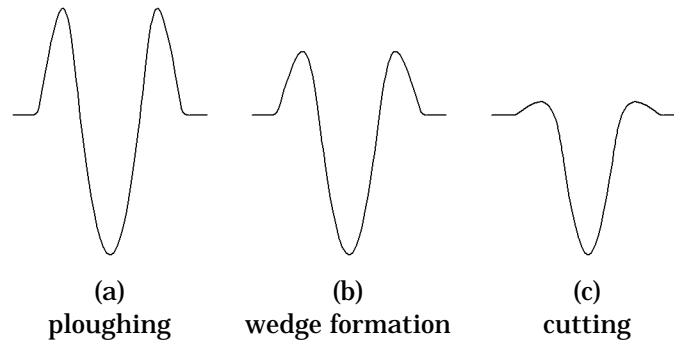


Fig. 4.8: Schematic impression of the geometry of the resulting wear scar in the different wear regimes (not to scale).

For a given asperity geometry and contact conditions, the abrasive wear mode diagram maps the wear mode in which the asperity operates. Each of the three possible wear modes represents a characteristic value of the degree of wear, and by multiplying the degree of wear and the frontal area of the scratching asperity the volumetric wear per sliding distance is obtained.

Hence the volumetric wear per sliding distance Ψ due to the scratching motion of a spherical asperity depends on the size of the asperity, the indentation depth and the wear parameter ζ . An expression for Ψ is given in eq. (4.4), with A_g the frontal area of the scratching part of the asperity.

$$\Psi = \frac{V}{L} \approx \zeta \cdot A_g \quad (4.4)$$

4.2.5 Theoretical extension to other asperity shapes

Until so far the discussion on wear has merely focussed on spherically shaped indenters. However, in the discussed contact model both spheres and cones were applied. Furthermore, the asperity might have an elliptic base and an orientation with respect to the sliding direction. The theory has to be extended to meet these shapes. Indenters with a elliptic paraboloidal shape or elliptic conical shape are, to the author's knowledge, not commercially available.

A translation to ellipticity of the asperities is made by adjusting the value of the degree of penetration and by introducing the orientation β of the asperity with respect to the sliding direction (Fig. 4.9). It is assumed that except its influence on the degree of penetration and hence on ζ , the orientation has no additional effects on the wear volume.

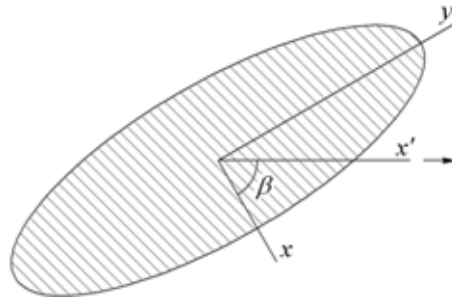


Fig. 4.9: Orientation of the asperity with respect to the sliding direction x' .

For an asperity with an elliptic base the semi-axis of the contact spot in sliding direction $a_{x'}$ can be expressed in terms of the semi-major and semi-minor axes a_x and a_y of the contact spot and the orientation of the asperity, represented by the angle β between the sliding direction and the minor axis of the contact ellipse:

$$a_{x'} = \sqrt{\frac{a_x^2 \cdot a_y^2}{a_x^2 \cdot \sin^2 \beta + a_y^2 \cdot \cos^2 \beta}} \quad (4.5)$$

4.2.5.1 Elliptical paraboloid

The degree of penetration according to Fig. 4.6 was defined in eq. (4.2) as the ratio of the indentation depth and the semi-axis of the contact spot. With the expression for the semi-axis $a_{x'}$ in sliding direction (eq. (4.5)), the degree of penetration for a paraboloidal shaped asperity with an elliptic base becomes:

$$D_p = \frac{d}{\sqrt{\frac{a_x^2 \cdot a_y^2}{a_x^2 \cdot \sin^2 \beta + a_y^2 \cdot \cos^2 \beta}}} \quad (4.6)$$

4.2.5.2 Elliptic cone

The abrasive action of conically shaped asperities follows directly from the abrasive wear mode map of Kato and Hokkirigawa, as shown in Fig. 4.7. The attack angle of a conical asperity with an elliptic base is given in eq. (4.7).

$$\varphi_{x'} = \operatorname{atan}\left(\frac{d}{a_{x'}}\right) = \operatorname{atan}\left(\frac{d}{\sqrt{\frac{a_x^2 \cdot a_y^2}{a_x^2 \cdot \sin^2 \beta + a_y^2 \cdot \cos^2 \beta}}}\right) \quad (4.7)$$

4.2.6 Discussion on modelling wear

Although describing abrasive wear phenomena using the abrasive wear diagram in its present form is possible, there are several considerable deficiencies:

- because the volumetric wear depends linearly on the degree of wear, selecting the correct value for ζ is important.
- the transitions between the wear modes in the diagram are sudden, i.e. a minor mistake in the determination of the values of f_{tr} and D_p might lead to a large error in the calculated wear volume.
- particularly in the wedge formation regime the value of ζ falls within a wide range, possibly leading to a substantial error of the calculated volumetric wear.
- the three wear modes are assumed to occur separately, while it has been shown by several researchers (c.f. [63], [73]) that often several wear modes take place simultaneously.
- determining the correct quantitative value for the relative strength of the contact f_{tr} is difficult, as this simple parameter incorporates a multitude of properties, including the lubrication condition in the contact, boundary

layers, material properties like ductility and fracture toughness and environmental conditions.

Jiang and Arnell [57] tried to solve some of these problems by including a gradual increase of ζ in the wedge formation regime based on a low cycle fatigue mechanism. However, the physical interpretation of such a mechanism is unclear as the model is applied to single pass scratching and hence the fatigue life of the surface in contact is set to 1 cycle.

The representation of data as shown in Fig. 4.10 provides a system dependent relation between the degree of wear ζ and the degree of penetration D_p . With this representation of the experimental data it is possible to get around most of the deficiencies mentioned before. In this graph the measured degree of wear is plotted as a function of the degree of penetration for the contact between a spherical shaped rigid diamond indenter and ball bearing steel specimens with various heat treatments. The numerical values next to the curves indicate the hardness of the specimens (in [MPa]), as measured using a Vickers hardness indenter. For low values of the degree of penetration, the degree of wear $\zeta = 0$. With increasing degree of penetration the degree of wear increases following an S-shaped curve and levels off towards a maximum value ζ_{\max} .

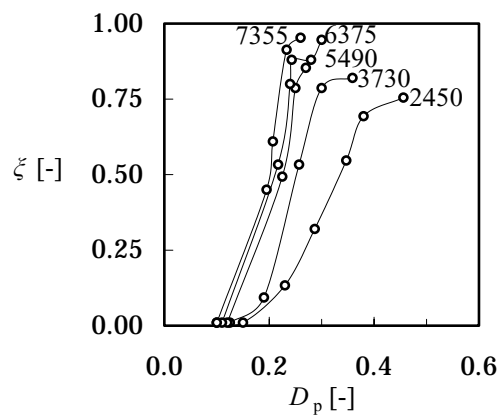


Fig. 4.10: Degree of wear as a function of the degree of penetration for heat treated tool steels with different hardness, ranging from 2.45 to 7.3 GPa. From Hokkirigawa and Kato [48].

4.3 SEM experiments

The theory presented in the preceding is developed and experimentally validated for ball bearing steel, which is a homogeneous metal. For inhomogeneous materials, like nodular cast iron, the situation is more complicated. Therefore, the wear behaviour of nodular cast iron in sliding contact with a hard asperity is empirically modelled using experiments on the SEM pin-on-disk set-up of the tribology laboratory of Tohoku University in Japan. This set-up can be placed inside the chamber of a scanning electron microscope, enabling in-situ observation of the wear process.

4.3.1 Experimental set-up

Fig. 4.11 shows a schematic illustration of the experimental set-up. A photographic impression of this tribometer can be found in Appendix C.1. The single asperity is represented by a static diamond indenter that is in contact with a rotating disk. Indenters with a radius $R = 25 \mu\text{m}$ are applied. The initial surface roughness of the disk specimens is $R_q = 0.05 \mu\text{m}$. More experimental parameters are given in Table 4.2. The pin-disk contact is loaded by compressing the spring using the nut. The experiments are executed inside a scanning electron microscope, at a pressure of 10^{-6} Torr ($\approx 10^{-4}$ Pa).

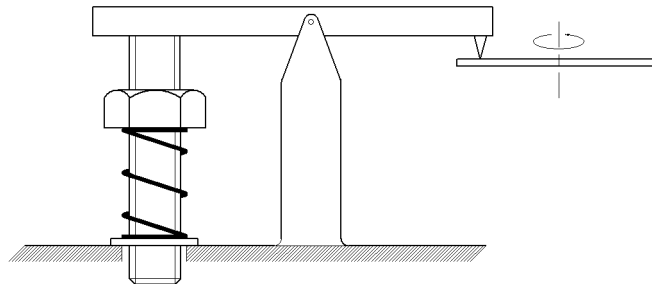


Fig. 4.11: Experimental set-up in SEM scratching experiments.

Each disk specimen is used for a number of experiments and therefore tracks are drawn at several radii. Because the rotational speed of the specimen is kept constant, scratching a track on a different diameter results in a different scratching velocity. According to Xie and Williams [116] the influence of the velocity on the wear rate may be neglected in low velocity abrasion.

Table 4.2: SEM-scratch test set-up.

Contact load	> 0.05 N
Rotational speed	0.01 rad·s ⁻¹
Scratch-track radius	8 – 12 mm
Scratching velocity	80 – 120 μm·s ⁻¹

4.3.1.1 Specimens

Nodular cast iron specimens with a range of hard surface layers are tested. The tested materials are listed in Table 4.3. The metal-carbon (MC) and chromium nitride (CrN) coatings have a thickness t in the order of several microns. Therefore, the substrate will have a considerable influence in the experimental results. The stellite clad layer (clad) has a thickness of about 1 mm and hence the substrate has no effect on the contact behaviour. For both the specimen coated with the stellite layer as well as the specimen with the clad + chromium nitride duplex layer the thick stellite layer can be considered as the substrate.

Table 4.3: Tested materials in the SEM tribo-system.

Substrate material	Coating	Coating process	Thickness [μm]
GGG70L	none	-	-
GGG70L	Metal-Carbon (MC)	PVD	4
GGG70L	Chromium Nitride (CrN)	PVD	4
GGG70L	Stellite 6	Laser cladding	10 ³
GGG70L	Stellite 6 + Chromium Nitride	Laser cladding + PVD	10 ³ + 6

The effective hardness of a coated surface was discussed in section 3.2.3. In Fig. 4.12 the effective hardness of the tested surfaces as a function of the degree of penetration is plotted.

4.3.1.2 Indenters

Diamond was applied as the pin-material because its Young's modulus is significantly higher than the Young's modulus of the tested materials. Hence the indenter may be considered rigid. The applied indenters have a conical shape with a hemispherical tip radius of $R = 25 \mu\text{m}$ and a tip angle $\theta = 30^\circ$.

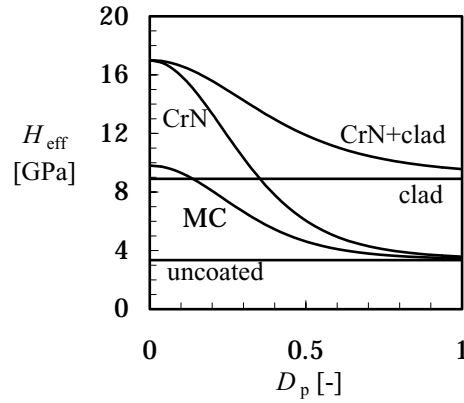


Fig. 4.12: Effective hardness of the tested surfaces as a function of the degree of penetration, for an indenter with radius $R = 25 \mu\text{m}$.

The maximum indentation depth for this indenter is given by eq. (4.8). Until this depth the contacting part of the indenting tip can be assumed to be spherical. For larger indentations part of the indentation is made by the conical body.

$$d_{\text{max}} = R - \sqrt{\frac{R^2}{\tan^2(\varphi_c) + 1}} \quad (4.8)$$

In this equation φ_c represents the attack angle of the conical part ($\varphi_c = 90^\circ - 0.5 \cdot \theta$). Solving eq. (4.8) for the applied indenters gives a maximum indentation depth $d_{\text{max}} = 18.5 \mu\text{m}$.

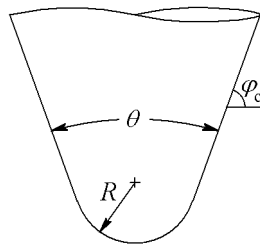


Fig. 4.13: Geometry of the indenter.

4.3.1.3 Testing procedure

The samples are cleaned by submerging in acetone in an ultrasonic bath for twelve minutes. Subsequently the sample is wiped dry and connected to the

rotating table using adhesive carbon tape. The load is applied on the indenter by rotating the nut which causes the spring to tighten (see Fig. 4.11). Then the system is inserted into the chamber of the scanning electron microscope and the chamber is depressurised. After approximately one hour the ultra high vacuum is reached and the experiment is executed. After the scratching experiment the chamber is pressurised, the tribo-system taken out of the chamber, the indenter unloaded and lifted and the sample rinsed with acetone. Using an interference microscope the geometry of the wear scar is measured at three locations and the degree of wear determined.

4.3.2 In-situ visual observation of the wear process

The wear experiments provide a range of results. First of all, the electron microscope enables in-situ visual observation of the wear process. This provides information on the dominant wear mechanism and the behaviour of the contact partners. After the experiment the geometry of the resulting scratch is measured using an interference microscope, from which the degree of wear can be obtained. In this section some general results of the in-situ visual observations will be discussed. In the next section both the visual observations as well as the degree of wear results for each of the specimens are presented.

As indicated in the theory for homogeneous materials, with increasing degree of penetration the wear mode changes from ploughing to wedge formation to cutting. This behaviour was verified, as illustrated for the disk covered with a stellite 6 layer in Fig. 4.14. However, two different types of cutting can be distinguished: "flaking", in which small flakes are removed from the surface (see Fig. 4.15(a)) and "chipping" where a continuous chip is cut from the surface (Fig. 4.15(b)). A similar observation was made by Kitsunai [66], in experiments with multiple passings of the asperity. He suggests the flaking or the shear-tongue wear mode to be a special case of ploughing.

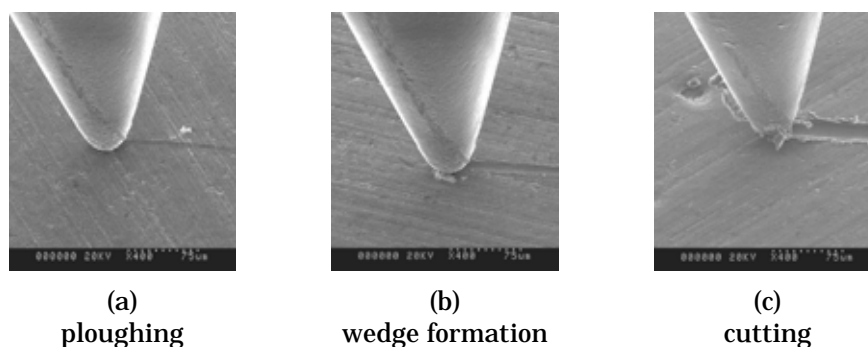
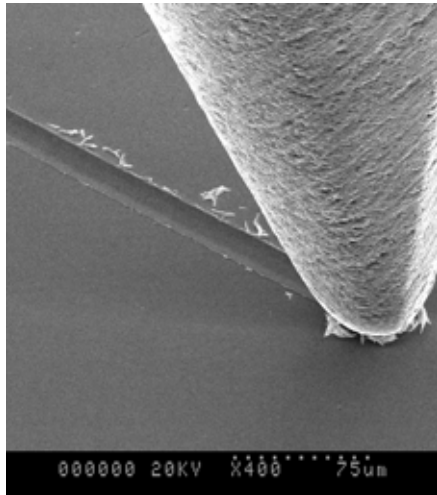
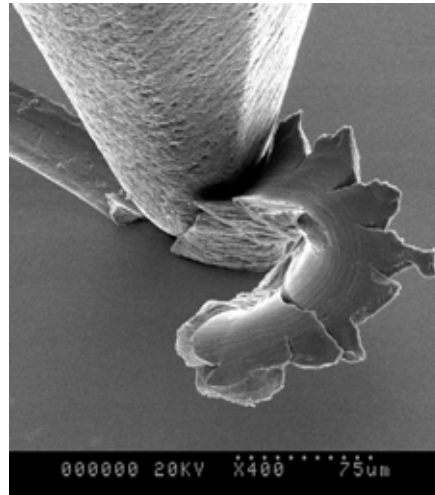


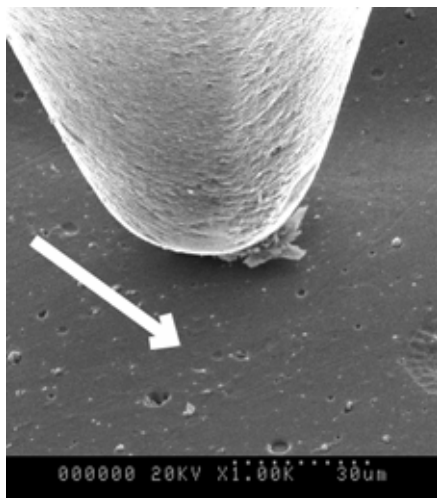
Fig. 4.14: Wear modes observed on the stellite 6 disk.



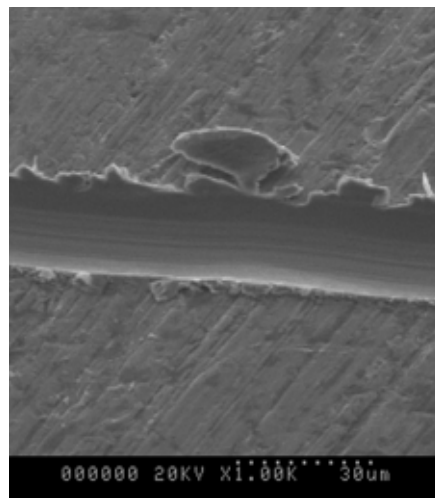
(a)
flaking type cutting



(b)
chipping type cutting



(c)
combined wedge
formation and cutting
on a
chromium nitride
coated surface



(d)
adhesion of a small chip
to the
surface

Fig. 4.15: Visual observations of the SEM wear experiments.

A clear transition from wedge formation to cutting was hardly ever observed. A transitional zone exists in which wedge formation and cutting occur simultaneously. This is illustrated in Fig. 4.15(c) for the specimen with a chromium nitride coating.

Due to the vacuum environment inside the scanning electron microscope no oxidation occurs and therefore the chip formed in front of the diamond indenter in both cutting modes sometimes was not removed as assumed in the model, but adhered to the surface again. An example of this phenomenon is shown in Fig. 4.15(d). It particularly occurred in the flaking regime and cutting with relatively small chips.

4.3.3 Degree of wear results

Based on results presented in literature that were shown in Fig. 4.10, the degree of wear is expected to increase from $D_p = 0$, $\zeta = 0$ to a maximum value ζ_{\max} following an S-shaped curve. The value of this maximum degree of wear varies for each specimen. The degree of wear in the cutting regime can be associated to the brittleness of the material, with a high brittleness resulting in a high degree of wear. For most materials the brittleness is proportional to the hardness. Furthermore, according to Jardret, Zahouani, Loubet and Mathia [55] the shape of the groove created by a given indenter depends on the ratio E / H of the abraded material. When it is assumed that the maximum degree of wear ζ_{\max} depends solely on this ratio, an approximate relation as presented in eq. (4.9) can be obtained by fitting, using the data of Fig. 4.10.

$$\zeta_{\max} = 8.8 \cdot \frac{H}{E} + 0.65 \quad (4.9)$$

In the next section the procedure to determine the degree of wear from the experiments is described.

4.3.3.1 Determination of the experimental degree of wear

The geometry of the scratch and its surrounding area is measured using an interference microscope. A typical result is shown in Fig. 4.16, where both the scratch as well as the carbon nodules are clearly visible. In this image it can be seen that both the groove and the side ridges are not constant in size and hence the value of ζ is not constant over the measured scratch.

It can be concluded that the wear process is not stationary. This is a result of a combination of factors, like the tested material which is inhomogeneous, the stiffness of the experimental set-up and the predominant wear mechanism, such as chip formation or wedge formation with repeated breaking off of wear debris, which are not necessarily stationary.

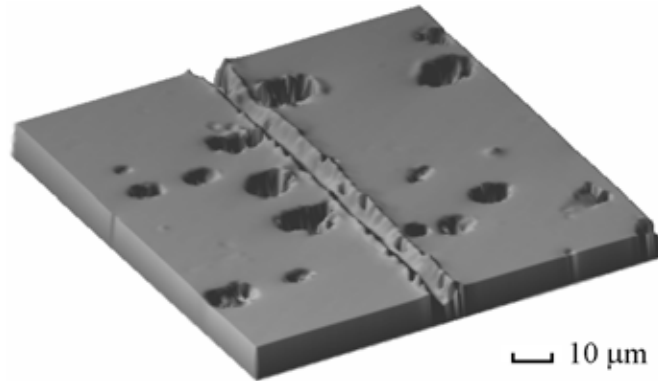


Fig. 4.16: Typical scratched nodular cast iron surface.

From a surface height measurement the visible carbon nodules are neglected and the remaining intact profiles perpendicular to the wear scar are analysed. From each profile the tilt is removed and the location and boundaries of the wear scar are determined. This is done by calculating the deviation from the mean line and defining the wear scar as the location where the surface micro-geometry surpasses three times the standard deviation of the undeformed surface. The result is illustrated in Fig. 4.17(b), showing a scratched surface as well as the boundary of the wear scar. Inside the wear scar, the groove and the side ridges are defined as the locations where the surface data has respectively negative and positive values.

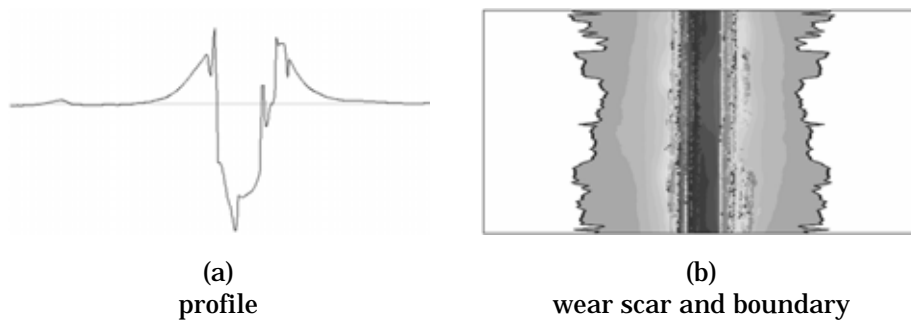


Fig. 4.17: Scratched surface.

For each profile i the degree of wear ξ_i is determined using eq. (4.1). Two typical histograms of values obtained for different profiles in a surface roughness measurement are shown in Fig. 4.18. In the left graph a histogram obtained for a wear scar resulting from an asperity operating in the wedge formation regime is shown. This histogram shows a wide range of values for ξ_i .

Fig. 4.18(b) shows the results for a surface with a wear scar that is cut, with some scatter but predominantly high values for ξ_i . In the analysis of the experimental results, the degree of wear is obtained by averaging over all profiles, according to eq. (4.10). This process is executed for three surface measurements in each experimental scratch.

$$\xi = \frac{1}{n} \cdot \sum_{i=1}^n \frac{A_{g,i} - A_{s,i}}{A_{g,i}} \quad (4.10)$$

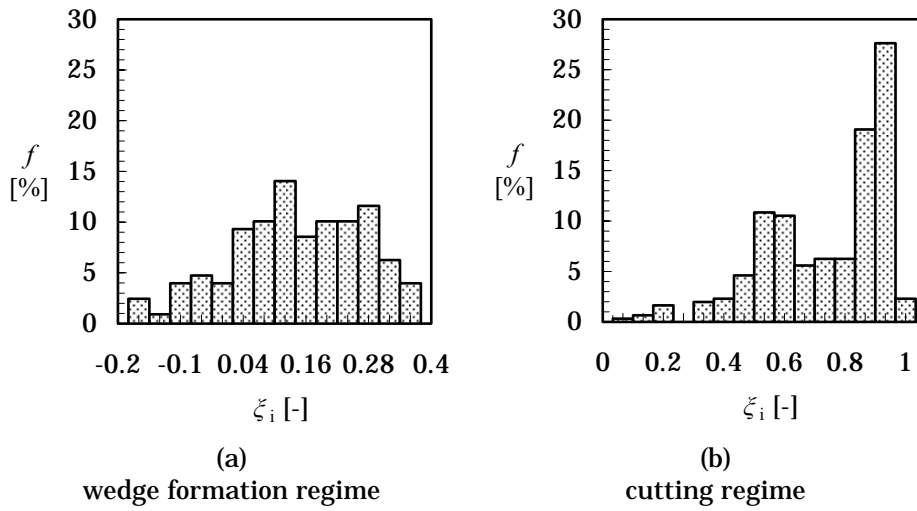


Fig. 4.18: Histograms showing calculated values of ξ_i .

4.3.3.2 Empirical relations for ξ

In Fig. 4.10 it was shown that the degree of wear increases with the degree of penetration following an S-shaped curve. Such a curve can be described using various functions, like a third order polynomial or a hyperbolic tangent. In this work the latter is applied because a *tanh*-function incorporates the asymptotic behaviour of the curve. The template is of the form

$$\xi = A \cdot \tanh(B \cdot D_p - C) + D \quad (4.11)$$

Given the constraining value $\xi = 0$ at $D_p = 0$ and the maximum value ξ_{\max} , the remaining degrees of freedom are obtained using a least squares fitting procedure on the experimental data.

4.3.3.3 Uncoated nodular cast iron

Fig. 4.19 shows the degree of wear as a function of the degree of penetration for the uncoated nodular cast iron specimen. The plotted values are the average of three measurements, with the error bars indicating the standard deviation. The expected increase of ζ with increasing D_p is visible until $D_p = 0.30$. Above this, the degree of wear starts to fluctuate heavily with increasing D_p , while values obtained at the same degree of penetration show a large spread. The underestimation of the value of ζ at these conditions can be explained by the observed adhesion of chips to the surface as mentioned before in Fig. 4.15(b). Therefore, for the uncoated nodular cast iron specimens, the results obtained for $D_p > 0.30$ are neglected in obtaining the least squares fit expression.

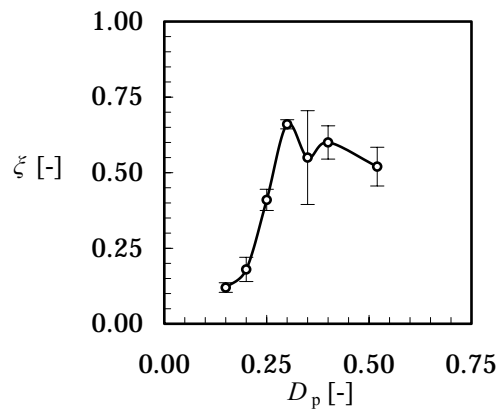


Fig. 4.19: Experimental degree of wear for uncoated nodular cast iron.

In Fig. 4.20 the experimentally obtained results for the uncoated nodular cast iron specimen (solid line with circular points) are compared with results on various heat treated ball bearing steels reported by Hokkirigawa and Kato [50] (dashed lines). From the experimental results a value of $\zeta_{\max} \approx 0.8$ can be estimated. This value is also obtained when the material properties for nodular cast iron are inserted into eq. (4.9), which indicates that the iron matrix of uncoated nodular cast iron behaves in a similar way as ball bearing steel. Applying this maximum and the constraining value $\zeta = 0$ at $D_p = 0$ results in the empiric relation given in eq. (4.12). This relation is shown as the solid line in Fig. 4.20.

$$\zeta = 0.4 \cdot \tanh(12.3 \cdot D_p - 3.0) + 0.4 \quad (4.12)$$

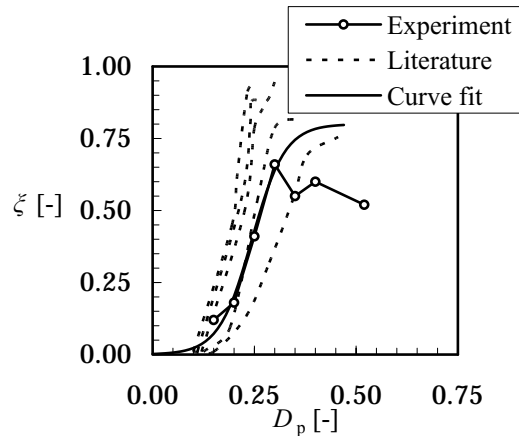


Fig. 4.20: Degree of wear as a function of the degree of penetration for uncoated nodular cast iron.

4.3.3.4 Nodular cast iron with a metal-carbon layer

The metal-carbon layer is applied to the nodular cast iron surface using a PVD process. The applied specimens are coated with a layer of 4 μm thickness.

Even at relatively low loads and small indentation depths, the hard metal-carbon layer fails and circular cracks appear, as shown in Fig. 4.21. The circular crack patterns observed indicate brittle failure to occur on both the leading edge and the trailing edge of the contact.

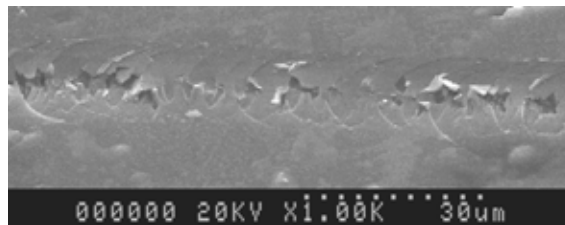


Fig. 4.21: Failure of the Metal-Carbon surface layer.

This behaviour can be attributed to insufficient thickness of the metal-carbon layer, as can be explained by the work of Michler and Blank [77]. They presented the design-map for metal-carbon layers on steel substrates shown in Fig. 4.22. This map is based on both FEM calculations and analytical solutions to simple mechanical analogues. In the map, the x-axis represents the normalised layer thickness (t/R), while the y-axis represents the normalised critical load (N/R^2). Three regions can be observed: at relatively low loads the coated system deforms elastically, for high loads the coating fails

and in between these extremes the substrate deforms plastically, which can result in the egg-shell phenomenon.

In the plot of Fig. 4.22 the dashed area represents the experimental conditions for the metal carbon layer. The normalised layer thickness equals 0.16 while the normalised load varies between 0.3 GPa and 6 GPa, indicating that in these experiments the failure of the surface is caused by this egg-shell phenomenon, where the coating fails due to large plastic deformation of the substrate. This makes the applied metal carbon layer unsuitable as a protective layer on nodular cast iron.

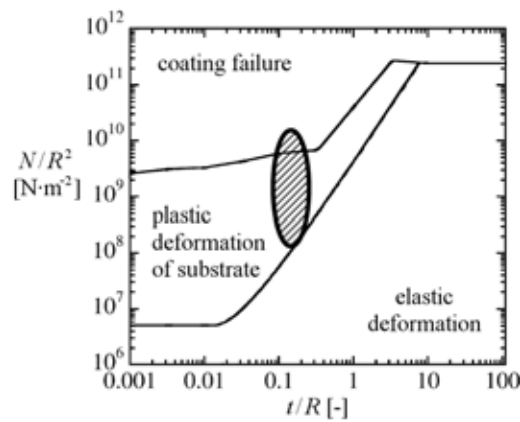


Fig. 4.22: Coating failure map according to Michler and Blank [77].

4.3.3.5 Nodular cast iron with a chromium nitride layer

In the photographs of the scratching process in Fig. 4.23 a clear wear groove with hardly any shoulders can be seen at each of the penetration depths. However, no chips or other volumetric wear is observed in the scratching process, except some at situations when the indenter encounters a carbon

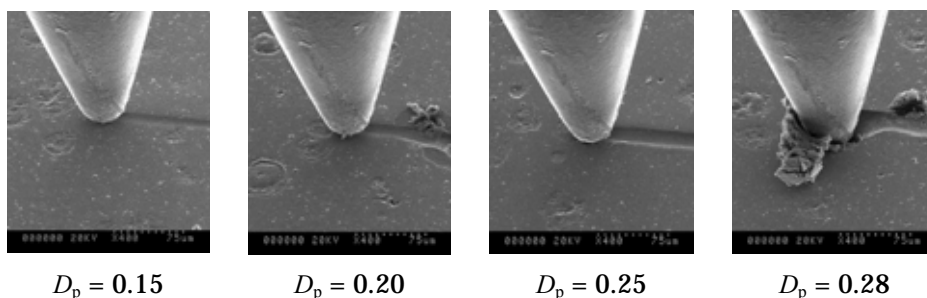


Fig. 4.23: Wear scars on chromium nitride coated nodular cast iron.

nodule as shown in the photographs at $D_p = 0.20$ and 0.28 . The image at $D_p = 0.28$ shows the indenter subsided into such a carbon nodule. In the determination of the degree of wear this sinking in of the indenter is neglected as it does not occur to this extent in the contact between two rough surfaces. In the contact between rough surfaces the indentation depth of individual asperities is generally displacement driven, while the experiments on single asperity indentation are force driven. Higher values of the degree of penetration could not be tested as the subsiding of the indenter into the carbon nodules resulted in fracture of the indenter.

Fig. 4.24 shows the degree of wear as a function of the degree of penetration for the chromium nitride coated specimens. The figure confirms the visual observations that a wear groove without shoulders is formed. The degree of wear remains approximately constant and at a high value of about $\zeta = 0.6$.

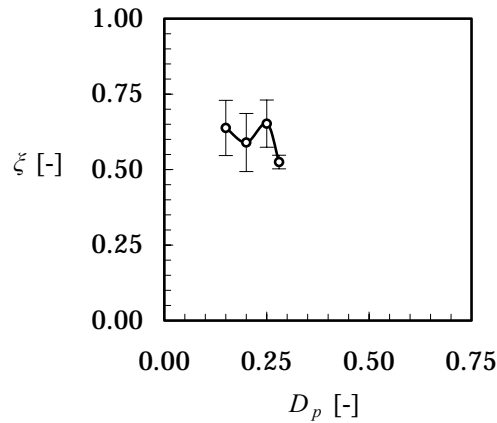


Fig. 4.24: Degree of wear as a function of the degree of penetration for chromium nitride coated nodular cast iron.

Although the degree of wear is quite high, no wear debris is observed during the scratching experiments. This might be caused by the Young's modulus of the CrN top-layer, which is significantly higher than that of the substrate. According to Bhushan [7] and O'Sullivan and King [84] the situation of a stiff layer on a more compliant substrate results in very high values of the sub-surface stresses. Therefore the substrate will deform plastically while the stiff top-layer prevents the formation of side ridges, causing an apparently high value of ζ , even though there is no volumetric wear.

4.3.3.6 Nodular cast iron with a stellite 6 layer

Using the laser-cladding technique a relatively thick surface layer is applied to the surface. A typical layer thickness ranges from several tenths of a millimetre to more than 1 mm. Because the indentation depths are of the order of micrometers, the contact behaviour depends only on the clad layer and not on the substrate material and the effective hardness of the coated surface is simply the hardness of the layer.

Fig. 4.25 shows the contact at several indentation depths. In these photographs the transition from ploughing to flaking to cutting can be observed. Particularly at a high degree of penetration ($D_p > 0.30$) the cutting process is fierce, see for instance the enlarged photograph at $D_p = 0.35$, where chips are clearly visible.

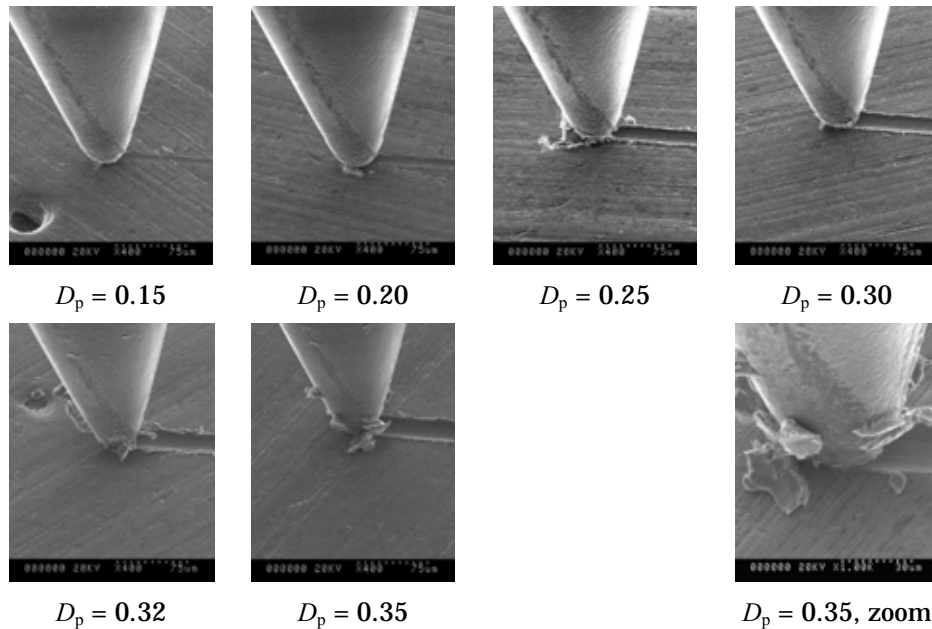


Fig. 4.25: Wear scars on stellite 6 coated nodular cast iron.

The experimentally determined degree of wear are plotted in Fig. 4.26. An estimate of the maximum degree of wear ζ_{\max} is calculated by inserting the hardness of the stellite layer as listed in Table 4.3 into eq. (4.9), which gives $\zeta_{\max} = 1$. Assuming again a *tanh*-fitting template and inserting $\zeta(D_p = 0) = 0$ results in the fit of eq. (4.13) as shown as the solid line in Fig. 4.26. This fit has a correlation coefficient of $R^2 = 0.98$.

$$\xi = 0.5 \cdot \tanh(8.6 \cdot D_p - 2.3) + 0.5 \quad (4.13)$$

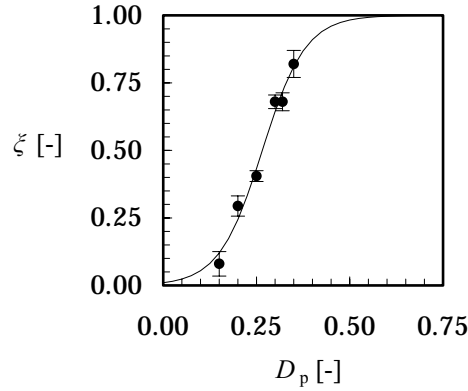


Fig. 4.26: Degree of wear as a function of the degree of penetration for stellite 6 coated nodular cast iron.

4.3.3.7 Nodular cast iron with a duplex layer

With this duplex layer system the relatively thick stellite 6 layer that is clad on the nodular cast iron specimen is coated with a thin chromium nitride layer. The result is a very hard coated surface with a thick hard undercoat.

Photographs of the wear process at various values of D_p are shown in Fig. 4.27. Similar to the observations for the CrN monolayer, no shoulders are observed along the groove. Furthermore, no chips or wear debris is observed in the scratching process. The deep crack in front of the indenter at $D_p = 0.28$ is caused by the cladding process, and obviously the test was stopped before the indenter entered the crack. For values of $D_p > 0.28$ the high applied contact load caused brittle fracture of the indenter after only a short time of testing. Therefore no pictures of the scratching indenter are available. Furthermore, photographs of the wear scars at $D_p = 0.28$ and $D_p = 0.34$ indicate coating failure to occur at $D_p = 0.34$.

The system hardness as measured using a 100 gr Vickers hardness tester for this duplex layer of stellite 6 and chromium nitride is the highest of all tested specimens. Therefore, again a value $\xi_{\max} = 1$ is taken in the curve fit. The result of the curve-fit is the expression shown in eq. (4.14), which is shown as the solid line in Fig. 4.28.

$$\xi = 0.56 \cdot \tanh(6.2 \cdot D_p - 1.1) + 0.44 \quad (4.14)$$

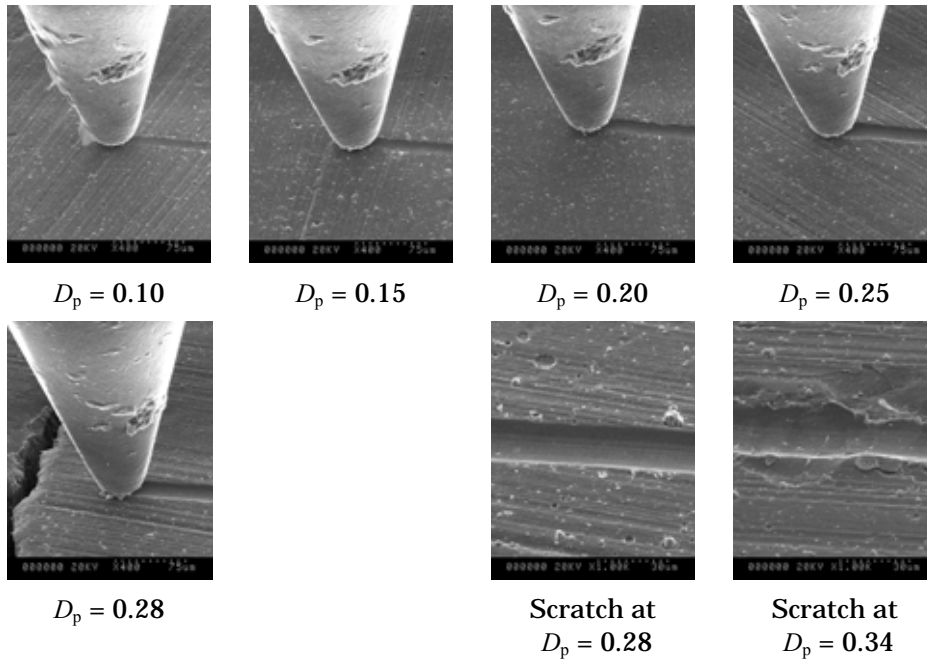


Fig. 4.27: Wear scars on stellite 6 - chromium nitride duplex coated nodular cast iron.

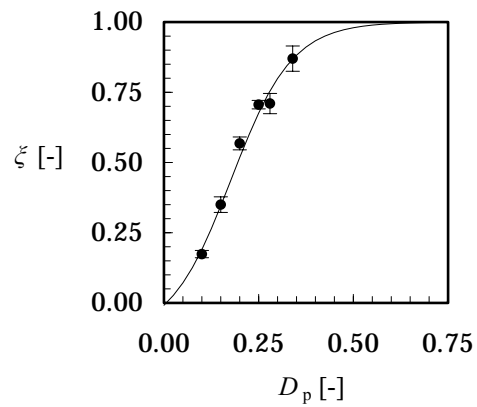


Fig. 4.28: Degree of wear as a function of degree of penetration for stellite 6 + chromium nitride duplex coated nodular cast iron.

4.4 Implementation

The expressions for the degree of wear as a function of the degree of penetration can be combined with the contact model as developed in Chapter 3, resulting in an empirical model for the abrasive action of a sliding rigid indenter in contact with a deforming counter surface. In this paragraph some results of the model are presented. Unless stated otherwise in the figures, the parameters as listed in Table 4.4 are applied for the calculations.

Table 4.4: Reference parameters for the presented results

Material combination	diamond indenter - uncoated nodular cast iron	
Indenter reduced radius	R_*	50 μm
Normal load	N	5 N
Ellipticity of asperity	λ	0.5
Orientation of asperity	β	30°

In this implementation a spherical indenter with a radius of 100 μm is applied, in contrast to the 25 μm radius of the indenters used in the SEM-tribo-system experiments described in the previous section. Furthermore it should be noted that the situation $\lambda = \lambda_s$, $\beta = \beta_s$, is identical to $\lambda = 1/\lambda_s$, $\theta = 90^\circ - \beta_s$. In which λ is the aspect ratio or ellipticity of the asperity and β represents the orientation of the asperity with respect to its sliding direction as illustrated in Fig. 4.9.

Fig. 4.29 shows the wear volume per unit length Ψ against the ellipticity ratio of the indenter for several orientations and at a constant carried load.

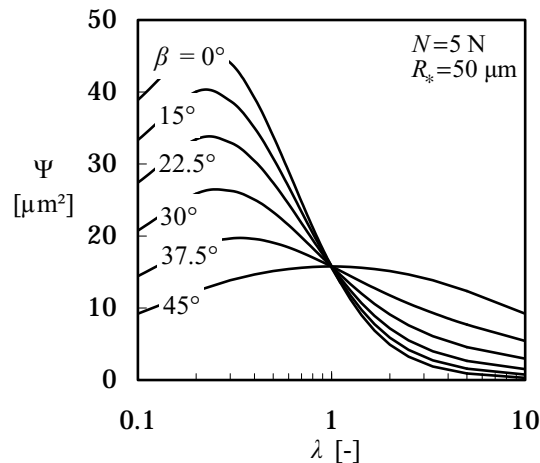


Fig. 4.29: Wear per unit length as a function of the ellipticity ratio for various indenter orientations.

Obviously, for a circular contact ($\lambda = 1$) the orientation has no influence on the wear behaviour. For both more wide and more narrow contacts the figure shows clearly that the effect of the orientation of the asperity is significant. This is also shown in Fig. 4.30 where Ψ is plotted against the orientation of the indenter for indenters with various ellipticities.

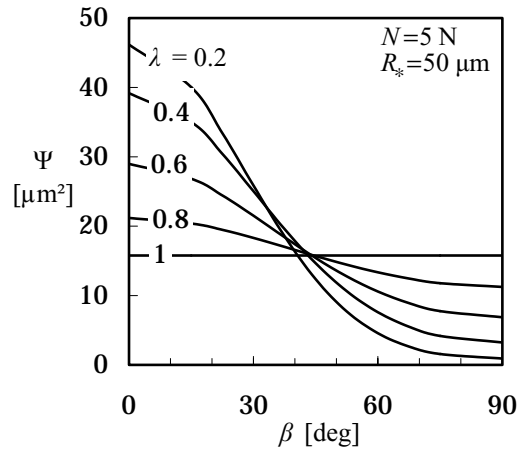


Fig. 4.30: Wear per unit length as a function of the indenter orientation for various indenter ellipticity ratios.

Fig. 4.31 shows the relation between the volumetric wear per unit length caused by the indenter and the carried load for various orientations of the indenter. The reduced radius of the indenter is $R_* = 50 \mu\text{m}$ with an ellipticity ratio of $\lambda = 0.5$. It can be seen that the load has a large influence on the

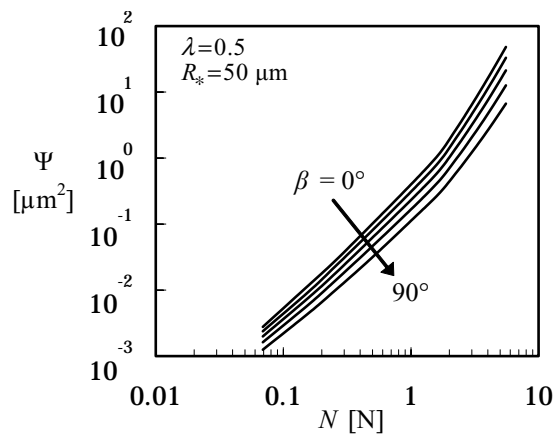


Fig. 4.31: Wear per unit length as a function of the carried load for various indenter orientations.

resulting wear: the slope in the $\log(\Psi) - \log(N)$ plot is larger than two. In the plot the elastoplastic to plastic transition at $N = 1.7$ N is clearly visible as a change in slope of the plotted lines. The plot confirms the considerable influence of the sliding direction of the indenter that was seen in the previous figures: at constant load the wear might change almost tenfold only by changing the orientation of the indenter.

The plots in Fig. 4.32 show the wear per unit length as a function of the load caused by various indenters with a different ellipticity ratio at a constant orientation. Particularly at relatively high loads the influence of the orientation of the indenter on the wear volume is large. The transition from elastic-plastic to fully plastic deformation ranges from $N = 2.3$ N for $\lambda = 0.2$ and $\lambda = 5$ to $N = 1.6$ N for $\lambda = 1$ and again results in a change in the slope of the graph.

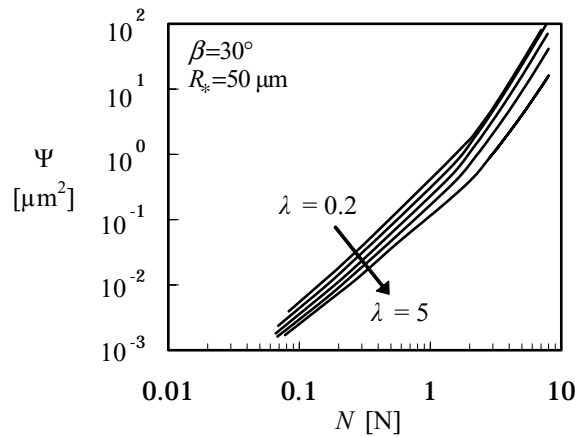


Fig. 4.32: Wear per unit length as a function of the load for various indenters with changing ellipticity ratio.

Fig. 4.33 shows the wear per unit length against the contact load for various indenter sizes. As expected, the size has a large influence on the wear behaviour: at a certain constant load, a small indenter operates in the plastic regime, with $d \sim N \cdot R^{-1}$, while a large indenter operates in the elastic regime ($d \sim N^{0.66} \cdot R^{-0.33}$). So, for the small indenter both the indentation depth and the degree of penetration (and hence the value of ξ) are larger than for the large indenter, resulting in a strong dependency of the volumetric wear on the indenter size.

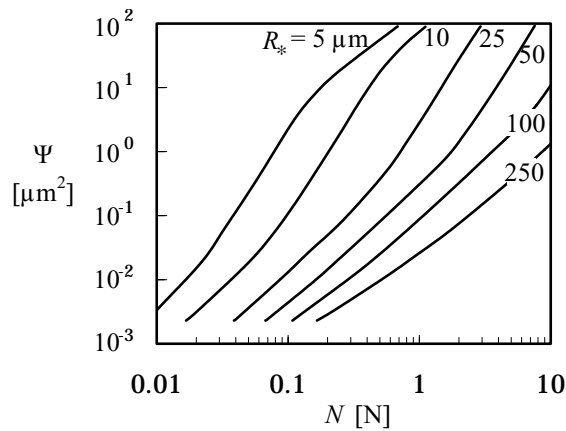


Fig. 4.33: Wear per unit length as a function of the load for various indenters with changing reduced radius.

Fig. 4.34 shows the wear per unit length as a function of the load for three different abraded materials. For very low loads and hence very small indentation depths, the lowest wear rate is found for the uncoated nodular cast iron surface. The laser clad surface and the CrN coated laser clad surface show a higher wear. At higher loads the reverse can be observed, with the highest volumetric wear for nodular cast iron. At a given load the abrasive asperity penetrates deeper into the uncoated nodular cast iron. However, the degree of wear at low indentation depths for nodular cast iron is very low. Because the volumetric wear is the product of the degree of wear and the frontal area of the asperity, a very low value of ξ , results in a very low wear volume, even when the indentation depth and hence the frontal area is

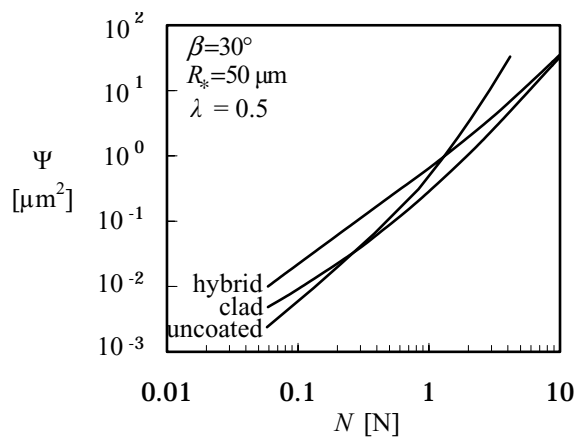


Fig. 4.34: Wear per unit length as a function of the load for various indenters with changing reduced radius.

substantial. At higher indentation depths the degree of wear of nodular cast iron also increases and its positive effect on the volumetric wear in comparison to both the laser clad as the CrN and laser clad surfaces is cancelled.

4.5 Discussion

In this chapter an empirical model for the scratching wear between a single sliding indenter or asperity and a deforming layered flat body is derived. Under relatively mild scratching conditions the material that originated in the scratch is transferred to the sides of the scratch, forming ridges. Although a scratch is formed, the volumetric wear in such a ploughing process equals zero. In the most severe scratching condition the material from the scratch is removed by a chipping or a cutting process, causing significant volumetric loss. In between these two extremes a non-steady state process might occur in which a lump of scratched material builds up in front of the sliding indenter. After reaching a critical size the lump breaks off, resetting the process to its initial conditions. In single asperity scratching experiments no distinct transitions between these three wear regimes were found, but a gradual transition from one to another. The degree of wear caused by the scratching action of a single asperity is plotted as a function of the degree of penetration.

The application of a hard coating on one of the bodies can provide improved wear behaviour of the tribological system. When the indentation depth is small compared to the layer thickness, the contact and wear behaviour is dominated by the hard top layer. For larger indentation depths the material behaviour depends on the combination of substrate and layer. In this case, a substantial difference in material properties of the top layer and the substrate might result in decreased wear resistance of the body. Typical failure mechanisms are cracking, flaking and delamination, see for instance the experimental observations for the metal-carbon layer in this chapter. A possible solution is to provide a more rigid support below the thin hard layer, for instance by increasing the layer thickness or the application of a hard underlayer.

The results obtained with the single asperity wear model indicate that the volumetric wear is very sensitive to the radius of the scratching asperity, the ellipticity ratio and the applied load. Furthermore, the application of hard surface layers might not always be beneficial.

Chapter 5

Modelling Contact and Abrasive Wear of Real Surfaces

5.1 Introduction

Engineering surfaces are never perfectly smooth. At a high magnification every surface shows irregularities which are for instance caused by the manufacturing process. In the contact between two surfaces, the highest irregularities on the surfaces are most probably the first ones to touch the counter surface. These micro-contact spots, i.e. the areas where real contact occurs, cover only a fraction of the apparent contact area.

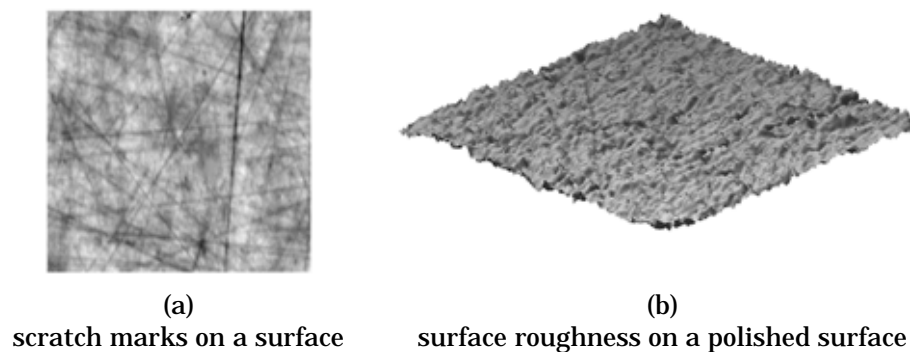


Fig. 5.1: Example of a surface roughness measurement.

This chapter focuses on the abrasive wear behaviour of real or engineering surfaces in contact. The model for abrasive wear in a single asperity contact, as developed in the previous chapters, is extended to describe the abrasive wear of rough surfaces in contact.

There are several ways to describe the behaviour of rough surfaces in contact. Usually some kind of simplification of the surface topography is used to enable the application of relatively simple equations. In this way, instead of full numerical simulations, analytical or semi-analytical models can be constructed.

5.2 Contact of rough surfaces

The most commonly applied contact model is the so-called "Greenwood and Williamson model". This model follows a statistical approach and is named after the authors of the renowned paper [40] in which the idea of simplifying surface roughness by assuming that it is composed of a collection of hemispherical shaped asperities with radius R , asperity density n and a statistical height distribution $\varphi(s)$ was introduced. The rationale behind this model and its assumptions is that they enable the application of relatively straightforward equations in modelling the contact behaviour. For example, the representation by spheres enables application of the theory of Hertz [47] to describe the elastic contact between two rough surfaces.

The Greenwood-Williamson model is discussed in more detail in Appendix B.3. Some extensions and adaptations of the GW-model to include plastic deformation and elliptical contacts are described by Chang, Etsion and Bogy [23], de Rooij [26], Francis [37], Halling [42], Horng [51], Johnson [58], Ogilvy [83] and Pullen and Williamson [87].



Fig. 5.2: Simplified surface roughness for the Greenwood & Williamson model.

In this statistic model the micro-contacts are assumed to be the summits on the rough surface that are identified using a nine-point criterion as described in Appendix B.3, according to Greenwood [39] and de Rooij [26]. Subsequently, de Rooij calculates the radius of each summit using three-point finite differences and takes the average value. This procedure has a number of disadvantages: first of all, a typical micro-contact in the sliding contact between rough surfaces is generally larger than one single summit, particularly in forming operations. Secondly, the average summit radius is calculated taking into account all summits, of which only a fraction is really in contact with the counter surface. Thirdly, the determination of the required

parameters from a given surface height measurement is not straightforward [26] and might require pre-processing of the data.

The statistical approach as briefly discussed above can give satisfactory results in modelling contact phenomena, see for instance the work of McCool [75], and Handzel-Powierza et al. [46]. However, in the wear model for single asperities, as discussed in Chapter 4, the relation between the summit radius and the volumetric wear is highly non-linear, indicating that the radius of each summit should be calculated with high accuracy and that taking the average summit radius in wear modelling leads to substantial errors, even in situations when the radii are determined accurately.

5.3 Deterministic approach

These drawbacks can be overcome with the application of a deterministic approach. From the measured surface height data of both contact partners as well as the contact conditions, the separation between the two surfaces can be calculated. This is done using an iterative procedure, as illustrated in Fig. 5.3. For explaining purposes this iterative procedure will be illustrated for the contact between a rough and a perfectly smooth surface in the following section. However, the procedure applies also to contacts between two rough surfaces.

Given the material properties of the two surfaces in contact, the surface micro-geometry and a known contact load, an initial separation between the two surfaces is estimated. At this separation between the surfaces a number of local contact spots is formed. In these so-called micro-contacts the actual surface to surface contact occurs. The geometry of each micro-contact is approximated using a simple geometrical body, called asperity. The contact load carried by an individual asperity follows from its geometry and the indentation depth. Summation of the contact load over all micro-contacts gives the total load carried by the contact, which is compared with the input load. Based on this outcome the surface separation is altered and the procedure is repeated, until the input load and the carried load match. Below the subsequent steps of the procedure are explained in some more detail.

5.3.1 Micro-contact

In the contact between a hard rough and a softer smooth surface, at a given mean plane separation, the micro-contacts are approximated by applying a threshold at a certain level, as illustrated in Fig. 5.4(a). In this contact between the (lower) rough surface and the (upper) smooth and flat surface, the grey area represents two micro-contacts in the contact. Fig. 5.4(b) shows a typical surface height representation, measured using an optical interference

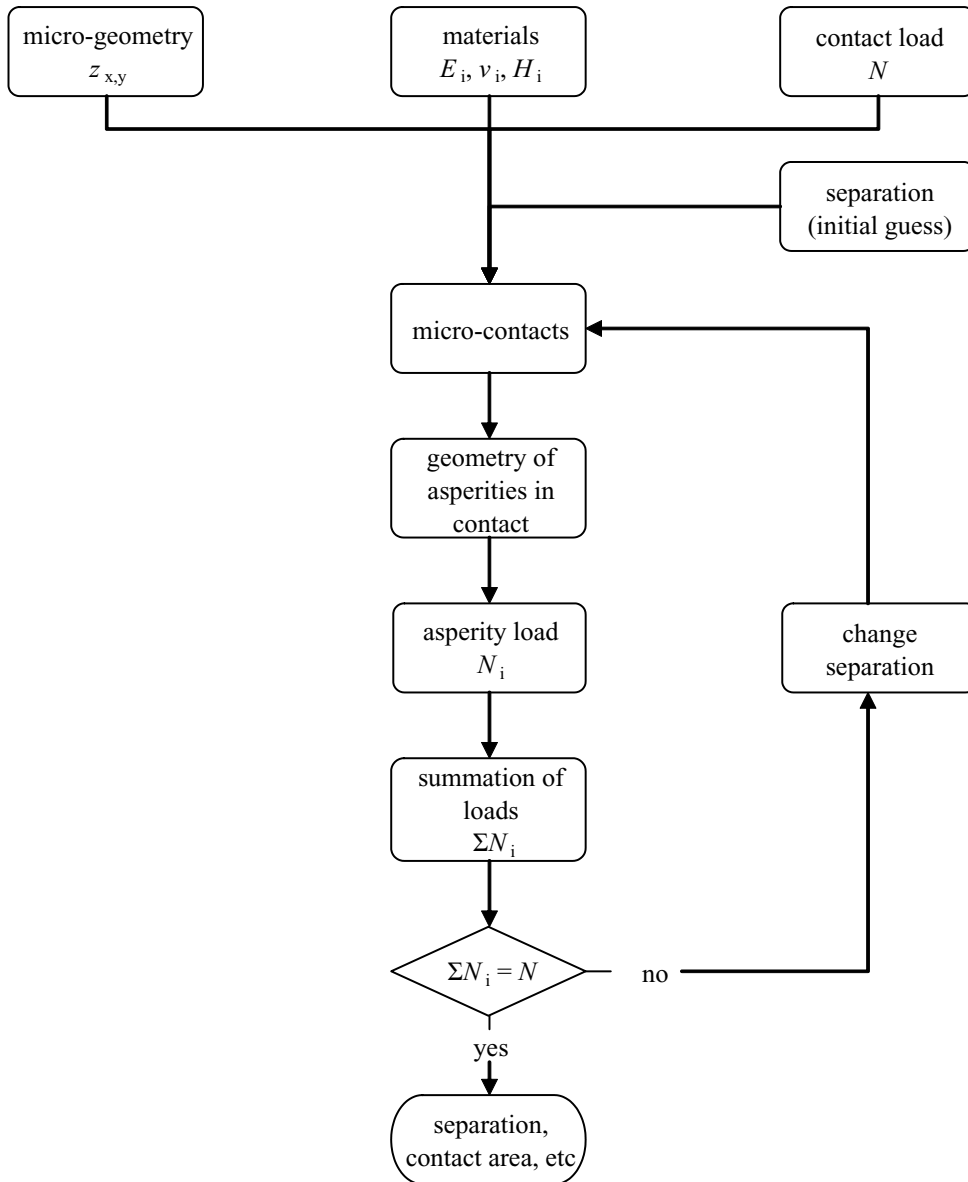


Fig. 5.3: Flow diagram of the iterative procedure applied in modelling the contact between rough surfaces.

microscope, as described by de Rooij [26]. A dark colour marks the valleys and the white regions are tops or the highest points on the surface. For the contact between this surface and a flat the resulting micro-contacts at a given mean plane separation are shown in black in Fig. 5.4(c).

When both surfaces are rough, the micro-contacts are obtained in a similar fashion, provided that the cut-off level is not a flat anymore. Instead, the tribological contact is composed by placing the two surfaces on top of each other at a given mean plane separation, with the micro-contacts defined as the locations where the micro-geometry of the 'bottom surface' has a higher value than that of the 'top-surface'.

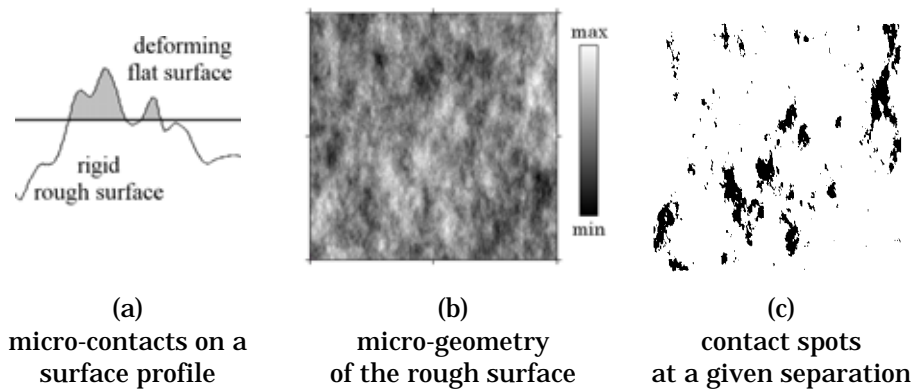


Fig. 5.4: Contact between a rough surface and a smooth and flat surface.

5.3.2 From micro-contact to asperity

The surface micro-geometry inside a micro-contact can be extracted from the measured height data. Subsequently, a simple geometrical shape can be fitted through the data, which enables the use of the equations developed in Chapters 3 and 4 for the contact and wear behaviour of the micro-contact. In the following, this simplified geometrical representation of a micro-contact is called an asperity.

As discussed in the previous chapter both the shape and the size of the representative asperity have a large effect on the contact and wear behaviour. These parameters can be obtained in various ways. In a previous work by Masen and de Rooij [72] a paraboloidal shape was fitted through the measured surface height data of each contact spot using least squares fitting. From this fit, two radii R_x and R_y and the orientation β of the asperity are obtained. De Pellegrin and Stachowiak [25] define the sharpness of an asperity, i.e. the ratio of normal area and frontal area, as the criterion to fit the asperities, which are mathematically described by a power-law. Some

other shapes and types of asperities that are reported in literature include spherically tipped cones (see Jiang, Sheng and Ren [56] and Jacobsen, Wallen and Hogmark [53]) and hyperboloids (Torrance [102]). In this work both elliptic cones and elliptic paraboloids are used as asperities. The applied method to fit an asperity to a micro-contact is discussed in the following section.

5.3.2.1 Load and energy defining the equivalent asperity

The hardness of a material is generally measured by indenting a supposedly rigid body at a pre-defined load into the material. Depending on the shape of the indenting body a characteristic size of the remaining indentation is measured, giving the indentation area A . The hardness H is then calculated by dividing the contact load N by the area A :

$$H = \frac{N}{A} \quad (5.1)$$

In representing the surface micro-geometry by a collection of asperities, from eq. (5.1) it can be concluded that the so-called "load equivalent asperity" should have the same normal area A as the original micro-contact spot in order not to alter the separation in fully plastic contact conditions.

Stillwell and Tabor [96] used an alternative but equivalent definition for the hardness H :

$$H = \frac{W}{V} \quad (5.2)$$

in which W represents the plastic work of indentation and V the deforming volume. According to eq. (5.2) the work associated with the (plastic) deformation of a material is proportional to its hardness and the deformation volume. This deformation volume represents the plastic region surrounding the indentation. When it is assumed that, irrespective of the shape of the indenting body, the deformation volume is proportional to the indentation volume, the energy equivalent representative asperity should have the same volume as the micro-contact.

Summarising, in order to maintain load and energy equivalence, the representing asperity should have the same contact area A and indentation volume V as the micro-contact. In this way both the load balance and the energy balance in fully plastic deformation are maintained by the substitution

of the actual geometry of the micro-contact by an equivalent shape. The two shapes of asperities that are considered in this work are discussed below.

5.3.2.2 Elliptic cone

The vertical cross-section of an elliptic cone through its centre is a triangle, while its horizontal cross-section is an ellipse. As shown in Fig. 3.2(a), the shape of an elliptic cone is characterised by its attack angles in x- and y-direction φ_x and φ_y . For a micro-contact with known volume V_m , contact area A_m and ellipticity ratio λ_m , the attack angles of the representing ellipsoidal cone are determined using eq. (5.3) and eq. (5.4).

$$\varphi_x = \text{atan} \left(\frac{3 \cdot V_m}{A_m} \cdot \sqrt{\frac{\pi \cdot \lambda_m}{A_m}} \right) \quad (5.3)$$

$$\varphi_y = \text{atan} \left(\frac{3 \cdot V_m}{A_m} \cdot \sqrt{\frac{\pi}{\lambda_m \cdot A_m}} \right) \quad (5.4)$$

5.3.2.3 Elliptic paraboloid

An elliptic paraboloid, as shown in Fig. 3.2(b), has a parabola as the vertical centre-line cross-section while the horizontal cross-section is an ellipse. The equivalent paraboloid is defined by the radii in x- and y-directions, R_x and R_y . These are obtained from eq. (5.5) and eq. (5.6), in which again V_m represents the volume, A_m the contact area and λ_m the ellipticity ratio of the asperity.

$$R_x = \frac{A_m^2}{4 \cdot \pi \cdot V_m \cdot \lambda_m} \quad (5.5)$$

$$R_y = R_x \cdot \lambda_m^2 \quad (5.6)$$

5.3.2.4 Interaction between asperities

Depending on the shape of the asperity and the regime in which it operates, the micro-level contact model as derived in Chapter 3 provides the load carried by the asperity. Simply summing the contributions of all individual micro-contacts gives the load carried by the macro-level contact. Repeating this procedure for a sequence of load increments, i.e. simulating that one surface subsides into the other, a force-displacement relation for the rough surface is obtained.

Merging of several adjacent asperities into a single micro-contact with increasing load, as illustrated in Fig. 5.5, is automatically taken into account

because the contact spot fitting procedure is repeated for each load increment and only surface height data that lies within the micro-contact is taken into account.

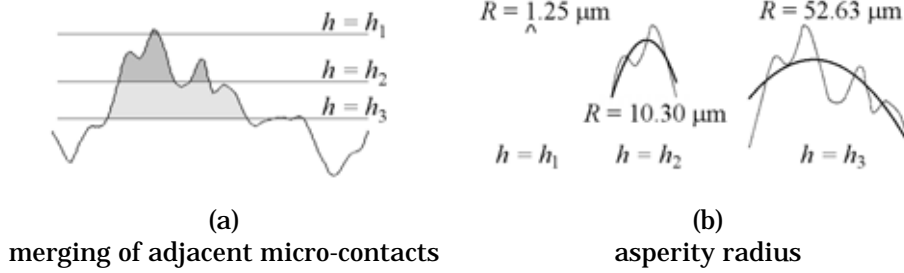


Fig. 5.5: Micro-contacts and asperities at three values of the surface separation.

Only the contact data coloured dark in Fig. 5.5(a) is used as input for the asperity fitting function, resulting in a changing contact radius and the formation of a merged contact spot, as illustrated in Fig. 5.5(b). This two-dimensional example clearly shows that the radius of the fitted asperity can change considerably with changing approach of the two surfaces.

5.3.2.5 Wear

Once the geometry of all individual asperities and the associated behaviour of the surfaces in contact are determined using the contact model, the volumetric wear V_i caused by the sliding action of a single asperity is obtained using eq. (5.7), which is similar to eq. (4.4), with A_{fi} the indenting part of the frontal area of the asperity, ζ_i the degree of wear and L the sliding distance.

$$V_i = \zeta_i \cdot A_{fi} \cdot L \quad (5.7)$$

Because a rough surface is represented as a collection of independently operating asperities, the total wear volume can be calculated according to eq. (5.8), i.e. taking the summation of the contributions of all individual micro-contacts. Subsequently, the volumetric wear per unit sliding distance Ψ is calculated according to eq. (5.9).

$$V = \sum_{i=1}^c V_i \quad (5.8)$$

$$\Psi = \frac{V}{L} \quad (5.9)$$

5.4 Results of the deterministic model

In the following sections the deterministic contact and wear model is applied to three tribological systems and the results will be presented and discussed. The three sample surfaces shown in Fig. 5.6 act as hard abrasive surfaces, while in each system the abraded counter surface is supposed to be perfectly smooth and flat.

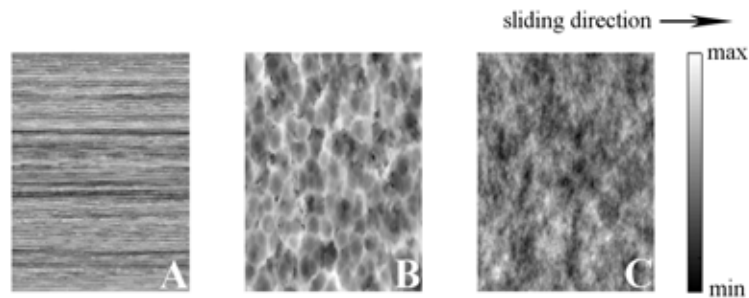


Fig. 5.6: Surface micro-geometry of the three applied sample surfaces.

Surface A is a ground and subsequently polished surface, characterised by a principal direction of the surface micro-geometry. Surface B is a surface resulting from a sand blasting process, resulting in an isotropic surface micro-geometry with a relatively high roughness. The micro-geometry of surface C is isotropic and is numerically generated, with statistical parameters similar to those of surface A. The micro-geometry of the surfaces A and B is measured using an optical interference microscope. Each surface representation covers an area of 228×304 points with a pixel size in x- and y-direction of $1.45 \mu\text{m}$ respectively $1.49 \mu\text{m}$, i.e. each measured surface area equals 0.149 mm^2 .

5.4.1 Asperity properties

Some surface roughness parameters of the surfaces are presented in Table 5.1. Furthermore, the table shows statistical parameters of the summits as determined according to de Rooij [26]. R_q represents the standard deviation of the surface roughness, n is the summit density, C is the number of summits on the surface measurement, R_{avg} is the average summit radius as calculated using finite differences, σ is the standard deviation of the summit heights and $C_{\text{st}}(h)$ represents the number of summits above the cut-off height h . These statistical parameters are explained in more detail in Appendix B.3.

From the summit density n , the number of micro-contacts C_{st} at a given approach can be calculated, assuming A_n equals the measured surface area. The so-called GW-parameters, i.e. the parameters of the surface that are applied as input in the statistical model, are determined according to the equations presented in Appendix B.3, after de Rooij [26].

Table 5.1: Statistic properties of the three sample surfaces.

	surface A	surface B	surface C
	anisotropic	isotropic	isotropic
R_q [μm]	0.16	1.97	0.16
n [m^{-2}]	$2.3 \cdot 10^{10}$	$3.6 \cdot 10^9$	$2.0 \cdot 10^{10}$
C [-]	3424	541	3004
R_{avg} [m]	$1.1 \cdot 10^{-5}$	$3.7 \cdot 10^{-6}$	$2.0 \cdot 10^{-5}$
σ [m]	$1.2 \cdot 10^{-7}$	$1.9 \cdot 10^{-6}$	$1.5 \cdot 10^{-7}$
$n \cdot R_{\text{avg}} \cdot \sigma$ [-]	0.03	0.025	0.06
$C_{\text{st}} (h/R_q = 0)$	1712	270	1502
$C_{\text{st}} (h/R_q = 1)$	322	81	438
$C_{\text{st}} (h/R_q = 2)$	14	10	52

In Fig. 5.7 the number of micro-contacts is plotted as a function of the normalised mean plane separation of the two surfaces. The separation is normalised with respect to the roughness R_q of the surface. Fig. 5.7(a) shows the number of micro-contacts obtained with the statistic model C_{st} , while Fig. 5.7(b) presents the number of contact spots according to the deterministic approach C_{det} .

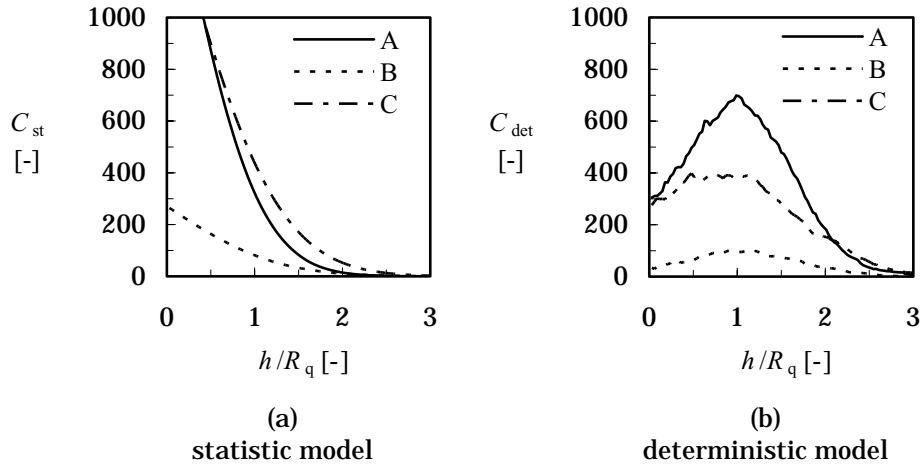


Fig. 5.7: Number of micro-contact spots as a function of the normalised separation between the surfaces.

According to the statistical model, the number of micro-contacts increases with decreasing separation h between the contact partners. For the deterministic approach a similar trend is observed only when the separation is relatively large. In that case there are relatively few contacting spots, which are scattered over the surface. Because the individual micro-contact spots are quite isolated, a decrease in separation will result in the formation of more micro-contacts while merging of neighbouring contact spots will hardly ever occur. At smaller separations the distance between the micro-contacts is smaller, and therefore merging of neighbouring micro-contacts will occur more often. As a result the growth of the number of contact spots with decreasing separation slows down. For the three surfaces calculated, the number of micro-contacts even decreases with decreasing separation when the normalised separation h/R_q is smaller than approximately 1.

5.4.1.1 Deterministic model with conical shaped asperities

The histograms in Fig. 5.8 show the distribution of the attack angles φ_i of the asperities for surface A as calculated using the deterministic approach with cone fitting. The y-axis represents the percentage f of the total number of asperities corresponding to the value of the attack angles as shown on the x-axis. Fig. 5.8(a) represents the situation when the normalised mean plane separation h/R_q of the contacting surfaces is 1.0, Fig. 5.8(b) shows the histogram for $h/R_q = 1.5$ and Fig. 5.8(c) corresponds to $h/R_q = 2.0$. The attack angles of the asperities range between 0 and 15 degrees and the distribution of asperity angles appears to be rather insensitive to the separation. The observation that the distribution of the asperity angles is indifferent to the mean plane separation agrees with the work of Greenwood [39] for summits described according to the random process theory.

Fig. 5.9 shows the histograms of the calculated asperity attack angles for the rough isotropic surface B at three values of the normalised mean plane separation. Some very sharp asperities are found, with attack angles over 60 degrees, but the majority of the asperities has an attack angle smaller than 20 degrees. The histograms of the asperity attack angles for surface C are presented in Fig. 5.10, again at three values of the normalised mean plane separation. In this case the resulting asperities are quite shallow, with attack angles smaller than 5°.

It can be concluded that the distribution of asperity attack angles is quite insensitive to the mean plane separation between the two surfaces. Furthermore, for each of the three surfaces the calculated attack angles of the asperities rarely exceed 20°. According to the abrasive wear mode map for wedge shaped asperities presented by Hokkirigawa and Kato [49], based on the theoretical slip-line models of Challen and Oxley [17], in practical applications abrasive wear does not occur for attack angles smaller than 20°.

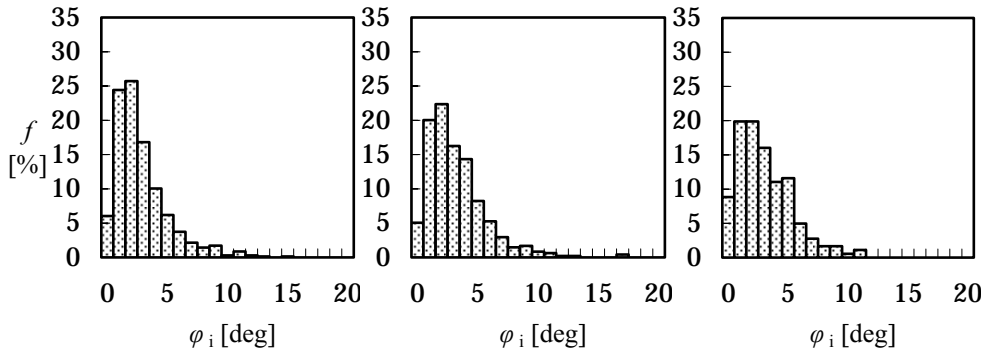


Fig. 5.8: Surface A.

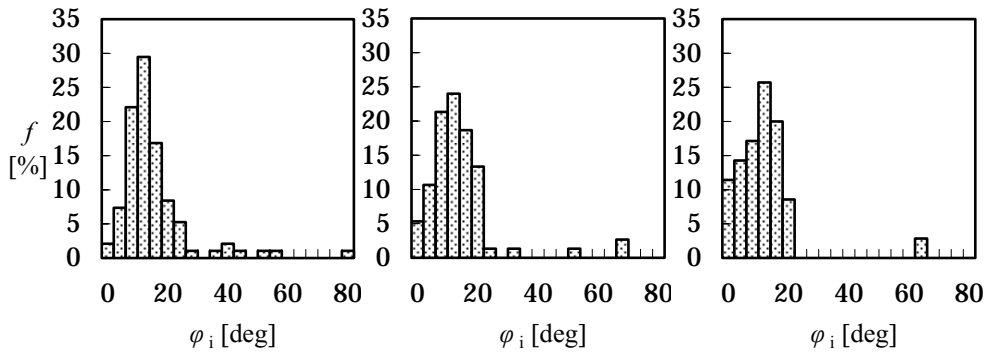


Fig. 5.9: Surface B.

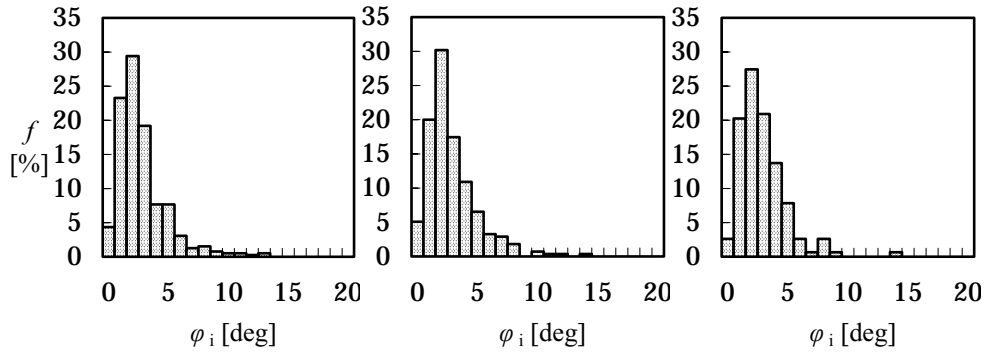


Fig. 5.10: Surface C.

(a)
 $h/R_q = 1.0$

(b)
 $h/R_q = 1.5$

(c)
 $h/R_q = 2.0$

Histograms of the attack angles of the asperities for surfaces A, B and C obtained using the deterministic model.

Therefore the obtained distributions of asperity attack angles as presented in Fig. 5.8, Fig. 5.9 and Fig. 5.10 result in calculated wear rates that are negligible. Presently, experimental results linking the degree of wear to the asperity attack angle are not available and therefore in the remainder of this thesis, only results of the deterministic model with paraboloidal shaped asperities will be discussed.

5.4.1.2 Deterministic model with paraboloidal shaped asperities

Fig. 5.11 shows three histograms for the radii of the asperities on surface A, as calculated using the deterministic model and the paraboloid fitting method. The line marked R_{st} represents the average radius applied in the statistical contact model, as determined using nine point summit identification and finite differences to calculate the radius, as described by de Rooij [26], see also Appendix B.3.

As explained before, this statistical value is calculated taking into account all summits on the surface, and therefore it is independent of the mean plane separation. Furthermore, it can be seen that the nine-point summit identification function and determination of the asperity radius using finite differences generally results in an average asperity radius that is of the same order of magnitude as the deterministic method with load and energy equivalence. Note that the x-axis represents the logarithm of the asperity radius. This is done because of the large variation in measured radii, ranging from approximately $1 \mu\text{m}$ to $200 \mu\text{m}$. Similar to the observations for the attack angles of the conical asperities, the distribution of asperity radii is rather insensitive to the mean plane separation of the surfaces in contact. This observation is also valid for even smaller mean plane separations, like $h/R_q = 0$ and $h/R_q = 0.5$.

For surface B the distribution of the radii is presented in the histograms of Fig. 5.12. For this surface the statistical average radius approximates the average deterministic radius quite well. Again the range of calculated asperity radii covers several orders of magnitude. The distribution of the asperity radius is relatively independent of the mean plane separation between the two surfaces.

The histograms of the asperity radii for surface C are presented in Fig. 5.13, again at three values of the normalised mean plane separation. Some large asperities are found, with a radius up to $1000 \mu\text{m}$, as well as several small asperities, with radii in the order of tenths of micrometers. However, the majority of the asperities has a radius in the order of several micrometers. Again, the obtained radii are somewhat smaller than the average asperity radius obtained for the statistical model and the distribution of asperity parameters hardly depends on the mean plane separation.

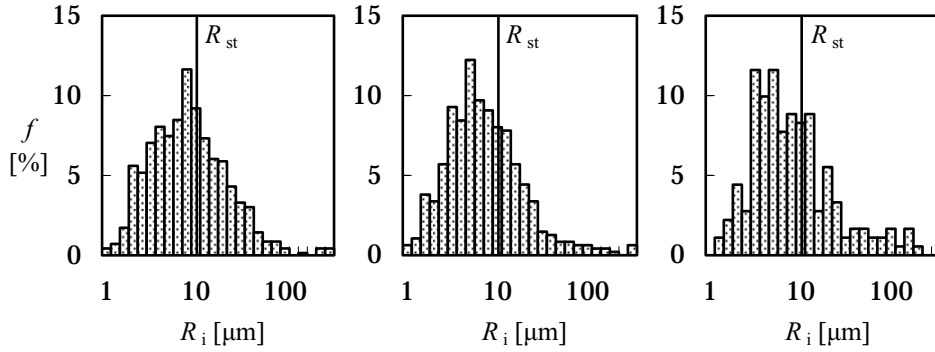


Fig. 5.11: Surface A.

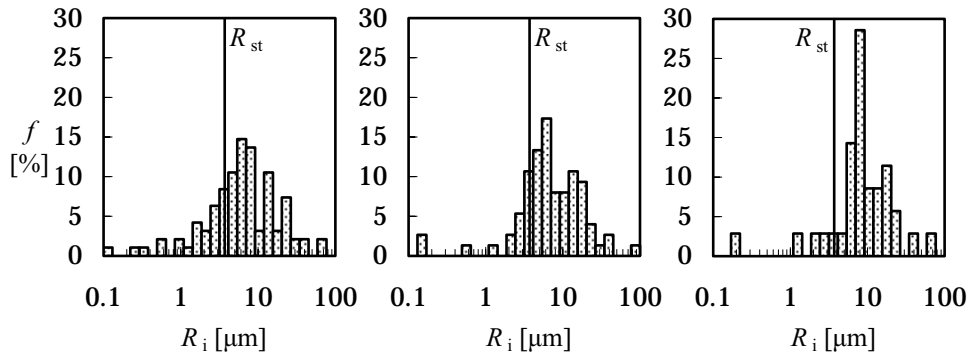


Fig. 5.12: Surface B.

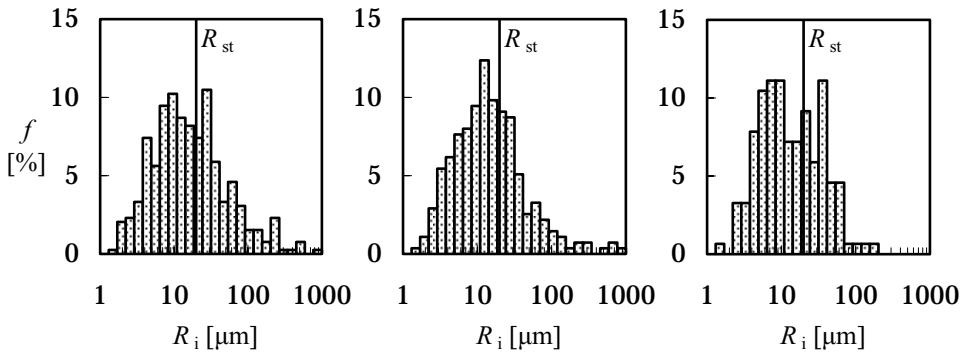


Fig. 5.13: Surface C.

(a)
 $h/R_q = 1.0$

(b)
 $h/R_q = 1.5$

(c)
 $h/R_q = 2.0$

Histograms of the radii of the asperities for surfaces A, B and C obtained using the deterministic model.

Fig. 5.14(a), (b) and (c) show the distribution of asperity radii R as a function of the normalised height z_i/R_q of the asperity, for three values of the mean plane separation between the surfaces. It appears that most of the large asperity radii are found for asperities that just slightly contact the counter surface, so $z_i = h$. At a large mean plane separation the micro-contacts are relatively isolated on the surface and follow the observations for summits by Greenwood [39], that the curvature ($= R^{-1}$) of a summit increases with its height. At smaller values of the mean plane separation, for instance as shown in Fig. 5.14(a), the distribution of heights and radii of the asperities shows a more diffuse cloud.

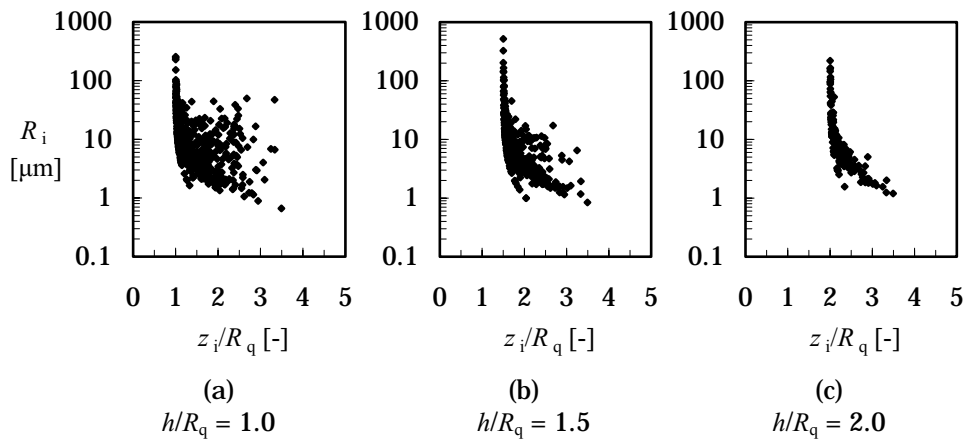


Fig. 5.14: Distribution of the radii of the asperities as a function of the asperity height, for surface A.

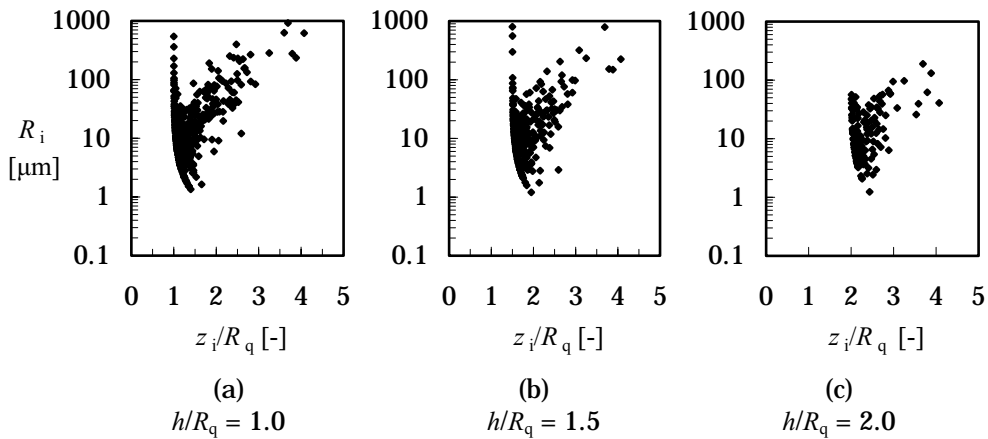


Fig. 5.15: Distribution of the radii of the asperities as a function of the asperity height, for surface C.

Roughly, the plots in Fig. 5.15 present a similar distribution for the asperities on surface C. However, some very large radii are found even at a large mean plane separation. These large asperities are a result of the low-frequency nature of the surface roughness in comparison to surface A and are expected to dominate the contact behaviour of the surface.

5.4.2 Contact

The plots in Fig. 5.16 show the calculated normalised contact pressure p/H as a function of the normalised mean plane separation h/R_q , for each of the three surfaces.

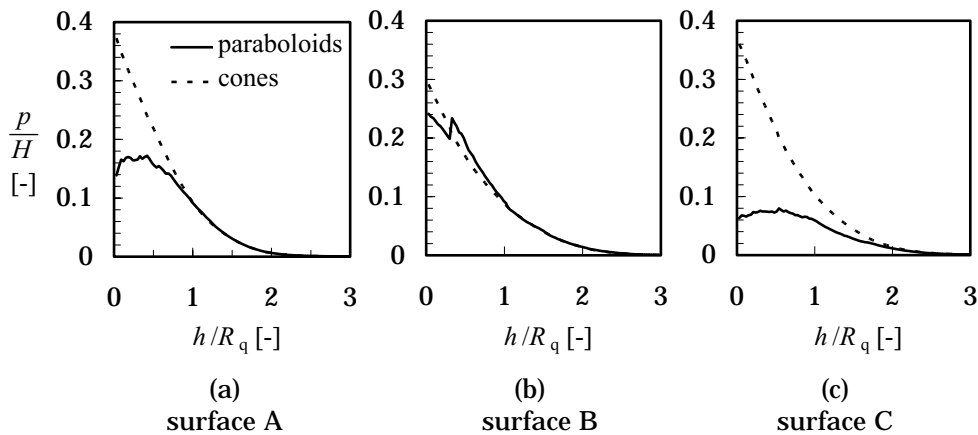


Fig. 5.16: Normalised contact pressure p/H as a function of the normalised mean plane separation.

The solid line represents results obtained with paraboloidal shaped asperities, while the dashed line depicts the results for conical shaped asperities. As long as the mean plane separation is not too small, the applied asperity shape only has a minor effect on the outcome, for each of the three surfaces. For very small mean plane separations there is a substantial difference in results.

For paraboloidal shaped asperities, with decreasing separation the asperities merge, forming a large asperity that deforms elastically. This results in a lower value of the normalised contact pressure. In case of a large conical asperity, the limit for elastoplastic contact is not reached and therefore the normalised contact pressure increased with decreasing mean plane separation. Therefore, the choice of asperity shape can result in some differences in calculated contact behaviour.

As discussed in Chapter 3, in fully elastic scratching the entire normal area of the asperity is in contact with the counter surface, while in pure plastic scratching only the front half of the asperity is in contact with the counter

surface. Consequently, in fully elastic sliding the fraction of area in contact equals the bearing area, while in fully plastic scratching this fraction only covers half the bearing area. With this, the surface deformation index \mathcal{A} can be defined as the calculated contact area divided by the bearing area of the surface as defined by Abbott and Firestone [1]. For a perfectly plastic deforming surface, this surface deformation index equals 0.5, while in elastic deformation $\mathcal{A} = 1$.

In Fig. 5.17 \mathcal{A} is plotted as a function of the normalised mean plane separation for each of the three surfaces, and for both conical and paraboloidal shaped asperities. From these graphs it follows that there can be a substantial difference in the amount of elastoplasticity with changing mean plane separation and selected asperity shape.

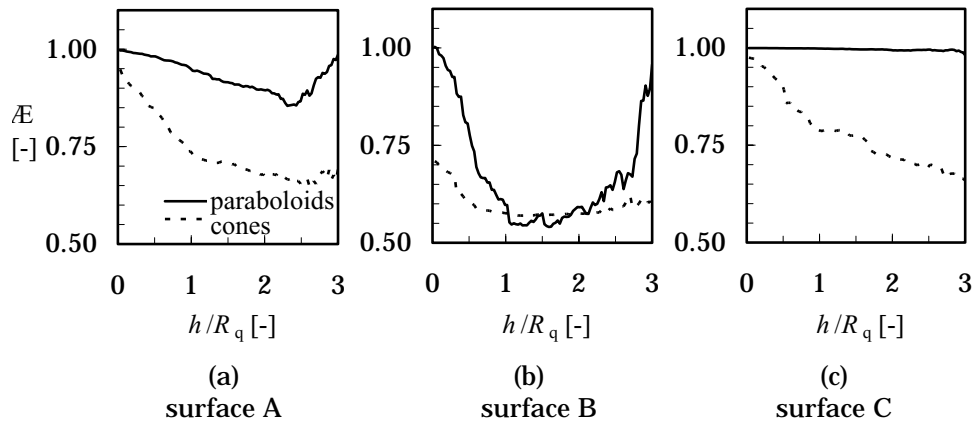


Fig. 5.17: Surface deformation index \mathcal{A} as a function of the normalised mean plane separation.

Surface A operates in the elastoplastic deformation mode, but the amount of elastoplasticity depends on the mean plane separation. At a large value of the mean plane separation the asperities on the surface deform elastically because the indentation depth is relatively small. With decreasing mean plane separation, the indentation depth of the asperities increases and plasticity becomes more important. Finally, at a very small separation, contact spots merge and a limited number of elastically deforming large micro-contacts are formed. This behaviour is in agreement with the observations of Whitehouse and Archard [114] and Majumdar and Bhushan [71] that large micro-contacts will behave elastic, see also Greenwood and Wu [41].

Comparing the curves for surfaces A and C, which have a similar surface roughness R_q , shows the influence of the surface micro-geometry. While surface A is mainly elastoplastic, the asperities on surface C deform

elastically. In Fig. 5.7(b) it was already observed that, at the calculated separations, the number of micro-contacts on surface C is smaller than the number of micro-contacts on surface A, implying that generally at equal mean plane separation a typical micro-contact on surface C is larger than a micro-contact on surface A. Furthermore, in Fig. 5.15(c) it was observed that some very large micro-contacts are formed on surface C, which might dominate the contact behaviour.

In the contact with surface B mainly elastoplastic or fully plastic deformation occurs, depending on the mean plane separation between the two surfaces. At a large separation the contact is elastoplastic. With decreasing separation the value of $\bar{\epsilon}$ drops close to 0.5, indicating fully plastic behaviour. As observed before, at an even smaller separation, a small number of large elastically deforming micro-contacts dominate the contact.

The plots in Fig. 5.18 show the distribution of load carried by the individual asperities N_i as a function of the contact area of the asperity A_i , for paraboloidal shaped asperities on surface A. As can be expected, the load carried by the asperities increases with increasing asperity size. Furthermore, as was observed before, with decreasing mean plane separation the area of the asperities grows. Again, this figure confirms that the large asperities operate in the elastic contact mode as was suggested by Majumdar et al. [71] based on a fractal model of the contact of rough surfaces.

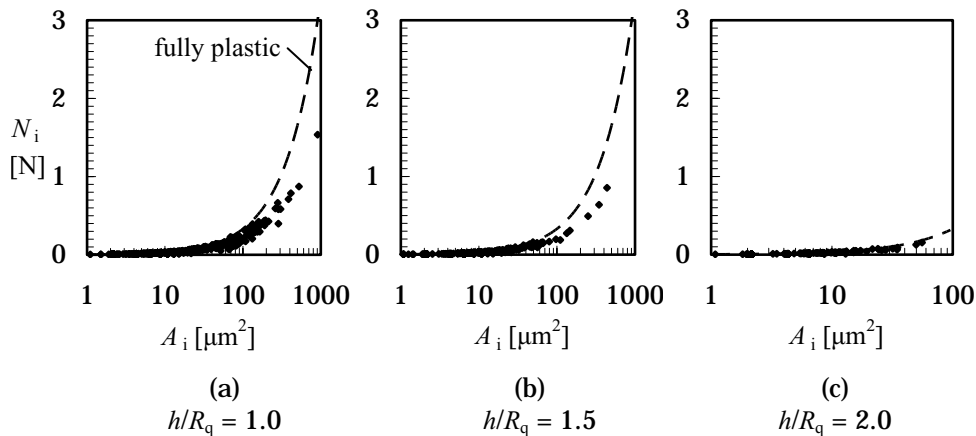


Fig. 5.18: Distribution of the load carried by the individual asperities as a function of the contact area, for surface A.

5.4.3 Abrasive wear

5.4.3.1 Degree of penetration

The total volumetric abrasive wear caused by the sliding contact between two surfaces is a summation of the contributions of all individual asperities. The distribution of the degree of penetration $D_{p,i}$ of the asperities as a function of their radius R_i for surface A and C is shown in Fig. 5.19 and Fig. 5.20 respectively. The majority of the asperities has a relatively low degree of penetration and will cause only a limited amount of volumetric wear.

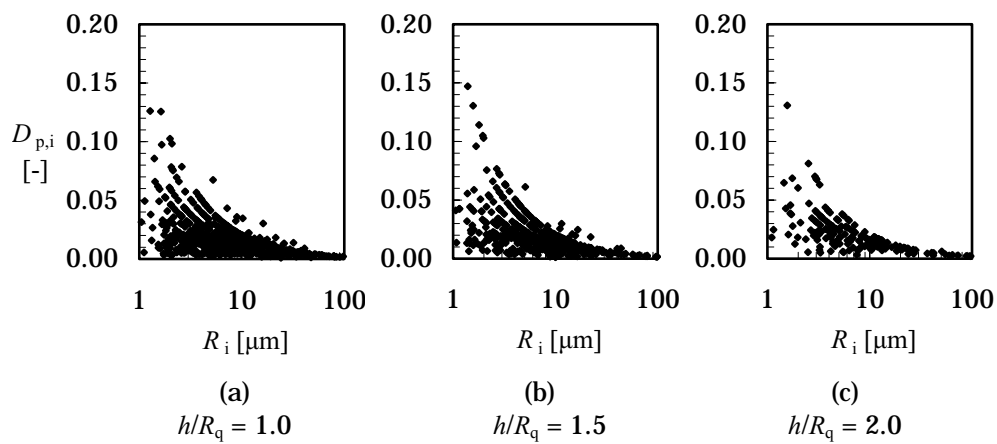


Fig. 5.19: Distribution of the degree of penetration of the individual asperities as a function of the radius, for surface A.

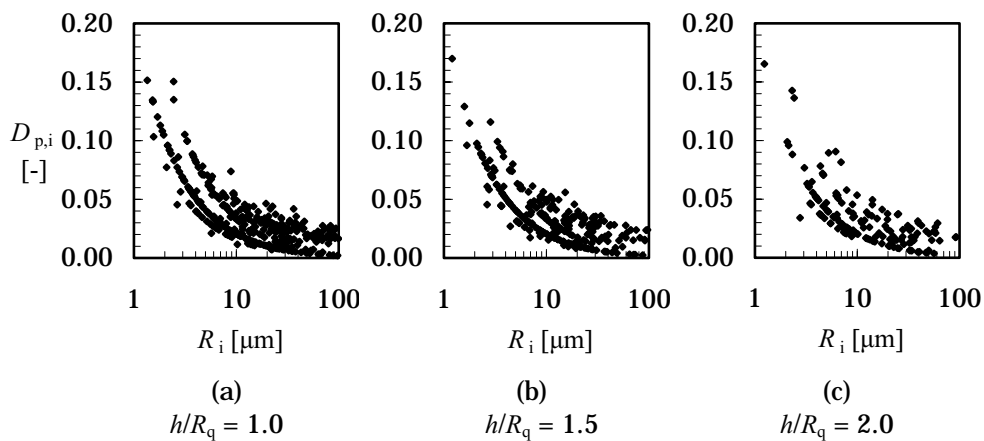


Fig. 5.20: Distribution of the degree of penetration of the individual asperities as a function of the radius, for surface C.

The difference between the distributions for both surfaces is striking. For surface A, at small mean plane separations a large number of small asperities with a low value of D_p are formed, indicating that these asperities contribute little to the abrasivity of the surface. In contrast, the values of the degree of penetration of the asperities on surface C are relatively high, and more highly abrasive asperities are formed with decreasing mean plane separation. Therefore, the micro-geometry of surface C might be more abrasive than surface A, although it has fewer asperities contacting the counter surface.

5.4.3.2 Abrasive wear volume

The corresponding volumetric wear per sliding distance $\Psi_i = V_i \cdot L^{-1}$ caused by each asperity is plotted in Fig. 5.21. Note the logarithmic scale of the y-axis in the figures, indicating that there is a large spread in volumetric wear caused by each asperity. From the figures it can be concluded that the total abrasive wear volume caused by the hard rough surface is mainly determined by a small fraction of the asperities.

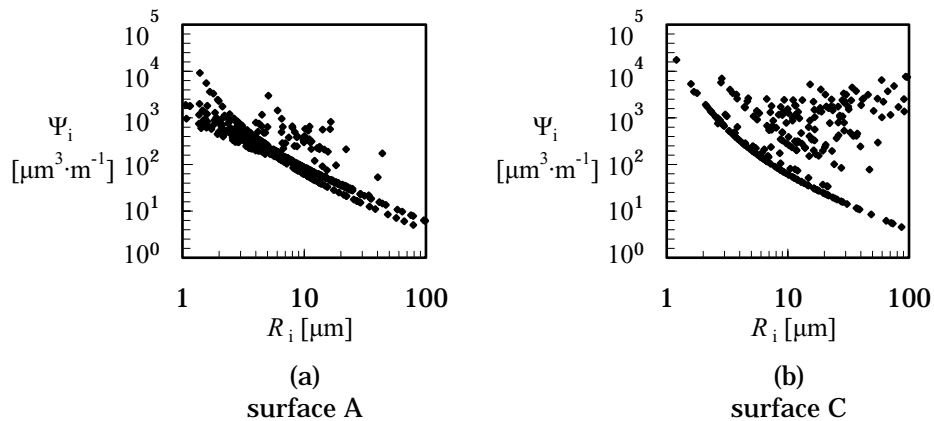


Fig. 5.21: Distribution of the volumetric wear per unit sliding distance caused by the individual asperities as a function of the radius, at a normalised mean plane separation $h/R_q = 1.5$.

In Fig. 5.22 this volumetric wear per unit sliding distance is plotted for each of the three surfaces A, B and C at three levels of the normalised mean plane separation. The results show that the rough surface B indeed causes a higher volumetric abrasive wear than the less rough surfaces A and C. Furthermore, the volumetric wear caused by the isotropic surface C is about twice the volumetric wear caused by the anisotropic surface A. As was observed in Fig. 5.19 and Fig. 5.20, the high anisotropy of the micro-geometry of surface A results in asperities having a low degree of wear ζ when compared to surface C. On top of that, the asperities have a small frontal area, a combination that leads to a relatively low wear volume.

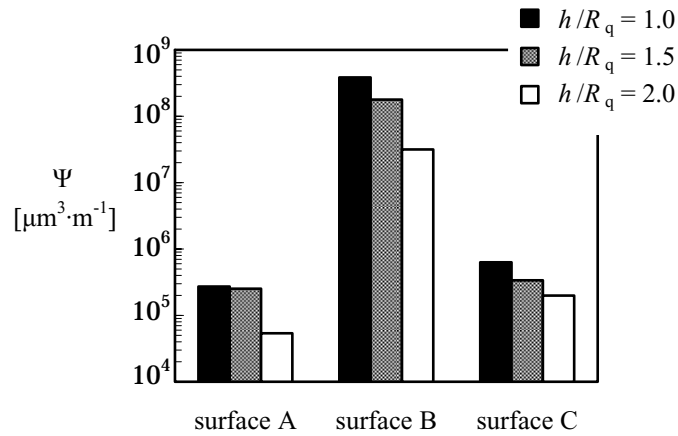


Fig. 5.22: Volumetric abrasive wear per unit sliding distance for the three surfaces at three values of the normalised mean plane separation.

The specific wear rate k is defined according to eq. (5.10) as the volumetric wear per unit sliding distance and unit load. Calculated values of k of the tribo-systems with the three surfaces A, B and C as a function of the normalised mean plane separation are shown in Fig. 5.23.

$$k = \frac{V}{N \cdot L} \quad (5.10)$$

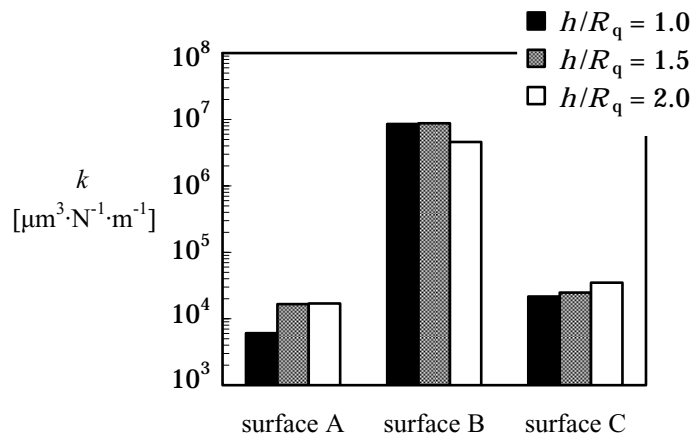


Fig. 5.23: Archard wear coefficient for the three surfaces at three values of the normalised mean plane separation.

It can be seen that for surface B the wear coefficient is approximately constant with changing mean plane separation, i.e. the abrasive wear volume changes linearly with the applied load on the contact, as was found by Archard [4]. This behaviour is not observed for surfaces A and C, although the various wear coefficients still have the same order of magnitude. This behaviour does not agree with the Archard relationship, but is however commonly found in experiments, see for instance Ravikiran and Jahanmir [88] and Kennedy et al. [65].

5.4.4 Effect of the orientation of the surface micro-geometry

The difference in results obtained for surfaces A and C was explained by the difference in surface micro-geometry. Surface A has relatively slender asperities, which result in relatively minor abrasivity, while the asperities on the isotropic micro-geometry of surface C cause higher abrasion. However, a consequence of this explanation is that surface A should be highly abrasive when the sliding direction is perpendicular to the orientation of the micro-geometry, because the asperities have a larger degree of penetration D_p and therefore a higher degree of wear ζ at the same indentation depth, as well as a larger frontal area.

The effect of the orientation of the micro-geometry of the abrasive surface on the abrasive wear volume is illustrated in Fig. 5.24. In this figure the abrasive wear volume caused on a soft surface by the sliding of surfaces A and C is shown. The results referred to as 'surface A // ' and 'surface C // ' represent the situation as illustrated in Fig. 5.6, with the sliding direction parallel to the surface micro-geometry of surface A. In contrast, the results marked 'surface A \perp ' and 'surface C \perp ' correspond to a sliding direction perpendicular to the initial sliding direction. As can be expected, for the isotropic surface

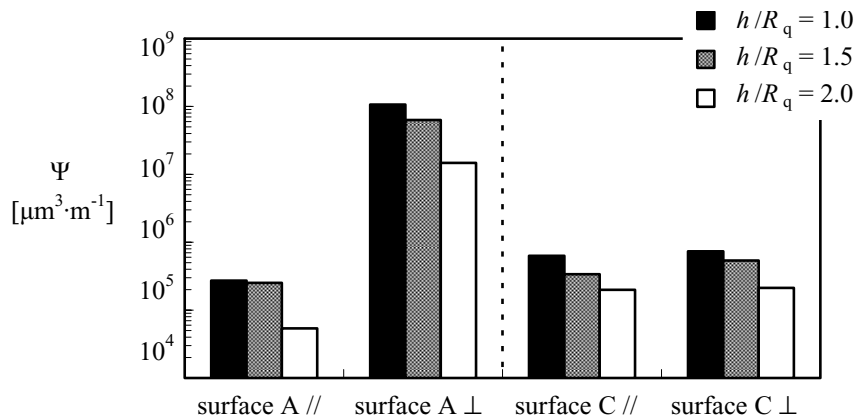


Fig. 5.24: Volumetric wear per unit sliding distance for the three surfaces at three values of the normalised mean plane separation.

micro-geometry there is only a minor difference in results and the volumetric wear can be considered independent of the orientation of the micro-geometry with respect to the sliding direction. For the anisotropic surface the situation changes dramatically, with a resulting wear volume that is approximately two orders of magnitude larger than when sliding occurs in the direction of the micro-geometry.

5.4.5 Effect of the hardness of the abraded material

The effect of the hardness of the abraded material on the specific wear rate k is illustrated in Fig. 5.25. In this graph the calculated volumetric abrasive wear caused by surface B at a mean plane separation $h = 1.5 \cdot R_q$ is plotted as a function of the hardness H of the abraded surface. After an initially steep decline of k with increasing H , a levelling off of the curve can be observed. This is caused by the increased range of elastic deformation (recall $d_{e,trans} \sim H^2$ as discussed in Appendix B.1). The plot shows that $k \sim H^{-1.1}$, which agrees with results presented by Kato [62], as well as with the rule of thumb that the Archard wear coefficient K , defined as $K = k \cdot H$, is approximately constant.

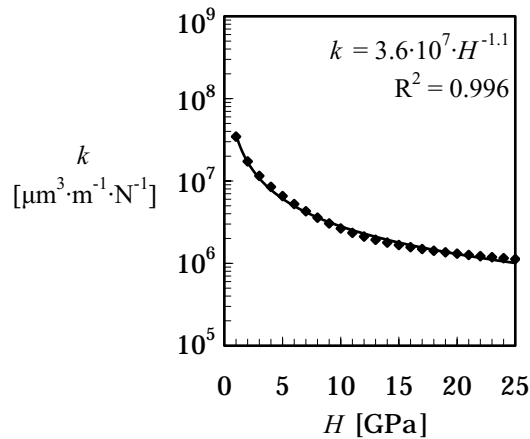


Fig. 5.25: Archard wear coefficient as a function of the hardness of the abraded material at three values of the normalised mean plane separation.

5.4.6 Hard surface layers

Generally, the application of a protective layer affects both the load bearing capacity of the surface as well as the abrasion resistance of the surface. In the previous section only the effect of changing the hardness (i.e. the load bearing capacity) of the abraded surface was examined. It was assumed that the abrasion resistance, represented by the relation between the degree of penetration D_p and the degree of wear ζ , remained constant. In Chapter 4 some relations between D_p and ζ were experimentally obtained for bodies covered with a hard surface layer.

The grey bars in Fig. 5.26 show the specific wear rate k for the contact between surface B and softer surface that are coated with protective surface layers, using the empirical relations between D_p and ζ as obtained in Chapter 4. Note that in this graph the y-axis is linear, i.e. also minor changes in the wear coefficient are clearly shown. GGG70L symbolises uncoated nodular cast iron, while the bar marked St6 represents the results for nodular cast iron with a 1 mm thick stellite 6 layer and St6 + CrN represents the results for the stellite 6 + 5 μm chromium nitride duplex layer.

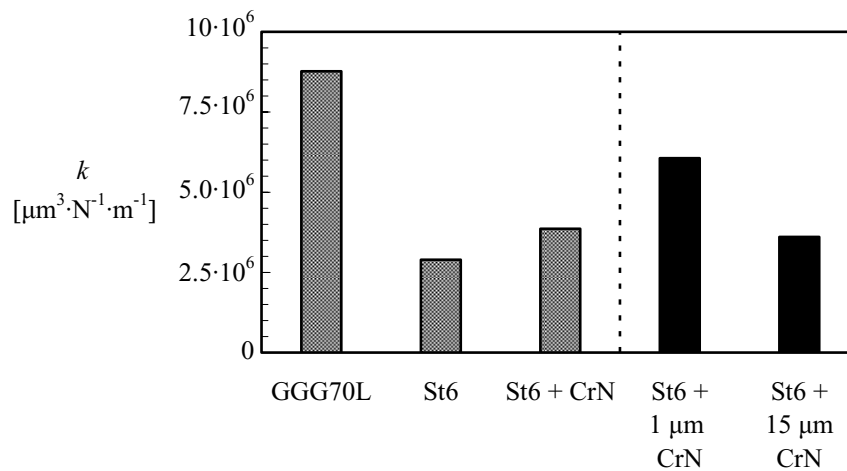


Fig. 5.26: Specific wear rate for surface B sliding against uncoated nodular cast iron, nodular cast iron with a stellite 6 layer and nodular cast iron with stellite 6 + chromium nitride duplex layers.

It can be seen that the application of the hard stellite 6 surface layer to the nodular cast iron substrate diminishes the specific abrasive wear rate k threefold. In contrast, coating the stellite surface with an additional 5 μm chromium nitride layer *increases* the volumetric wear by approximately 30 percent. This is caused by the altered $D_p - \zeta$ relation of the chromium nitride layer with respect to stellite 6. The increase of the load bearing capacity due to the application of the layer is not sufficient to prevent an increase of the wear rate k .

The thickness of the chromium nitride layer is varied in order to alter the load bearing capacity of the surface, while keeping the $D_p - \zeta$ relation for the duplex layer constant. The results are shown as the black bars in Fig. 5.26. It can be seen that applying a chromium nitride layer of 1 μm thickness on top of the stellite 6 results in a duplication of the abrasive wear. Increasing the layer thickness from 5 μm to 15 μm only results in a marginal decrease of the specific wear rate k .

5.5 Discussion

In this chapter a model for the abrasive wear caused by a rough surface was developed. The model is based on the contact and wear behaviour of the so-called unit-event of a single asperity. In the contact between two surfaces, actual surface to surface contact only occurs in the micro-contacts. These micro-contacts are approximated by simple geometrical shapes, i.e. cones and paraboloids, of which the contact behaviour can be described using straightforward equations.

First step in the model is to find the representing or equivalent asperity of each micro-contact. The representing asperity has the same normal area and indentation volume as the original micro-contact, resulting in equivalent load and energy behaviour of the asperity and the micro-contact in fully plastic deformation. In the case of conically shaped asperities, attack angles ranging from 0 to approximately 20° were obtained, indicating that the surface micro-geometry shows relatively shallow slopes. For paraboloidal shaped asperities, the obtained range of radii is relatively large, ranging from tenths of a micrometer to several hundred micrometers. The most extreme values in this range are obtained for asperities that are just slightly in contact with the counter surface.

As could be expected, with increasing approach between the two surfaces both the size of the asperities as well as the load carried by each asperity increases. At a large distance between the two surfaces the contact is mainly elastic, and with increasing approach (or decreasing separation) the contact becomes more plastic, until eventually a 'macro-sized' micro-contact is formed, resulting again in predominantly elastic deformation.

From both experimental results as well as calculations it follows that the behaviour of the surfaces in contact is highly dependent on their surface micro-geometry. However, the results of the contact model are mainly independent of the selected type of asperity geometry, i.e. the load at a given separation as calculated using conical asperities equals the load calculated using paraboloidal asperities.

The abrasive wear behaviour of the asperities is described by empirical relations. In the previous chapter these were experimentally determined for paraboloidal shaped asperities. Therefore the emphasis in this chapter is on modelling using paraboloidal shaped asperities.

When it is assumed that the individual micro-contacts operate independent of their neighbours, the abrasive wear volume in a macro-scale tribological system is merely a summation of the individual asperity wear volumes. This volumetric abrasive wear depends on the material properties of the abraded

surface, the contact conditions of the tribological system as well as on the micro-geometry of the abrasive surface.

The calculated results show the specific wear rate to decrease slightly with increasing load. This behaviour is in agreement with results reported in literature. Furthermore, the influence of surface roughness is significant; an increase in surface roughness tends to result in a much higher wear volume.

Also the shape of the micro-contact and the directionality of the micro-geometry have a considerable effect. For a highly anisotropic surface the wear rate can change several orders of magnitude with changing sliding direction. This behaviour can be visualised with a winter-sports equivalent: in ice-skating, when the skates are positioned parallel to the moving direction of the skater the volumetric wear of the ice is negligible, while an perpendicular orientation of the skates with respect to the moving direction results in severe damage to the skating rink.

There is also a substantial influence of the hardness of the abraded material on the volumetric abrasive wear. Assuming unaltered micro-wear behaviour of the abraded surface, the model indicates that the specific wear rate tends to decrease with increasing hardness following $k \sim H^{-1.1}$, i.e. the Archard wear coefficient is approximately constant. For hard surface layers with empirically determined micro-wear behaviour, a significant decrease of the abrasive wear can be obtained. For thin coatings the layer thickness is decisive, as it directly affects the load bearing capacity of the layer.

Chapter 6

Abrasive Wear in Deep Drawing of Tailor Welded Blanks

6.1 Introduction

In this chapter the developed model will be applied to the practical situation of deep drawing of tailor welded blanks. Laboratory scale experiments of the deep drawing of tailor welded blanks are discussed. Furthermore, the developed model is applied to these experiments, enabling comparison of the calculations and the experiments. Finally, the model is used to present some guidelines for the prevention of abrasive tool wear in sheet-metal forming processes.

6.2 Deep drawing simulations

Abrasive wear experiments are performed on the contact between the tool and the tailor welded blank using a laboratory scale deep drawing simulator.

6.2.1 Experimental set-up

The experimental set-up is composed of a tensile tester and a tribo-tester, as schematically illustrated in Fig. 6.1 and simulates the contact between the forming tool and the deforming tailor welded blank. A strip of the tailor welded blank is clamped in the tensile tester and stretched. The tribo-tester is mounted on the tensile tester and can move vertically along the sheet. A specimen of the tool material is positioned as the sliding tool in the tribo-tester. The experimental set-up is explained in more detail by ter Haar [99] and de Rooij [26]. In Appendix C.2 some pictures of the experimental set-up are shown.

Using the bellows a normal force is applied on the contact between the sliding tool and the sheet. By moving the tribo-tester down along the sheet, the weld scratches through the tool material, creating a wear scar. The dimensions of the wear scar can be measured using an optical interferometer and from the measured height data the volumetric wear can be determined.

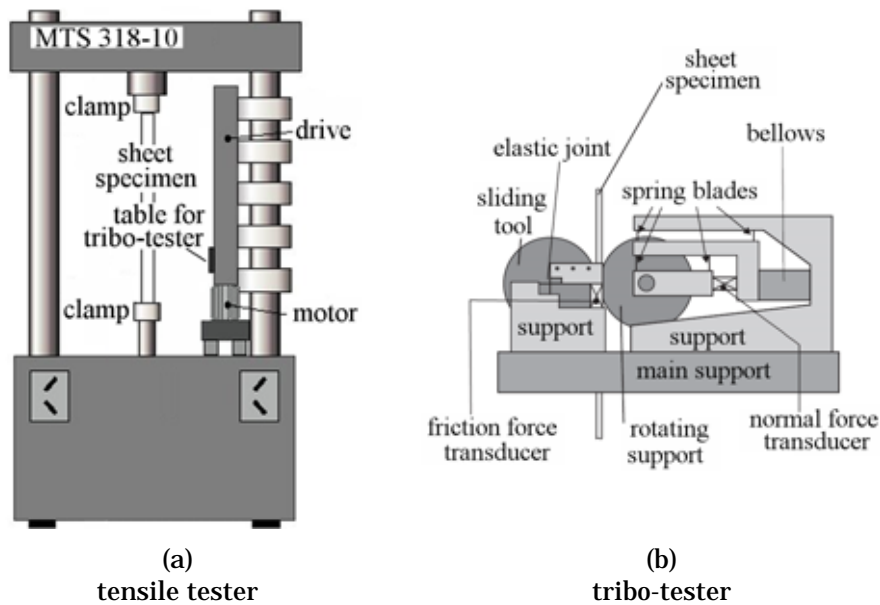


Fig. 6.1: Deep drawing simulator.

6.2.1.1 Tool specimens

A schematic drawing of a tool specimen is shown in Fig. 6.2. The tool specimen has a cylindrical body with a diameter of 20 mm and a width of 34 mm. The ten-sided sections on both sides of the specimen are used for mounting the specimen on the tester. The specimens are made of nodular cast iron, coated with a variety of commercially available hard surface layers. The

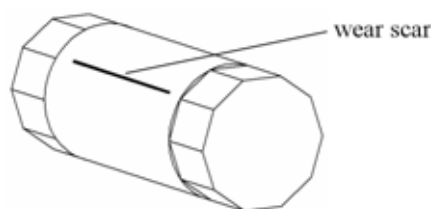


Fig. 6.2: Tool specimen with wear scar (schematically).

samples are ground to an R_q roughness of $0.3 \mu\text{m}$. For the thin coatings, this grinding is done prior to the coating process. It was shown by de Rooij [26] that the application of a thin coating does not significantly affect the surface micro-geometry of the tool material. For the thick surface layers the grinding is done after the application of the surface layer. Some properties of the tool material and the coatings are listed in Appendix A.1 and A.2 respectively. The experimentally investigated coated tools are listed in Table 6.1.

Table 6.1: Tested tool materials in the deep-drawing simulator.

Substrate material	Coating	Coating process	Thickness [μm]
GGG70L	none	-	-
GGG70L	Titanium Nitride (TiN)	PVD	3.2
GGG70L	Metal-Carbon (MC)	PVD	4
GGG70L	Hard Chromium (HCr)	Electroplating	15
GGG70L	Cobalt based alloy A (St6)	Laser cladding	10^3
GGG70L	Cobalt based alloy B (Ult)	Laser cladding	10^3

6.2.1.2 Tailor welded blank specimens

The tailor welded blank specimens, as shown in Fig. 6.3, are produced by laser welding of DC05 sheet-metal. In contrast to a 'real' tailor welded blank, which is composed of multiple sheets, the specimens are produced by welding on a single sheet. This is done to avert any effects caused by any mismatch of the sheets. The tailor welded blank specimens have two parallel welds, enabling proper alignment of the sheet and the tool specimen. The distance between the two welds is 10 mm. The welds show a repetitive zigzag pattern, resulting in a line shaped wear scar on the tool material as indicated in Fig. 6.2. Properties of the sheet material and the welds are listed in Appendix A.3.

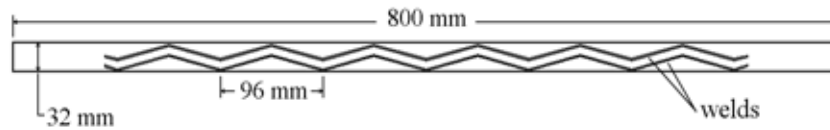


Fig. 6.3: Tailor welded blank specimen.

A three dimensional representation of the surface micro-geometry of the weld is shown in Fig. 6.4(a) and (b). Some additional images of the welds on tailor welded blanks are shown in Appendix A.3.1. It can be seen that the weld is quite rough and sticks out of the surface.

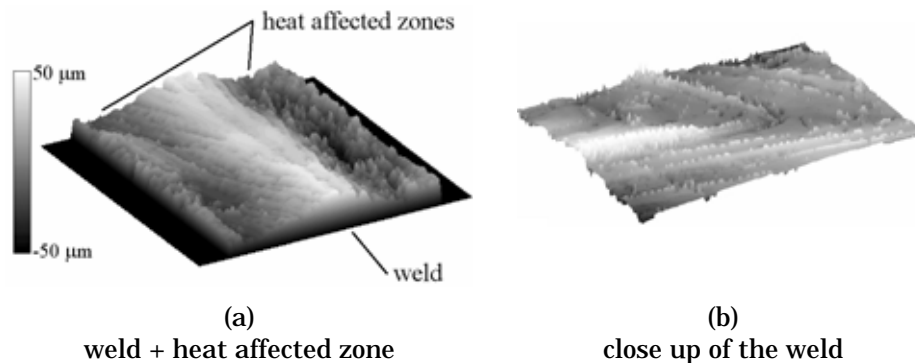


Fig. 6.4: Surface micro-geometry of a laser weld in a tailor welded blank.

6.2.1.3 Testing procedure

The sheet, which was stored in conservation oil, is cleaned with ethanol. Subsequently, using a drenched cloth a new layer of oil is applied. The lubricant applied in these experiments is Quaker Ferrocoat N6130, which is a conservation oil with some deep drawing lubricating properties. The lubricant has a dynamic viscosity of 55 mPa·s at 22° C.

The sheet is clamped into the tensile tester and the tool specimen is positioned into the sliding tool holder of the tribo-tester. The normal load is applied on the contact using the bellows and subsequently the vertical motion of the tribo-tester is started. After the test, the volumetric wear of the tool specimens is measured using an optical interferometer. The parameters and settings of the deep drawing wear experiments are listed in Table 6.2.

Table 6.2: Parameters in the deep drawing simulations.

normal load	N	300 N
velocity	v	40 mm·s ⁻¹
sliding distance	L	400 mm

6.2.1.4 Tool - tailor welded blank contact

When the blank is considered flat, the contact between the tool and the blank is a line contact and the load of 300 N causes a nominal contact pressure of 135 MPa. However, the surface of the tailor welded blank is not flat, and the welds stick out of the blank surface. Macroscopically, a single weld can be considered as a cylindrical bulge on the surface of the blank, changing the contact situation to that of crossed cylinders. From a cross-section the radius of the weld is estimated at $R_{\text{weld}} = 2$ mm.

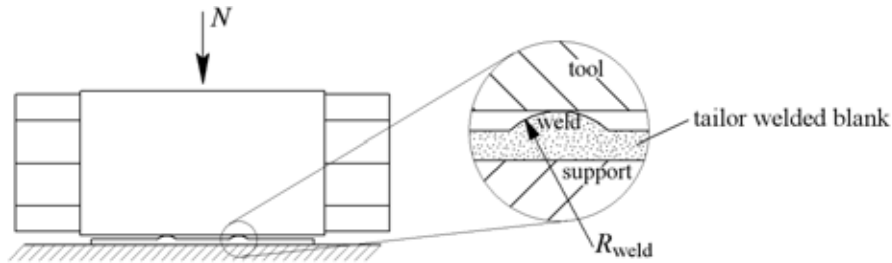


Fig. 6.5: Contact between tool and tailor welded blank in the experiments.

The contact situation is illustrated in Fig. 6.5. With a normal load $N = 300$ N, each tool-weld contact carries a load of 150 N, resulting in a nominal elastic contact pressure of 1.77 GPa. The resulting contact spot between the uncoated nodular cast iron tool and the weld is 558 μm long and 194 μm wide.

6.2.2 Experimental results

The results of the experiments are shown in Fig. 6.6. The uncoated nodular cast iron shows the highest wear rate of the six tested surfaces. The surfaces coated with a protective layer show specific wear rates that are significantly lower. The lowest wear rates are found for titanium nitride, hard chromium and the cobalt-based clad layers.

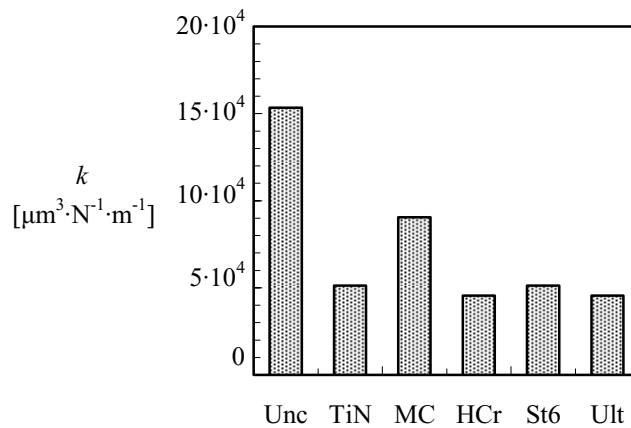


Fig. 6.6: Results of the deep drawing simulator experiments.

From the experiments it follows that the application of a hard surface layer has a beneficial effect on the wear resistance of the tool, i.e. the specific abrasive wear rate k decreases. For both titanium nitride as well as chrome plating the amount of wear can decrease a factor three, which is consistent with the results of Vermeulen [111].

Comparing these results with the hardness data of the applied surface layers, as listed in Appendix A.2 shows there is no direct relation between the hardness of the deposited layer and the abrasive wear resistance of the tool body. The thin surface layers titanium nitride and hard chromium show an approximately equal specific wear rate, while the hardness of titanium nitride is almost 3 times as high. Furthermore, the cobalt based clad layers show a lower specific wear rate than expected from their hardness alone.

6.2.3 Modelled results

In chapter 4, empirical relations for the single asperity wear behaviour were obtained for both the uncoated nodular cast iron and stellite 6 coated nodular cast iron. Hence, for these materials the experimental deep drawing results can be compared with results of the model. In these calculations the contact condition as explained in section 6.2.1.4 is assumed, i.e. each weld has a radius of 2 mm and carries a load of 150 N. Results for both the uncoated nodular cast iron and the stellite 6 coated tool specimens are shown as the dark coloured bars in Fig. 6.7.

It appears that the results calculated using the model approximate the behaviour of the tool-tailored blank contact quite reasonable. The calculated wear rates k are slightly lower than the experimental values. The results indicate that the abrasive wear behaviour of the tool - tailor welded blank contact can be quantitatively described by the developed model.

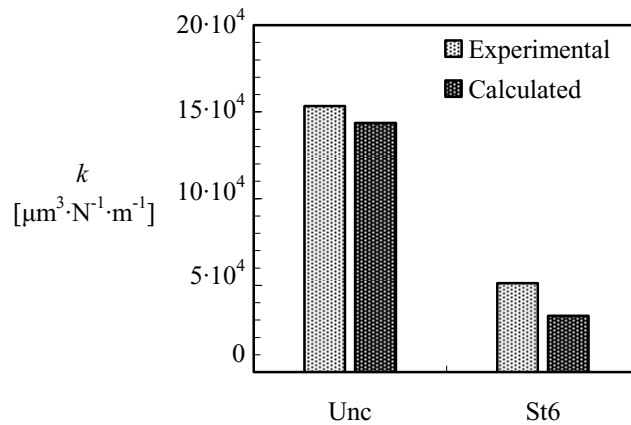


Fig. 6.7: Comparison of calculated and experimental drawing simulator results.

6.3 Improving the wear resistance in deep drawing

The abrasive wear in a contact is influenced by the micro-geometry of the bodies in contact, their hardness and their sensitivity to abrasion. In this section these three variables will be studied in the case of a tailor welded blank in contact with a forming tool. First the surface micro-geometry of the weld is altered. Subsequently, the influence of hardness and sensitivity to abrasion is studied using the model on some alternative forming tool materials.

6.3.1 The weld on the tailor welded blank

The surface roughness of the deep drawing tool is of the order of $R_q = 0.3 \mu\text{m}$ which is much smaller than the roughness of the weld. Therefore the tool can be considered smooth. The micro-geometry of the weld can be represented by a series of V-shaped ridges, with a slightly lower gutter in the centre. Hence the micro-contacts between weld and sheet can be approximated by highly elliptic paraboloids, as illustrated in Fig. 6.8(b).

The V-shaped pattern of the weld suggests the possibility to change the micro-geometry of the laser weld by adjusting the welding parameters. For example, by increasing the forwards velocity of the laser, the inclination angle β of the V-shaped ridges with respect to the central line of the weld might be altered. In that case the power of the laser beam has to be increased as well in order to keep the welding energy constant. Below, the wear behaviour of the weld is studied using a simplified model of the micro-geometry of the weld.

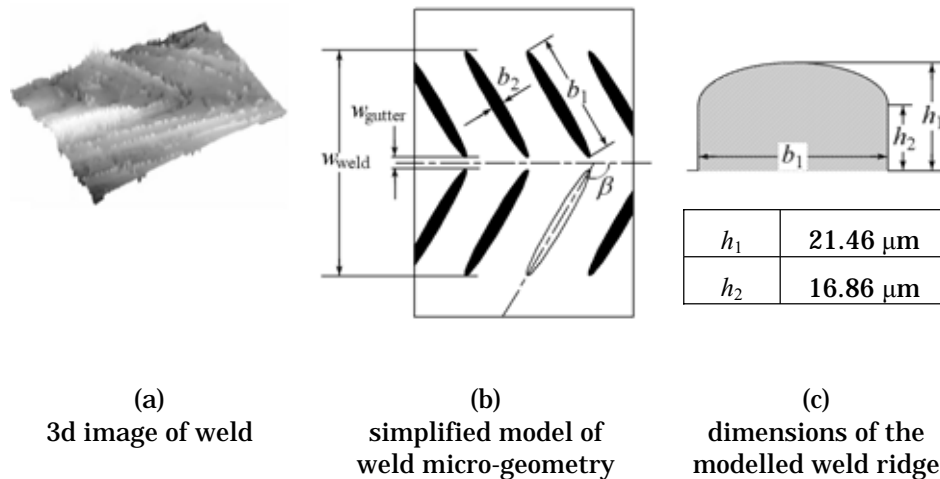


Fig. 6.8: Dimensions of the weld in a tailor welded blank.

6.3.1.1 Modelling the weld

The 'real' weld and the modelled weld should show identical contact and wear behaviour, i.e. the area, the inclination angle β , the load-displacement relation and the wear behaviour should be equal.

From the surface micro-geometry of the weld the dimensions of both the weld and the V-shaped ridges can be estimated. The width w_{weld} of the weld is about 230 μm . The width w_{gutter} of the central 'low part' or gutter of the weld is approximately 30 μm , while the inclination of the ridge β is 160°. A surface height measurement with a length of 867.5 μm covers 12 ridges. Assuming the rest of the surface to be smooth, the V-shaped ridge is modelled as two adjacent elliptic paraboloids with an area $A_{\text{ridge}} = 2 \times 8500 \mu\text{m}^2$, which equals the area of the ridges on the weld. Finally, calculations based on the load and the volumetric wear result in the dimensions of the ridge as shown in Fig. 6.8(c).

The calculations and results presented in this section (6.3.1) only apply to one modelled ridge (i.e. two elliptic paraboloids.)

6.3.1.2 The inclination of the ridge β

In the following the inclination β of the ridge is varied, while keeping both the width of the weld and the area of the ridge constant. Therefore, the length to width ratio of the paraboloids change.

The calculated specific wear rates k for these tool-weld contacts are plotted in Fig. 6.9 as a function of the weld ridge inclination β . It can be seen that there

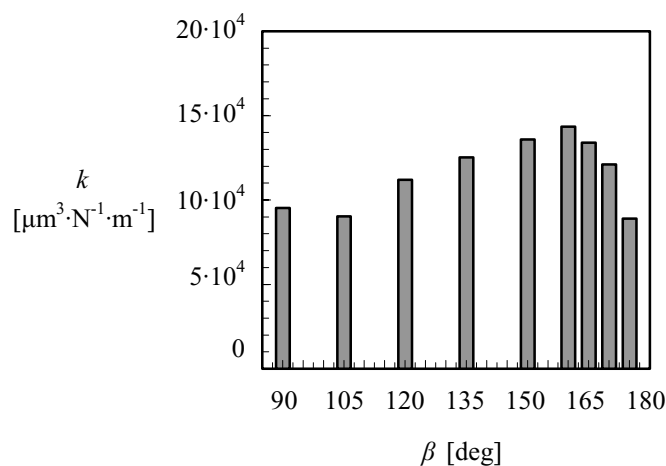


Fig. 6.9: Specific wear rate in the contact between tool and tailor welded blank as a function of the weld inclination angle β .

is a substantial influence of the shape of the weld on k . As a rule of thumb the inclination of the weld ridges should either be small or relatively large to prevent wear of the metal forming tool. 'Real-life' welds on tailor welded blanks show a value for β close to 160° , resulting in the highest wear. Therefore, adjusting the welding parameters can be beneficial to the wear behaviour due to the welds.

6.3.2 The forming tool

6.3.2.1 Alternative tool materials

As was discussed in Chapter 1, alternative tool materials are being considered in deep drawing. The developed model enables the prediction of the volumetric abrasive wear in the contact between these tools and the deforming product based on the results of a series of scratch tests. In the results presented below the micro-geometry of the 'real' weld is used again, and not the simplified weld model as discussed in the previous section.

Tool steel

Hokkirigawa and Kato [48] performed single asperity scratch tests on tool steels with various hardness. Their results were presented in Fig. 4.10, which is repeated below. The graph shows the degree of wear ζ as a function of the degree of penetration D_p of the contact between the single asperity and the tool steel specimen. The general trend in this graph is that at equal indentation depth, the sensitivity to abrasion ζ of a specimen increases with its hardness.

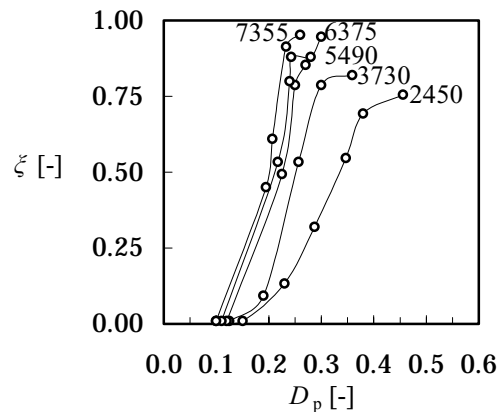


Fig. 6.10: Degree of wear as a function of the degree of penetration for heat treated tool steels with different hardness, ranging from 2.45 to 7.3 GPa. From Hokkirigawa and Kato [48].

Inserting these experimental scratch results into the model gives the specific wear rates shown in Fig. 6.11. For the softest steel the average contact pressure is well above the hardness, causing plastic bulk deformation and a very high wear rate. With increasing hardness the volumetric wear drops about two orders of magnitude.

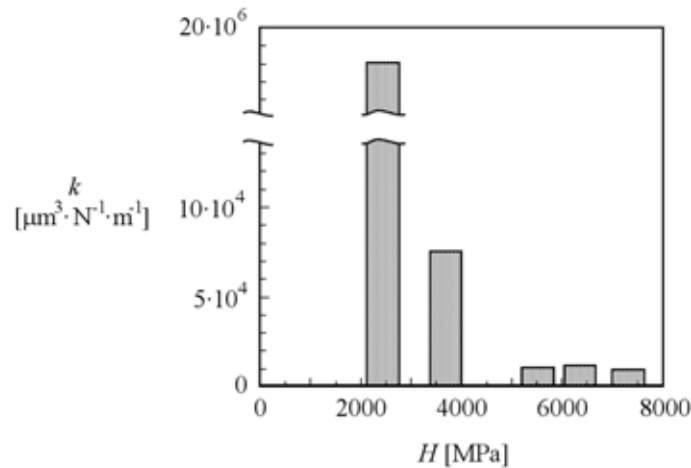


Fig. 6.11: Calculated specific wear rates for five heat treated tool steels.

For materials with a higher hardness, at identical load the weld penetrates less deep into the surface, on the other hand, an increased hardness results in a higher sensitivity to abrasion. This causes the approximately equivalent wear rates for the three bodies with the highest hardness.

Ceramics

Recently, Kataoka, Murakawa, Aizawa and Ike [60] presented work on the application of a range of ceramic materials as the tool material in unlubricated sheet-metal forming. They investigated alumina, zirconia, silicon carbide and silicon nitride tools and found promising results, particularly in the processing of zinc-coated sheets.

Ceramics materials are well known for their high hardness¹. In the preceding chapters it was observed that increasing the hardness of the tool material is only beneficial for wear prevention if the increase in load bearing capacity

¹ It was shown by Torrance [100] that abrasive wear only occurs if the difference in hardness of two bodies is more than 20 per cent. Hence, the general assumption made in the model that the weld is rigid and hard and acts as an abrasive might not be satisfied anymore with these ceramic materials.

surpasses the increased sensitivity to abrasion of the system. Therefore, the effect of the high hardness of the ceramics might be nullified by the very limited plastic deformation before fracture of ceramics, as even at small indentation depths it will result in high values of ζ .

Table 6.3: Material properties of four ceramic materials, from Metselaar [76].

		E [GPa]	ν [-]	H [GPa]
Alumina	Al_2O_3	390	0.23	22
Zirconia	ZrO_2	205	0.30	14
Silicon Carbide	SiC	430	0.17	28
Silicon Nitride	Si_3N_4	320	0.24	15

In Table 6.3 some material properties for four types of ceramic materials are shown. These material properties are inserted into the developed model, using the measured micro-geometry of the weld as the abrasive surface. In the calculations it is assumed that pure cutting occurs at any degree of penetration, so $\zeta = 1$. The calculated specific wear rates are scaled with respect to the wear rate for nodular cast iron, in which it is assumed as well that $\zeta = 1$. These relative specific wear rates are presented in Fig. 6.12.

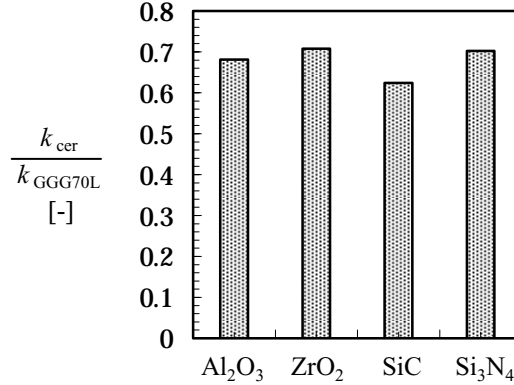


Fig. 6.12: Calculated relative specific abrasive wear rates for four ceramic materials.

It can be seen that the application of ceramic tool materials can cause a reduction of the specific wear rate up to 40%. Furthermore, the obtained ranking, with SiC having the highest resistance to abrasive wear, followed by Al_2O_3 , Si_3N_4 and ZrO_2 , agrees with the experimental ranking of Kataoka et al. [60] which is based on the surface roughness of the formed products.

6.3.2.2 Coatings on the tool

The effect of the application of a hard protective layer on a substrate was already discussed in Chapter 5. In Chapter 4 it was observed that in single asperity scratching at an equal degree of penetration, generally the abrasive wear of a coating increases with its hardness.

The load carried by a single asperity at a given degree of penetration depends on its hardness. Therefore, in terms of the specific wear rate k , applying a hard protective coating only makes sense if the increase in system hardness surpasses the decrease in resistance to abrasion of the system. An example was shown in Fig. 5.26, where it was illustrated that in that situation, adding a stellite 6 layer to nodular cast iron is beneficial for the wear behaviour, while the application of an additional layer of chromium nitride is not.

6.4 Discussion

Abrasive wear depends on a complex combination of geometry, hardness, micro-geometry, and sensitivity to abrasive wear of the bodies in contact. These parameters need to be balanced in the right way to minimise the amount of abrasive wear.

This chapter focussed on the abrasive wear of the tool in the deep drawing of tailor welded blanks. Experimental results obtained using the deep drawing simulator were presented for the tool material, with a range of applied coatings.

The titanium nitride and the chrome plated surfaces, as well as the cobalt based clad layers show improved wear resistance. The experimental results obtained for the metal-carbon coated surface are somewhat disappointing when compared to the results reported in literature, where results show generally that the application of metal-carbon layers is quite beneficial to wear prevention in metal forming processes (see for instance Murakawa, Koga, Watanabe and Takeuchi [80], van der Heide and Schipper [110] and de Rooij [26]). However, in all these cases the tool is made of tool steel, onto which the metal-carbon layer adheres well, while it was shown in Chapter 4 that the bond between the metal-carbon layer and the nodular cast iron substrate is not very good.

The experimental conditions were applied as input in the developed model for two of the tested surfaces. The obtained wear rates from the model and the experiments have similar values, although more single asperity scratch data for other coating - substrate combinations are needed in order to validate the developed model.

Subsequently, the developed model is applied for a wear analysis of the deep drawing process. Using a simplified model of the surface micro-geometry of the weld, the influence of the welding velocity on the wear behaviour of the tool - tailor welded blank system is studied. From this analysis it appears that the welds on the tailor welded blanks that are applied in this research have the most abrasive micro-geometry. Hence a potentially significant decrease in specific wear rate in the contact between tool and tailor welded blank can be obtained by adjusting the welding parameters.

Another possibility to decrease the wear in the system is by changing mechanical properties of the surface of the forming tool. This can be done by either changing the material of the tool or by applying a protective coating. The developed model is applied to perform some indicative calculations on two alternative tool materials as well as on some hard coatings. It appears that by applying hardened tool steel as the material for metal forming tools, the wear rate can be reduced significantly. For ceramic tool materials no degree of wear data is currently available, and hence the $\zeta - D_p$ relation needs to be guessed. The relative specific wear rate for these ceramic materials shows an increase in wear resistance up to 40%. Besides that, the application of ceramic tools might enable the use of environmentally friendly water based lubricants.

Chapter 7

Conclusion

7.1 Introduction

In this thesis a model is developed that describes the contact behaviour and the associated abrasive wear in metal forming processes. The contact situation under consideration is that of a (due to welding) relatively hard work piece sliding against a softer forming tool. In this final chapter the conclusions of this research as well as some recommendations for further research are presented.

7.2 Overview of the developed model

A schematic overview of the developed model applied to deep drawing of tailor welded blanks is shown in Fig. 7.1. The model is composed of a *contact model*, numbered ②, ③ and ④, and an *abrasive wear model* (⑤ & ⑥). First, the micro-geometry of the two surfaces is measured and inserted in the contact model. In the figure, the bottom surface represents the softer tool, while the upper surface shows the micro-geometry of the tailor welded blank. Secondly, the surfaces are brought into contact and a load N is applied. In the third step, the contact spots are determined. Fourth, the micro-geometry of these spots is represented by paraboloids. Each paraboloid indents a certain amount into the tool surface. This indentation depth is normalised with respect to the asperity size, resulting in the relative indentation depth or degree of penetration $D_{p,i}$. This degree of penetration is the input for the abrasive wear model, which describes the relation between the degree of penetration and the 'abrasiveness' ξ_i of each asperity. From this relation, as plotted in the graph,

fifthly, the abrasive wear caused in each individual micro-contact is obtained and finally the summation over all micro-contacts gives the total abrasive wear volume, represented by the worn surface shown bottom-left in Fig. 7.1.

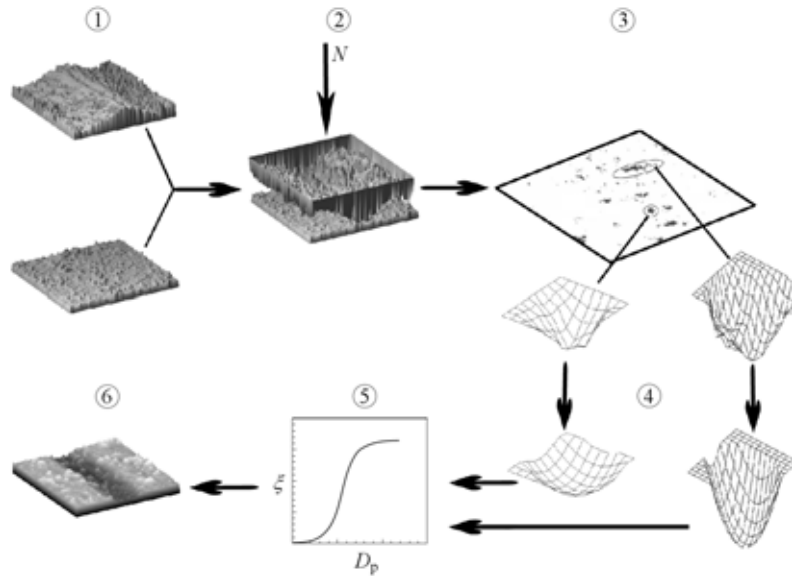


Fig. 7.1: Schematic overview of the developed model.

7.3 Conclusions

Single asperity contact

Chapter 3 focused on a model for the contact behaviour of a single rigid sliding asperity in contact with a deforming layered flat body. Two basic shapes of asperities are studied: elliptic cones and elliptic paraboloids. For conically shaped indenters, the deformation regime depends on the geometry of the indenter. For paraboloidal shaped asperities, at small values of the indentation depth of the asperity into the deforming body, the body deforms purely elastic. After a critical indentation depth yield occurs, and the deformation regime is a combination of elastic and plastic behaviour. Eventually the fully plastic deformation regime is reached. In the studied situation, the pure elastic deformation is only of minor importance, making the elastoplastic and fully plastic regimes decisive.

The contact behaviour, i.e. the relation between carried load and indentation depth, depends strongly on the dimensions of the asperity. However, the ellipticity of an asperity only has a minor effect on the modelled contact

behaviour. Surface layers on the deforming body may affect the contact behaviour. For very small indentation depths the contact behaviour depends solely on the properties of the layer. With increasing indentation depth the influence of the substrate material increases and the behaviour of the layered surface is described by a combination of the layers and the substrate.

Single asperity wear

The abrasive wear behaviour of single asperities is discussed extensively in Chapter 4. In the first section of this chapter a theoretical model for the abrasive wear of a surface resulting from the sliding contact with a single rigid asperity is discussed. The sliding and scratching action of the asperity causes a wear scar in the surface. This wear scar is composed of a groove, flanked on both sides by a shoulder. It is assumed that the material that originally was located in the groove is either transferred to the shoulders or removed as wear debris.

The proportion of the amount of transferred material to the amount of wear debris increases with increasing relative indentation depth of the scratching asperity. Furthermore, this ratio, commonly known as the degree of wear, depends on a large number of factors, including the surrounding environment, lubricants and both surface properties and bulk properties of the materials.

To determine the degree of wear of the systems under consideration, single asperity scratch tests were performed on a series of coated nodular cast iron specimens. These experiments and the obtained results are discussed in the second part of Chapter 4. The relation between the degree of penetration of an asperity and the resulting degree of wear of the surface follows an S-shaped path that can be described by a *tanh*-function. This empirical relation for the sensitivity to abrasion of a surface forms the basis of the developed wear model for rough surfaces. Other observations from the single asperity experiments are that many commonly applied hard coatings show unsatisfactory adherence to the nodular cast iron substrate, even at very low loads and indentation depths. Typical coating failure mechanisms that were observed include cracking, flaking and delamination.

In the final section of chapter 4, the developed wear model including the empirical degree of wear relation is implemented and the model is used to analyse the effects of several parameters of the model. The volumetric abrasive wear is very sensitive to the applied load as well as to the dimensions of the scratching asperity, such as the radius and the ellipticity. The results also show that a hard protective surface layer might not always reduce the abrasive wear of a single asperity contact.

Contact between rough surfaces

The developed model for the contact and wear behaviour of a single asperity and a deforming flat is extended to rough surfaces in Chapter 5. From the measured surface micro-geometry and the mean plane separation of the two surfaces, the micro-contacts are obtained. Through each micro-contact a simple geometrical shape is fitted, enabling the use of the developed single asperity model for both the contact and wear behaviour of rough surfaces.

The developed model is studied by applying it to a series of sample-surfaces. In case conical shaped asperities are applied, the calculated attack angles generally are smaller than 15° . In the case of paraboloidal shaped asperities, the calculated radius can range over four orders of magnitude, from tenths of a micrometer to several hundred micrometers.

Initially, at a large separation between the surfaces, real contact occurs at a limited number of micro-contacts. At such a large separation, the indentation depth of the asperities into the counter surface is small and the dominant deformation mode is elastic. When the surfaces approach each other more closely, these initial micro-contacts penetrate deeper into the surface, causing elastoplastic and eventually fully plastic deformation. Also the number of micro-contacts grows. With even more decreasing mean plane separation of the two surfaces, the increase of the number of micro-contacts is slowed down because several adjacent micro-contacts merge. The model indicates that these large scale micro-contacts deform elastically again. Although this behaviour of increasing elasticity with increasing indentation depth might seem counter-intuitive, these results are confirmed in literature.

The abrasive wear in the contact of rough surfaces is a summation of the wear volumes of all individual asperities. Generally, only a fraction of the contacting asperities on a surface significantly contribute to the wear volume.

The specific abrasive wear rate in a contact is influenced strongly by both roughness and anisotropy of the micro-geometry of the abrading surface. Furthermore, the model confirms the Archard wear law.

The model shows that the specific wear rate might decrease when a hard surface layer is applied. Whether this happens depends on the hardness of the layered surface, the thickness of the layer as well as on the sensitivity to abrasion of the layer. In Chapter 4 it was seen that, generally, at equal indentation depth, hard coatings show an increased degree of wear, which diminishes the effects of the increase in hardness on the wear resistance.

Abrasive wear in deep drawing of tailor welded blanks

In Chapter 6 the developed model for abrasive wear between rough surfaces is applied to the contact between a hard and rough tailor welded blank in contact with a softer forming tool. First, some results of laboratory scale deep drawing experiments are presented. An important observation from these experiments is that the application of a hard surface layer on the tool can have a considerable effect on the specific wear rate, but only if the coating adheres well to the nodular cast iron surface, as was also found in the single asperity experiments.

Secondly, the experiments are analysed with the developed model. A comparison of the experimental and calculated results indicates that the developed model is capable of quantitatively describing the abrasive wear of the forming tool.

Finally, the wear model is applied to investigate the influence of the geometry of the weld and the influence of the tool materials. The weld is simplified by assuming that it is composed of a succession of V-shaped ridges. The results indicate that the specific wear rate in the contact can be reduced significantly by changing the micro-geometry of the weld, which can be done by adjusting the welding parameters. Besides that, some alternative tool materials are studied. It can be seen that, from an abrasive wear point of view, hardened tool steels and ceramics provide an interesting alternative to nodular cast iron. Protecting the tool surface with a hard surface layer can decrease the specific wear rate, but generally hard coatings tend to show a higher degree of wear at constant indentation depth. Therefore, the wear rate only decreases if the increased sensitivity to abrasion of the layer is outdone by the increase in load bearing capacity due to the increased hardness.

7.4 Recommendations

Static single asperity contact

- The static contact between a single paraboloidal shaped asperity and a deforming flat is described using three deformation regimes: elastic, elastoplastic and fully plastic. The transitional elastoplastic regime ranges from $d = d_{e,trans}$ to $d = d_{p,trans} = S_{ep} \cdot d_{e,trans}$. In this thesis a theoretical value of S_{ep} between 60 and 80 is derived, depending on the aspect ratio of the asperity. This theoretical work is confirmed by experimental results of Jamari [54], who found a value $S_{ep} = 80$ for spherically shaped asperities. However, for non-spherically shaped asperities the value of S_{ep} needs to be validated.

Sliding single asperity contact

- In single asperity sliding, the contact behaviour will depend on the wear behaviour, i.e. the forces arising in a scratching contact will be different from that in a sliding contact. Presently, this effect of scratching is neglected. More research is needed on this wear - contact relation, after which it can be included in the model.

Single asperity wear

- To enable the in-situ visual observation of the wear processes in sliding single asperity contact, the scratch tests were performed in the high vacuum environment of the chamber of a scanning electron microscope. However, the contact and wear behaviour are affected by the environment and hence the accuracy of the model might be improved by determining the $D_p - \zeta$ relation under atmospheric conditions. This can be done using a scratch tester or the single asperity micro-tribometer which is currently being developed at the laboratory for Surface Technology and Tribology [16], [94].
- Presently, for each set of materials, surface layers, environmental properties and lubrication conditions, the relation between $D_p - \zeta$ needs to be determined experimentally. When this relation can be obtained fast and accurately without the use of experiments, for instance using numerical simulations, the developed model provides a powerful tool for the calculation of the abrasive wear resistance of tribological systems.
- Nodular cast iron appear to be a 'difficult' substrate material for thin hard coatings. This was shown for instance in the experiments in Chapter 4, where the metal-carbon layer delaminated even at very low indentation depths. The adherence of coatings might be improved by applying an intermediate layer between substrate and coating. Other possibilities to improve the performance of the coated surface are increasing the coating thickness and the application of multi-layered coatings.

Contact between rough surfaces

- The developed deterministic contact model enables the investigation of the behaviour of rough surfaces in contact without some of the restrictions associated to conventional contact models. This makes the contact model also of interest in mixed and boundary lubricated contacts, for example in the study of ball bearings, engines and transmissions.

Abrasive wear in deep drawing of tailor welded blanks

- The experimentally obtained results in laboratory scale deep drawing correspond with the calculated wear rates. However, more single asperity scratch data for other coating - substrate combinations are needed in order to fully validate the developed model.
- The model indicates that the micro-geometry of the weld on a tailor welded blank can affect the abrasive wear in the tool - tailor welded blank. Furthermore, of the weld geometries analysed, the welds applied in the experiments are shown to have the most abrasive micro-geometry. This observation opens perspectives for the optimisation of the abrasive wear behaviour of the forming tool by adjusting the tailor welded blanks.
- The ultimate objective of this research project is the application of the developed model for process optimisation in industrial deep drawing. Hence validation of the model on a typical deep drawing product in a field test is highly recommended.

Abrasive wear in metal forming processes

The application of the developed model is not restricted to the deep drawing of tailor welded blanks. As indicated in Chapter 1, abrasive wear of the forming tool occurs in many other metal forming processes. Examples include other sheet metal forming processes, like hydroforming, spinning and stretch forming. Furthermore, abrasive wear plays an important role in many other situations, ranging from metal forming processes, such as the extrusion of aluminium and magnesium alloys, where lumps that adhere to the tool surface cause scratches in the product, to attrition and abrasion in dentistry, where teeth wear because of the contact with other teeth and with foreign materials, respectively. The abrasive wear in these applications can also be analysed using the developed model.

Acknowledgements

This thesis is written to conclude a four and a half year period as a researcher at the laboratory of Surface Technology and Tribology at the University of Twente. In this work, research done within the framework of the IOP-OT project 99005 "Slijtvaste Coatings voor het Omvormen van Tailored Blanks met Gietijzeren Gereedschappen" is described.

The atmosphere in our research group was very pleasant. The occasional activities like skiing in Winterberg and 'because-of-the-nice-weather'-barbecues were always fun. For this I would like to thank all colleagues and former colleagues: Ako, Andre, Belinda, Benoit, Bernd, Bert, Caner, Daniël, Dik, Ellen, Elmer, Emile, Erik, George, Harm, Henk, Irinel, Isaias, Jamari, Jan-Willem, John, Kees, Laurens, Loredana, Luis, Mark, Matthijn, Qiang, Rihard, Walter, Willie and Wijtze. Special thanks go to my roommate Jan-Willem Sloetjes, for providing a nice working environment as well as for his excellent choice of music.

This project was carried out in cooperation with TNO Industrie in Eindhoven. Thanks go to Bert Huis in 't Veld and Emile van der Heide of TNO for their assistance, as well as to all people associated to IOP-OT who showed interest in this research and who provided valuable input and an industrial boundary to the problem under consideration.

The experimental work on single asperity wear, presented in Chapter 4, was done during a three month visit to professor Kato's Tribology laboratory at Tohoku University in Sendai, Japan. Professor Koji Kato, professor Koshi Adachi, Wang Xiaolei, Boyko Stoimenov and Ulrika Pettersson are thanked for their experimental assistance and many useful discussions.

During the past four and a half years I spent most of my time on the research discussed in this thesis. However, working at the university also includes other interesting aspects. The supervision over MSc students, being a tutor for first-year students and other educational tasks enabled me to practice my teaching skills and to broaden my view. Particularly, I would like to thank the students of the Sari Asia committee, who organised a fantastic trip to Indonesia, Singapore and Malaysia last December. The extensive preparations were very interesting and the study tour itself provided a welcome break in the process of writing this thesis.

Furthermore, my friends and family are thanked for their ongoing support and their interest in my work. Their patience and acceptance were vital to the realisation of this work.

Finally I would like to thank my father, who introduced me into the world of physics and engineering, for his constant enthusiasm regarding my activities, his advise and support and for being my best friend.

Marc

Appendix A

Material properties

A.1 Tool material

Table A.1: Properties of the tool material.

Name according to DIN EN 1563 [32]: EN-GJS-700-2

Typical composition in mass%

C	Si	Mn	P	S	Cu	Mg	Mo	Ni
3.3- 3.6	1.8- 2.4	0.30- 0.60	<0.05	<0.02	0.80- 1.20	0.04- 0.07	0.40- 0.60	0.90- 1.20

Mechanical properties

Young's modulus	E	[GPa]	176
Poisson's ratio	ν	[-]	0.275
Ultimate stress	σ_u	[MPa]	700
Yield strength	σ_y	[MPa]	420
Hardness	H	[GPa]	3.35
Density	ρ	[kg·m ⁻³]	7.2

A.2 Coatings

Table A.2: Properties of the applied coatings.

Name	Young's Modulus [GPa]	Poisson's ratio [-]	Hardness [GPa]	Thickness [μm]
Titanium Nitride	600	0.25	28	3.2
Metal-Carbon	100	0.30	10	4
Chromium Nitride	180	0.30	17	4
Hard chromium	210	0.30	10	15
Stellite 6	209	0.31	4	10^3
Ultimet	209	0.31	3	10^3

A.3 Sheet

A.3.1 Sheet material

Table A.3: Properties of the sheet material.

Name according to DIN EN 10130 [31]: DC05

Typical composition in mass%

C	P	S	Mn	Ti
0.06	0.025	0.025	0.35	-

Young's modulus	E	[GPa]	210
Poisson's ratio	ν	[-]	0.30
Ultimate stress	σ_u	[MPa]	300
Yield strength	σ_y	[MPa]	180
Brinell Hardness	H	[HB]	80
Hardness	H	[GPa]	0.82*
Density	ρ	[$\text{kg}\cdot\text{m}^{-3}$]	7.9

*: approximate value; converted from Brinell hardness

A.3.2 Weld

In an ideal weld there is no clear boundary between the weld material and the sheet. However, a small amount of undercut or excess weld metal is allowed. Table A.4 lists the limits for undercut and excess weld metal for the three quality levels that are defined in EN ISO 13919-1:1996 [52].

Table A.4: Limits for weld-undercut according to EN ISO 13919-1:1996 [52].

Imperfection	moderate D	intermediate C	stringent B
Undercut	$h \leq 0.15 \cdot t$ and $h \leq 1\text{mm}$	$h \leq 0.1 \cdot t$ and $h \leq 0.5\text{mm}$	$h \leq 0.05 \cdot t$ and $h \leq 0.5\text{mm}$
Excess weld metal	$h \leq 0.20\text{mm} + 0.3 \cdot t$ and $h \leq 5\text{mm}$	$h \leq 0.2\text{mm} + 0.2 \cdot t$ and $h \leq 5\text{mm}$	$h \leq 0.2\text{mm} + 0.15 \cdot t$ and $h \leq 0.5\text{mm}$

The applied sheet material has a thickness $t = 0.8$ mm, giving for the level B limit for the undercut $h \leq 0.04$ mm and for the excess weld metal $h \leq 0.32$ mm

Fig. A.2(a) shows the undercut and (b) the excess weld metal for the welds applied in the experiments of Chapter 6. The undercut is measured to be 0.037 mm and the excess weld metal 0.03 mm. For these imperfection designations the welds fall within the stringent quality level B.

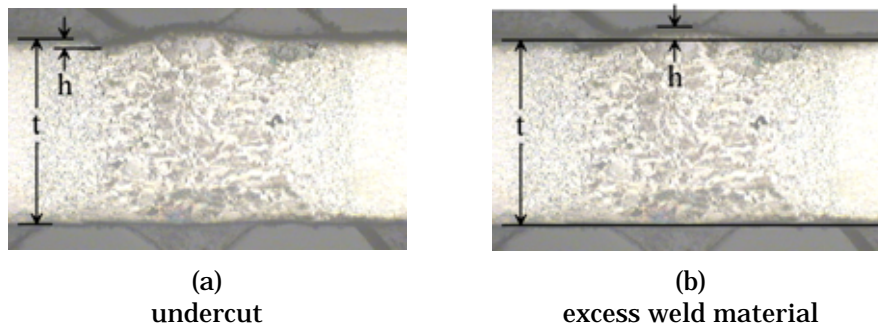


Fig. A.2: Imperfections of welds of the applied tailor welded blanks.

Appendix B

Contact

B.1 Static contact

In this appendix the static contact between a single asperity and a flat is discussed. First the elliptic cone is treated and subsequently the equations for the static contact between a paraboloidal shaped asperity and a flat are presented.

B.1.1 Conical shaped asperity

B.1.1.1 Axisymmetric cone

The elastic contact between a circular cone and a flat is described by Love [70], who gave a solution to the axisymmetric Boussinesq problem. For incompressible materials ($\nu = 0.5$) Johnson [58] found for the maximum shear stress:

$$\tau = \frac{1}{2} \cdot E_* \cdot \tan^{-1} \left(\frac{\theta}{2} \right) \quad (\text{B.1})$$

with θ the asperity top angle. According to both the Tresca and Von Mises yield criteria, plastic deformation occurs when the shear stress $\tau \geq 0.5 \cdot Y$, which gives for the limiting top angle:

$$\theta_c = 2 \cdot \operatorname{atan} \left(\frac{E_*}{Y} \right) \quad (\text{B.2})$$

Plastic deformation will occur when the conical asperity has a top angle smaller than this critical value. As a rule of thumb, for metals the elastic limit is reached at a strain $\varepsilon = Y/E = 0.2\%$ and consequently elastic deformation only occurs for conical asperities that are very blunt, i.e. have a top-angle that approaches 180° .

For compressible materials ($\nu < 0.5$), the situation is more complex. In that case, however, the elastic limit is reached at even lower values of the shear stress. Therefore it seems reasonable to neglect the linear elastic deformation regime for contacts with a conical shaped asperity.

Based on truncation of the contacting cap the plastic contact area for the contact between a flat and a cone with top-angle θ is given by eq. (B.3).

$$A_p = \pi \cdot \tan^2 \left(\frac{\theta}{2} \right) \cdot d^2 \quad (\text{B.3})$$

and the plastic contact load is obtained by multiplying the contact area of eq. (B.3) with the hardness H of the deforming material:

$$N_p = \pi \cdot \tan^2 \left(\frac{\theta}{2} \right) \cdot H \cdot d^2 \quad (\text{B.4})$$

In case of the contact between a rigid indenter and a deforming base material, a more realistic image than this rigid-perfectly-plastic representation can be obtained assuming that the contact consists of a plastic core which is surrounded by a shell where the material deforms elastically. This elastic-plastic behaviour can be modelled using the so-called cavity model (see Johnson [58]), as illustrated in Fig. B.1, in which the core is supposed to be a spherical cavity that expands due to internal pressure. This core is enclosed by a region where the material deforms plastically, which subsequently is surrounded by an elastic region.

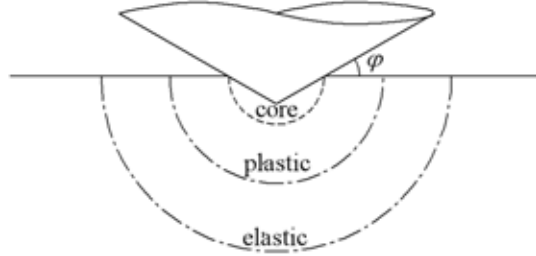


Fig. B.1: Cavity model of elastic-plastic indentation by a cone, taken from Johnson [58].

In this situation, the hydrostatic pressure in the core is given by eq. (B.5).

$$p_0 = \frac{2}{3} \cdot Y \cdot \left\{ 1 + \ln \left(\frac{\frac{E}{Y} \cdot \tan(\varphi) + 4 \cdot (1 - 2 \cdot \nu)}{6 \cdot (1 - \nu)} \right) \right\} \quad (\text{B.5})$$

By taking $H = 3 \cdot Y$ this relation changes to:

$$p_0 = \frac{2}{9} \cdot H \cdot \left\{ 1 + \ln \left(\frac{\frac{3 \cdot E}{H} \cdot \tan(\varphi) + 4 \cdot (1 - 2 \cdot \nu)}{6 \cdot (1 - \nu)} \right) \right\} \quad (\text{B.6})$$

The contact pressure as defined in eq. (B.6) can be normalised with respect to the hardness of the deforming material. The resulting relation between the normalised hydrostatic pressure in the core and the attack angle of the asperity is plotted in Fig. B.2 for several values of the Poisson's ratio of the material. It can be seen that the contact pressure is rather insensitive to the Poisson's ratio, in particular at the minimum and maximum values of the asperity attack angle. The bold line represents the grey cast iron tool material.

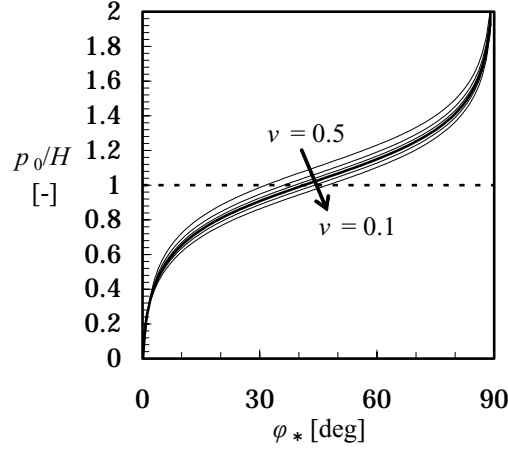


Fig. B.2: Normalised pressure as a function of the asperity attack angle.

The elastic-plastic contact load is obtained by multiplying the contact area with the average contact pressure of eq. (B.6). The elastic-plastic contact area is assumed to equal the plastic contact area, and hence can be approximated by truncation of the contacting cap. This gives in terms of the asperity attack angle φ :

$$A_{\text{ep}} = \pi \cdot \left(\frac{d}{\tan(\varphi)} \right)^2 \quad (\text{B.7})$$

and for the contact load:

$$N_{\text{ep}} = \frac{2 \cdot \pi}{9} \cdot \frac{H}{\tan^2(\varphi)} \cdot \left\{ 1 + \ln \left(\frac{\frac{3 \cdot E}{H} \cdot \tan(\varphi) + 4 \cdot (1 - 2 \cdot \nu)}{6 \cdot (1 - \nu)} \right) \right\} \cdot d^2 \quad (\text{B.8})$$

B.1.1.2 Cone with an elliptic cross-section

For a (non-axi-symmetric) Vickers hardness indenter, Johnson suggests an energy-equivalent approximation using a representative cone that displaces the equal amount of volume. For a Vickers indenter which has the shape of a square based pyramid with a 136° angle between the faces, he applies a representative cone with a top-angle of 140.6° .

Following the same procedure for an elliptic cone with top-angles θ_x and θ_y and attack angles $\varphi_{x,y} = \frac{1}{2} \cdot (\pi - \theta_{x,y})$ results in a representative cone with attack angle:

$$\varphi_* = \text{atan} \left\{ \sqrt{\tan(\varphi_x) \cdot \tan(\varphi_y)} \right\} \quad (\text{B.9})$$

Consequently, the equations for the contact area A and contact load N in the elastoplastic and fully plastic deformation modes are given by:

$$A_{\text{ep}} = A_{\text{p}} = \pi \cdot \left(\frac{d}{\tan(\varphi_*)} \right)^2 \quad (\text{B.10})$$

$$N_{\text{ep}} = \frac{2 \cdot \pi}{9} \cdot \frac{H}{\tan^2(\varphi_*)} \cdot \left\{ 1 + \ln \left(\frac{\frac{3 \cdot E}{H} \cdot \tan(\varphi_*) + 4 \cdot (1 - 2 \cdot \nu)}{6 \cdot (1 - \nu)} \right) \right\} \cdot d^2 \quad (\text{B.11})$$

$$N_{\text{p}} = \pi \cdot H \cdot \left(\frac{d}{\tan(\varphi_*)} \right)^2 \quad (\text{B.12})$$

B.1.2.3 Transitions

As stated before, pure elastic deformation only occurs when the asperity is extremely blunt and therefore, for conical asperities, this deformation mode can be neglected. In the fully plastic deformation mode the contact pressure equals the hardness of the deforming material. In the elastoplastic regime the contact pressure in the core is a function of the material properties and the geometry of the indenting asperity, as shown in eq. (B.6) and Fig. B.2.

When it is assumed that the transition from elastoplastic to fully plastic deformation occurs when the pressure equals the hardness of the deforming material, i.e. the normalised pressure equals 1. Substituting this into eq. (B.6) and solving for the attack angle φ gives:

$$\varphi_* = \text{atan} \left[\frac{H}{3 \cdot E} \cdot \left(6 \cdot (1 - \nu) \cdot e^{\frac{7}{2}} - 4 \cdot (1 - 2 \cdot \nu) \right) \right] \quad (\text{B.13})$$

In Fig. B.2 this relation was plotted as a function of the Poisson's ratio ν for $E = 178$ GPa and $H = 3300$ MPa. Relatively blunt asperities operate in the elastoplastic regime while sharp asperities operate in the fully plastic regime. For asperities with an attack angle between about 30° and 60° a transition in deformation mode is observed with changing Poisson's ratio. The bold line in Fig. B.2 represents $\nu = 0.275$ and therefore this curve indicates the hydrostatic contact pressure as a function of the asperity attack angle for a deforming body made of nodular cast iron. The hydrostatic contact pressure exceeds the hardness of the material when the attack angle exceeds 40° , which therefore marks the transition from elastoplastic to fully plastic deformation.

B.1.2 Paraboloidal shaped asperity

B.1.2.1 Axisymmetric paraboloid (sphere)

The elastic contact between a spherical shaped asperity and a flat is described by the equations of Hertz [47]. In this theory the contact between two curved solids is "scaled" to the contact between a sphere and a flat, resulting in relatively simple equations. The contact area and the contact load as a function of the penetration depth d for the contact between a single spherical asperity and a flat are given by eq. (B.14) and eq. (B.15).

$$A_e = \pi \cdot R \cdot d \quad (\text{B.14})$$

$$N_e = \frac{4}{3} \cdot E_* \cdot R^{\frac{1}{2}} \cdot d^{\frac{3}{2}} \quad (\text{B.15})$$

In eq. (B.15) E_* denotes the reduced Young's modulus as defined by eq. (B.16):

$$E_* = \left(\frac{1-\nu_1^2}{E_1} + \frac{1-\nu_2^2}{E_2} \right)^{-1} \quad (\text{B.16})$$

Unlike the contact between a sharp asperity and a flat, where the highest stress occurs at the apex, in the contact between a curved asperity and a flat the maximum shear stress occurs at a depth z below the surface, c.f. Hamilton and Goodman [45], as illustrated in Fig. B.3.

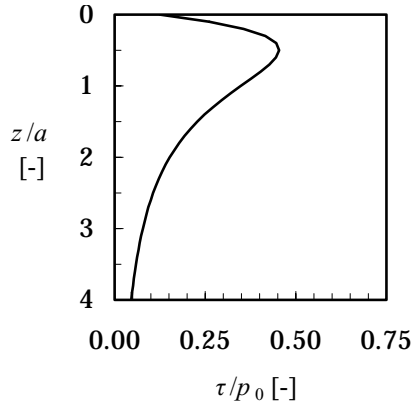


Fig. B.3: Stress distribution under elastic spherical indentation.

With increasing penetration depth of the asperity into the flat, this sub-surface stress exceeds the elastic limit of the flat and a sub-surface plastic core is formed. In this situation the elastic theory of Hertz is not applicable anymore.

When the plastic core extends to the surface, the contact operates in the fully plastic deformation regime, as discussed by Johnson [58]. In this regime, the relations for contact area and load as a function of the asperity penetration are, in their most simple form, based on the truncation of a spherical cap (equations (B.17) and (B.18))

$$A_p = 2 \cdot \pi \cdot R \cdot d \quad (\text{B.17})$$

$$N_p = 2 \cdot \pi \cdot R \cdot H \cdot d \quad (\text{B.18})$$

Next to these relatively simple equations for fully plastic deformation, more complex phenomena can be incorporated. For example Chang, Etsion and Bogy [23] developed a plastic model including volume conservation, resulting in a dilated contact area as shown in Fig. B.4.

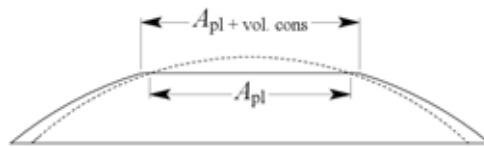


Fig. B.4: Dilation of the contact area due to volume conservation.

However, in the investigated situation of sheet-metal forming it is plausible to neglect this plastic volume conservation as Zhang et al. [119] showed by numerical simulations of a bump on a sheet that with increasing tensile stress in the sheet, the geometry of the bump remains approximately constant.

As stated before, for a spherical asperity the limit of linear elastic deformation is reached when the maximum sub-surface stress surpasses a critical limit and a sub-surface plastic core is formed. However, fully plastic deformation only initiates when the plastic core has extended to the surface of the deforming material. Johnson [58] states that for fully plastic deformation to occur, the load should be about 400 times the load at initial yield. Between the elastic and fully plastic regimes there is an intermediate regime in which with increasing load and penetration depth, the sub-surface core expands until it reaches the surface. The material behaviour in this elastoplastic regime is a combination of elastic and plastic events leading to complex equations for contact area and contact load. However, as the material behaviour at both the begin and at the end of the elastoplastic regime are well defined by the pure elastic and fully plastic regimes, it seems logical to describe the material behaviour in the intermediate elastoplastic regime by applying a rule of mixtures for these two asymptotes. This was done by Zhao and co-workers [118], who suggested describing the contact area in the elastoplastic stage using a third order polynomial template, as illustrated in Fig. B.5, providing a smooth and gradual transition between the elastic and fully plastic contact regimes.

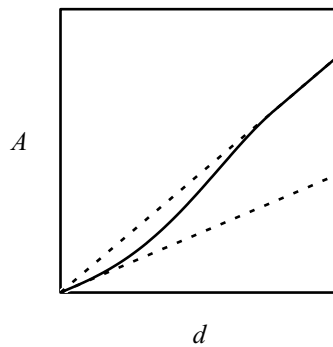


Fig. B.5: Schematic representation of the contact area as a function of the penetration depth for elastic, elastoplastic and fully plastic deformation.

As the elastoplastic regime extends from the onset of plastic deformation at $d_{e,trans}$ to the beginning of fully plastic deformation at $d_{p,trans}$ the relative elastoplastic indentation depth δ can be defined as:

$$\delta = \frac{d - d_{e,trans}}{d_{p,trans} - d_{e,trans}} \quad (\text{B.19})$$

With this, the elastoplastic contact area can be expressed as

$$A_{ep} = A_e + (A_p - A_e) \cdot (-2 \cdot \delta^3 + 3 \cdot \delta^2) \quad (\text{B.20})$$

Based on the work of Francis [37], who suggested a logarithmic relation between the average contact pressure and the indentation depth, Zhao obtained the relation presented in eq. (B.20) for the average contact pressure in the intermediate stage.

$$p_{ep} = H - H \cdot (1 - k) \cdot \frac{\ln d_{p,trans} - \ln d}{\ln d_{p,trans} - \ln d_{e,trans}} \quad (\text{B.21})$$

The contact pressure according to this relation, normalised with respect to the hardness of the material, is plotted in Fig. B.6 as a function of the indentation depth d .

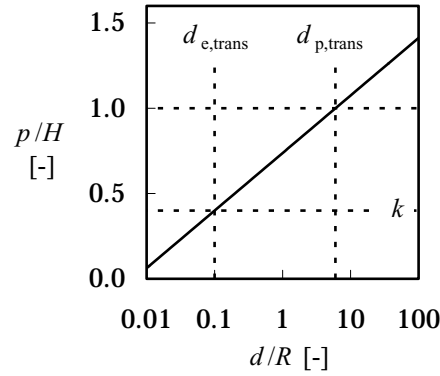


Fig. B.6: Normalised elastoplastic contact pressure.

Multiplying eq. (B.20) and eq. (B.21) results in the following expression for the contact load carried by an asperity-flat contact in the elastoplastic regime:

$$N_{ep} = \left\{ A_e + (A_p - A_e) \cdot (-2 \cdot \delta^3 + 3 \cdot \delta^2) \right\} \times \left[H - H \cdot (1 - k) \cdot \frac{\ln d_{p,trans} - \ln d}{\ln d_{p,trans} - \ln d_{e,trans}} \right] \quad (B.22)$$

B.1.2.2 Transitions

It was shown that with increasing penetration depth of the spherical asperity the contact goes through three deformation regimes. For small penetration depths, the contact is considered to be elastic. With increasing penetration depth some sub-surface plasticity occurs until finally the fully plastic deformation regime is attained. For correct application of the contact model the transitions between these regimes are important.

An expression for the indentation depth in elastic contact for an elliptic contact can be obtained by rearranging eq. (B.15).

$$d_e = \left(\frac{9 \cdot N^2}{E_*^2 \cdot R} \right)^{\frac{1}{3}} \quad (B.23)$$

And by dividing and eq. (B.15) by eq. (B.14) the average elastic contact pressure is obtained:

$$p_0 = \frac{1}{\pi} \cdot \left(\frac{2 \cdot N \cdot E_*^2}{R^2} \right)^{\frac{1}{3}} \quad (B.24)$$

In terms of the average contact pressure the transition from the elastic to the elastoplastic mode occurs when:

$$p_0 = k \cdot H \quad (B.25)$$

with H the hardness of the deforming material and k the average contact pressure factor as introduced by Tabor [98]. A good approximation for most metals is $k = 0.4$.

Inserting eq. (B.24) and eq. (B.25) into eq. (B.23) gives for the indentation depth $d_{e,trans}$ at first yield:

$$d_{e,trans} = \frac{9}{8} \cdot \pi^2 \cdot R \cdot \frac{k^2 \cdot H^2}{E_*^2} \quad (\text{B.26})$$

An alternative expression for the contact load at initial yield (i.e. the transition from elastic to elastoplastic material behaviour) can be obtained by multiplying the elastic contact area of eq. (B.14) and the average contact pressure (eq. (B.25)). According to Johnson [58], the transition to fully plastic deformation occurs when the contact load equals 400 times the load at initial yield. With the expression for the plastic contact load as given in eq. (B.18), this results in:

$$\frac{N_{p,trans}}{N_{e,trans}} = \frac{2 \cdot \pi \cdot R \cdot H \cdot d_{p,trans}}{\pi \cdot R \cdot k \cdot H \cdot d_{e,trans}} = 400 \quad (\text{B.27})$$

or in terms of the penetration depth at the elastoplastic-plastic transition:

$$d_{p,trans} = 200 \cdot k \cdot d_{e,trans} \quad (\text{B.28})$$

By inserting $k = 0.4$ this gives that the elastoplastic regime ranges from $d_{e,trans} \leq d \leq 80 \cdot d_{e,trans}$ and thus the indentation depth at the onset of fully plastic deformation is 80 times the indentation depth at first yield.

B.1.2.3 Paraboloidal shaped asperity

The contact between a paraboloidal shaped asperity is merely a generalisation of the spherical situation. Suppose that the geometrical shape of the asperity can be described by the function $z(x,y)$. The radii in x- and y-direction can now be specified:

$$R_x = \left| \frac{\partial^2 z(x,y)}{\partial x^2} \right|^{-1} \quad (\text{B.29})$$

$$R_y = \left| \frac{\partial^2 z(x,y)}{\partial y^2} \right|^{-1}$$

and the reduced radius R_* of the contact is defined as:

$$R_* = \left(\frac{1}{R_x} + \frac{1}{R_y} \right)^{-1} \quad (\text{B.30})$$

The elastic contact situation can again be described by Hertz' theory, with, for the contact area:

$$A_e = 2 \cdot \pi \cdot R_* \cdot \alpha_x \cdot \alpha_y \cdot \gamma^{-1} \cdot d \quad (\text{B.31})$$

In this α_x , α_y and γ are the dimensionless radii of the contact spot and the dimensionless approach between the two bodies as defined in eq. (B.32), see Reussner [89] and Moes [79]:

$$\begin{aligned} \alpha_x &= \kappa^{\frac{1}{3}} \cdot \left[\frac{2}{\pi} \cdot \mathbf{E}(1 - \kappa^2) \right]^{\frac{1}{3}} \\ \alpha_y &= \kappa^{\frac{2}{3}} \cdot \left[\frac{2}{\pi} \cdot \mathbf{E}(1 - \kappa^2) \right]^{\frac{1}{3}} \\ \gamma &= \kappa^{\frac{2}{3}} \cdot \left[\frac{2}{\pi} \cdot \mathbf{E}(1 - \kappa^2) \right]^{\frac{1}{3}} \cdot \frac{2}{\pi} \cdot \mathbf{K}(1 - \kappa^2) \end{aligned} \quad (\text{B.32})$$

with \mathbf{K} and \mathbf{E} the complete elliptic integrals of the first and second kind according to eq. (B.33) and $\kappa = a_x / a_y$ the ellipticity ratio of the contact area.

$$\begin{aligned} \mathbf{K}(m) &= \int_0^{2\pi} \left(1 - m \cdot \sin^2(\psi) \right)^{\frac{1}{2}} d\psi \\ \mathbf{E}(m) &= \int_0^{2\pi} \left(1 - m \cdot \sin^2(\psi) \right)^{\frac{1}{2}} d\psi \end{aligned} \quad (\text{B.33})$$

An approximate relation (Moes [79]) between κ and the gap curvature ratio $\lambda = R_x / R_y$ is given by eq. (B.34).

$$\kappa \approx \left[1 + \sqrt{\frac{\lambda}{2} \cdot \ln(16 \cdot \lambda)} - \sqrt{\ln(4)} + \ln(\lambda^{-0.16}) \right]^{-1} \quad \text{for } 0 < \lambda \leq 1 \quad (\text{B.34})$$

and the elastic contact load according to Hertz is given by:

$$N_e = \frac{4}{3} \cdot \left(\frac{d}{\gamma} \right)^{\frac{3}{2}} \cdot E_* \cdot \sqrt{2 \cdot R_*} \quad (\text{B.35})$$

For the elastoplastic regime, the equations for contact area and contact load do not change:

$$A_{ep} = A_e + (A_p - A_e) \cdot (-2 \cdot \delta^3 + 3 \cdot \delta^2) \quad (\text{B.36})$$

$$N_{ep} = \left\{ A_e + (A_p - A_e) \cdot (-2 \cdot \delta^3 + 3 \cdot \delta^2) \right\} \times \left[H - H \cdot (1 - k) \cdot \frac{\ln d_{p,trans} - \ln d}{\ln d_{p,trans} - \ln d_{e,trans}} \right] \quad (\text{B.37})$$

For the relations between the contact area and contact load and the penetration depth of the asperity in the fully plastic regime are again based on the truncation of the spherical cap:

$$A_p = 2 \cdot \pi \cdot \sqrt{R_x \cdot R_y} \cdot d \quad (\text{B.38})$$

$$N_p = 2 \cdot \pi \cdot \sqrt{R_x \cdot R_y} \cdot H \cdot d \quad (\text{B.39})$$

B.1.2.4 Transitions

For paraboloidal shaped asperities, the procedure to derive the transitions between these elastic, elastoplastic and plastic regimes remains the same. The indentation depth $d_{e,trans}$ at first yield is given by:

$$d_{e,trans} = \frac{9}{8} \cdot \pi^2 \cdot \alpha_x^2 \cdot \alpha_y^2 \cdot \gamma \cdot R_* \cdot \frac{k^2 \cdot H^2}{E_*^2} \quad (\text{B.40})$$

And using Johnson's criterion for fully plastic deformation:

$$\frac{N_{p,trans}}{N_{e,trans}} = \frac{2 \cdot \pi \cdot \sqrt{R_x \cdot R_y} \cdot H \cdot d_{p,trans}}{2 \cdot \pi \cdot R_* \cdot \alpha_x \cdot \alpha_y \cdot \gamma^{-1} \cdot k \cdot H \cdot d_{e,trans}} = 400 \quad (\text{B.41})$$

the elastoplastic to plastic transitional depth $d_{p,trans}$ is obtained:

$$d_{p,trans} = 400 \cdot k \cdot \frac{\sqrt{\lambda}}{1 + \lambda} \cdot \frac{\mathbf{E}(1 - \kappa^2)}{\kappa \cdot \mathbf{K}(1 - \kappa^2)} \cdot d_{e,trans} \quad (\text{B.42})$$

The relative size of the elastoplastic regime S_{ep} is the quotient of $d_{e,trans}$ and $d_{p,trans}$ as expressed in eq. (B.43). Fig. B.7 shows S_{ep} as a function of the ellipticity ratio λ of the contact area. For a circular contact ($\lambda = 1$, $\kappa = 1$, $\mathbf{E} = \mathbf{K} = \pi/2$) the result of eq. (B.28) recurs.

$$S_{ep} = \frac{d_{p,trans}}{d_{e,trans}} = 400 \cdot k \cdot \frac{\sqrt{\lambda}}{1 + \lambda} \cdot \frac{\mathbf{E}(1 - \kappa^2)}{\kappa \cdot \mathbf{K}(1 - \kappa^2)} \quad (\text{B.43})$$

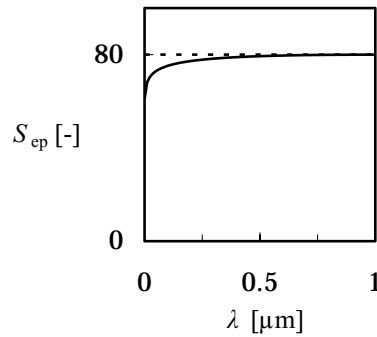
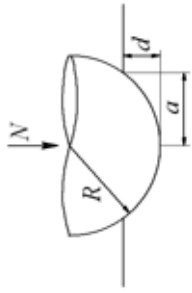
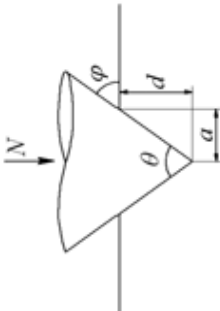


Fig. B.7: Relative size of the elastoplastic area as a function of the indenter ellipticity.

B.1.3 Summary of static contact

Table B.5: Summary of equations for the static contact situation.

		
elastic		$A_e = 2 \cdot \pi \cdot R_* \cdot \alpha_x \cdot \alpha_y \cdot \gamma^{-1} \cdot d$ $N_e = \frac{4}{3} \left(\frac{d}{\gamma} \right)^{\frac{3}{2}} \cdot E_* \cdot \sqrt{2 \cdot R_*}$ $d_{e,trans} = \frac{9}{8} \cdot \pi^2 \cdot \alpha_x^2 \cdot \alpha_y^2 \cdot \gamma \cdot R_* \cdot \frac{k^2 \cdot H^2}{E_*}$ $A_{ep} = A_e + (A_p - A_e) \cdot (-2 \cdot \delta^3 + 3 \cdot \delta^2)$ $N_{ep} = \left\{ A_e + (A_p - A_e) \cdot (-2 \cdot \delta^3 + 3 \cdot \delta^2) \right\} \times \left[\frac{H - H \cdot (1 - k)}{\ln d_{p,trans} - \ln d_{e,trans}} \right]$ $d_{p,trans} = 400 \cdot k \cdot \frac{\sqrt{\lambda}}{1 + \lambda} \cdot \frac{\mathbf{E}(1 - \kappa^2)}{\kappa \cdot \mathbf{K}(1 - \kappa^2)} \cdot d_{e,trans}$ $A_p = 2 \cdot \pi \cdot \sqrt{R_x \cdot R_y} \cdot d$ $N_p = A_p \cdot H$
transition	n.a.	n.a.
elastoplastic	$A_{ep} = \pi \cdot \left(d \cdot \tan^{-1}(\varphi_*) \right)^2$ $N_{ep} = \frac{2 \cdot \pi \cdot H}{9 \cdot \tan^2(\varphi_*)} \cdot \left\{ 1 + \ln \left(\frac{3 \cdot E}{H} \cdot \tan(\varphi_*) + 4 \cdot (1 - 2 \cdot \nu) \right) \right\} \cdot d^2$	$\varphi_{p,trans} = \text{atan} \left\{ \frac{H}{3 \cdot E_*} \cdot \left(6 \cdot (1 - \nu) \cdot e^2 - 4 \cdot (1 - 2 \cdot \nu) \right) \right\}$ $A_p = \pi \cdot \left[d \cdot \tan^{-1}(\varphi_*) \right]^2$ $N_p = A_p \cdot H$
transition		
fully plastic		

B.2 Explicit equations for sliding contact

B.2.1 Sub-surface stresses

In sliding contact the stress distribution in the contact changes because the coefficient of friction between the two bodies adds a tangential component. It is assumed that the normal and tangential components do not interfere. Strictly taken, this is only possible for the contact between two identical bodies, however, Johnson [58] shows that this effect can be neglected, even for two highly dissimilar bodies.

Hamilton [43] (see also the erratum [44] and the discussion by Alfredsson and Cadario [2]) presented explicit equations for the stresses beneath a sliding spherical contact. These equations are reproduced below. In these equations the following grouped parameters are used:

$$r^2 = x^2 + y^2 \quad (\text{B.44})$$

$$A = r^2 + z^2 - a^2 \quad (\text{B.45})$$

$$S = \sqrt{A^2 + 4 \cdot a^2 \cdot z^2} \quad (\text{B.46})$$

$$M = \sqrt{\frac{S+A}{2}} \quad (\text{B.47})$$

$$N = \sqrt{\frac{S-A}{2}} \quad (\text{B.48})$$

$$\phi = \text{atan}\left(\frac{a}{M}\right) \quad (\text{B.49})$$

$$G = M^2 - N^2 + z \cdot M - a \cdot N \quad (\text{B.50})$$

$$H = 2 \cdot M \cdot N + a \cdot M + z \cdot N \quad (\text{B.51})$$

B.2.1.1 Stresses due to the normal load

When $r > 0$:

$$\begin{aligned} \sigma_{x,n} = & \frac{3 \cdot P}{2 \cdot \pi \cdot a^3} \cdot \left[(1+\nu) \cdot z \cdot \phi + \frac{1}{r^2} \cdot \left\{ \frac{y^2 - x^2}{r^2} \right. \right. \\ & \times \left[(1-\nu) \cdot N \cdot z^2 - \frac{1-2 \cdot \nu}{3} \cdot (N \cdot S + 2 \cdot A \cdot N + a^3) - \nu \cdot M \cdot z \cdot a \right] \\ & \left. \left. - N \cdot \left(x^2 + 2 \cdot \nu \cdot y^2 \right) - \frac{M \cdot x^2 \cdot z \cdot a}{S} \right\} \right] \end{aligned} \quad (\text{B.52})$$

$$\begin{aligned} \sigma_{y,n} = & \frac{3 \cdot P}{2 \cdot \pi \cdot a^3} \cdot \left[(1+\nu) \cdot z \cdot \phi + \frac{1}{r^2} \cdot \left\{ \frac{x^2 - y^2}{r^2} \right. \right. \\ & \times \left[(1-\nu) \cdot N \cdot z^2 - \frac{1-2 \cdot \nu}{3} \cdot (N \cdot S + 2 \cdot A \cdot N + a^3) - \nu \cdot M \cdot z \cdot a \right] \\ & \left. \left. - N \cdot \left(y^2 + 2 \cdot \nu \cdot x^2 \right) - \frac{M \cdot y^2 \cdot z \cdot a}{S} \right\} \right] \end{aligned} \quad (\text{B.53})$$

$$\sigma_{z,n} = \frac{3 \cdot P}{2 \cdot \pi \cdot a^3} \cdot \left[-N + \frac{a \cdot z \cdot M}{S} \right] \quad (\text{B.54})$$

$$\begin{aligned} \tau_{xy,n} = & \frac{3 \cdot P}{2 \cdot \pi \cdot a^3} \cdot \left[\frac{x \cdot y \cdot (1-2 \cdot \nu)}{r^4} \cdot \left\{ -N \cdot r^2 + \frac{2}{3} \cdot N \cdot (S + 2 \cdot A) \right. \right. \\ & \left. \left. - z \cdot (z \cdot N + a \cdot M) + \frac{2}{3} \cdot a^3 \right\} + \frac{x \cdot y \cdot z}{r^4} \cdot \left\{ -\frac{a \cdot M \cdot r^2}{S} - z \cdot N + a \cdot M \right\} \right] \end{aligned} \quad (\text{B.55})$$

$$\tau_{yz,n} = \frac{3 \cdot P}{2 \cdot \pi \cdot a^3} \cdot \left[-z \cdot \left\{ \frac{y \cdot N}{S} - \frac{y \cdot z \cdot H}{G^2 + H^2} \right\} \right] \quad (\text{B.56})$$

$$\tau_{zx,n} = \frac{3 \cdot P}{2 \cdot \pi \cdot a^3} \cdot \left[-z \cdot \left\{ \frac{x \cdot N}{S} - \frac{x \cdot z \cdot H}{G^2 + H^2} \right\} \right] \quad (\text{B.57})$$

When $r = 0$ the stresses in the contact are given by:

$$\sigma_{x,n} = \sigma_{y,n} = \frac{3 \cdot P}{2 \cdot \pi \cdot a^3} \cdot \left[(1 + \nu) \cdot \left(z \cdot \operatorname{atan}\left(\frac{a}{z}\right) - a \right) + \frac{a^3}{2 \cdot (a^2 + z^2)} \right] \quad (\text{B.58})$$

$$\sigma_{z,n} = \frac{3 \cdot P}{2 \cdot \pi \cdot a^3} \cdot \left[\frac{-a^3}{a^2 + z^2} \right] \quad (\text{B.59})$$

$$\tau_{xy,n} = \tau_{yz,n} = \tau_{zx,n} = 0 \quad (\text{B.60})$$

In the graph below (Fig. B.8) a contour map of the Von Mises yield parameter $\sqrt{J_2}$ is plotted along the centre plane of the contact $y = 0$.

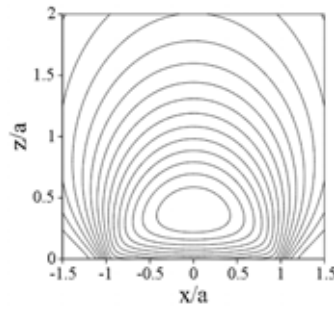


Fig. B.8: Sub-surface stress field in static contact.

B.2.1.2 Stresses due to the tangential load

Provided $r > 0$ the tangential components are :

$$\begin{aligned} \sigma_{x,t} = & \frac{3 \cdot Q}{2 \cdot \pi \cdot a^3} \cdot \left[-x \cdot \left(\frac{\nu}{4} + 1 \right) \cdot \phi + \frac{a \cdot x \cdot M}{r^4} \cdot \left\{ \left(\frac{3}{2} - \frac{2 \cdot x^2}{r^2} \right) \right. \right. \\ & \times \left(S \cdot \nu - 2 \cdot A \cdot \nu + z^2 \right) + \frac{x^2 \cdot z^2}{S} + \frac{7 \cdot \nu \cdot r^2}{4} - 2 \cdot \nu \cdot x^2 + r^2 \left. \right\} \\ & + \frac{x \cdot z \cdot N}{r^4} \cdot \left\{ \left(\frac{3}{2} - \frac{2 \cdot x^2}{r^2} \right) \cdot \left[-\frac{S \cdot (1-2 \cdot \nu)}{6} - \frac{A \cdot (1-2 \cdot \nu)}{3} - \frac{(z^2 + 3 \cdot a^2)}{2} \right] \right. \quad \text{(B.61)} \\ & \left. + \frac{a^2 \cdot x^2}{S} - \frac{\nu \cdot r^2}{4} - \frac{7 \cdot r^2}{4} \right\} + \frac{4 \cdot a^3 \cdot x \cdot z}{3 \cdot r^4} \cdot \left(\frac{3}{2} - \frac{2 \cdot x^2}{r^2} \right) \cdot (1-2 \cdot \nu) \left. \right] \end{aligned}$$

$$\begin{aligned} \sigma_{y,t} = & \frac{3 \cdot Q}{2 \cdot \pi \cdot a^3} \cdot \left[-\frac{3 \cdot \nu \cdot x \cdot \phi}{4} + \frac{a \cdot x \cdot M}{r^4} \cdot \left\{ \left(\frac{1}{2} - \frac{2 \cdot y^2}{r^2} \right) \right. \right. \\ & \times \left[\nu \cdot (S - 2 \cdot A + r^2) + z^2 \right] + \frac{y^2 \cdot z^2}{S} + \frac{3 \cdot \nu \cdot r^2}{4} \left. \right\} \\ & + \frac{x \cdot z \cdot N}{r^4} \cdot \left\{ \left(\frac{1}{2} - \frac{2 \cdot y^2}{r^2} \right) \cdot \left[-\frac{S \cdot (1-2 \cdot \nu)}{6} - \frac{A \cdot (1-2 \cdot \nu)}{3} - \frac{(z^2 + 3 \cdot a^2)}{2} \right] \right. \quad \text{(B.62)} \\ & \left. + \frac{a^2 \cdot y^2}{S} - \frac{3 \cdot \nu \cdot r^2}{4} - \frac{r^2}{4} \right\} + \frac{4 \cdot a^3 \cdot x \cdot z}{3 \cdot r^4} \cdot \left(\frac{1}{2} - \frac{2 \cdot y^2}{r^2} \right) \cdot (1-2 \cdot \nu) \left. \right] \end{aligned}$$

$$\sigma_{z,t} = \frac{3 \cdot Q}{2 \cdot \pi \cdot a^3} \cdot \left[\frac{z \cdot x \cdot N}{2 \cdot r^2} \cdot \left(1 - \frac{r^2 + z^2 + a^2}{S} \right) \right] \quad \text{(B.63)}$$

$$\begin{aligned}
\tau_{xy,t} = & \frac{3 \cdot Q}{2 \cdot \pi \cdot a^3} \cdot \left[\frac{y}{2} \cdot \left(\frac{\nu}{2} - 1 \right) \cdot \phi + \frac{a \cdot y \cdot M}{r^4} \cdot \left\{ \frac{x^2 \cdot z^2}{S} + \nu \cdot \left[(S - 2 \cdot A) \right. \right. \right. \\
& + \left. \left. \left. \left(\frac{1}{2} - \frac{2 \cdot x^2}{r^2} \right) - 2 \cdot x^2 + \frac{r^2}{4} \right] + \frac{r^2}{2} + z^2 \cdot \left(\frac{1}{2} - \frac{2 \cdot x^2}{r^2} \right) \right\} + \frac{y \cdot z \cdot N}{r^4} \cdot \right. \\
& \left. \left\{ \left(\frac{1}{2} - \frac{2 \cdot x^2}{r^2} \right) \cdot \left[(2 \cdot \nu - 1) \cdot \left(\frac{S}{6} + \frac{A}{3} \right) - \frac{z^2 + 3 \cdot a^2 + r^2}{2} \right] + \frac{r^2 \cdot \nu}{2} + \frac{a^2 \cdot x^2}{S} \right. \right. \\
& \left. \left. - \frac{y^2}{2} - \frac{3 \cdot x^2}{2} \right\} + \frac{4 \cdot a^3 \cdot y \cdot z}{3 \cdot r^4} \cdot \left(\frac{1}{2} - \frac{2 \cdot x^2}{r^2} \right) (1 - 2 \cdot \nu) \right] \quad (\text{B.64})
\end{aligned}$$

$$\begin{aligned}
\tau_{yz,t} = & \frac{3 \cdot Q}{2 \cdot \pi \cdot a^3} \cdot \frac{x \cdot y \cdot z}{2 \cdot r^4} \cdot \left[a \cdot M \cdot \left\{ \frac{1}{2} + \frac{1}{S} \cdot \left(\frac{z^2}{2} - \frac{3 \cdot a^2}{2} - \frac{r^2}{2} \right) \right\} \right. \\
& \left. + \frac{z \cdot N}{2} \cdot \left\{ -3 + \frac{1}{S} \cdot (5 \cdot a^2 + z^2 + r^2) \right\} \right] \quad (\text{B.65})
\end{aligned}$$

$$\begin{aligned}
\tau_{zx,t} = & \frac{3 \cdot Q}{2 \cdot \pi \cdot a^3} \cdot \left[\frac{3 \cdot z \cdot \phi}{2} + \frac{a \cdot z \cdot M}{r^2} \cdot \left\{ 1 + \frac{x^2}{r^2} - \frac{x^2}{S} \right\} \right. \\
& \left. + \frac{N}{r^2} \cdot \left\{ -\frac{3}{4} \cdot (S + 2 \cdot A) + z^2 - \frac{3}{4} \cdot a^2 - \frac{1}{4} \cdot r^2 + \frac{z^2}{2} \cdot \left(\frac{1}{2} - \frac{2 \cdot x^2}{r^2} \right) \right\} \right] \quad (\text{B.66})
\end{aligned}$$

And for $r = 0$:

$$\sigma_{x,t} = \sigma_{y,t} = \sigma_{z,t} = \tau_{xy,t} = \tau_{yz,t} = 0 \quad (\text{B.67})$$

and

$$\tau_{zx,t} = \frac{3 \cdot Q}{2 \cdot \pi \cdot a^3} \cdot \left[-a + \frac{3}{2} \cdot z \cdot \text{atan} \left(\frac{a}{z} \right) - \frac{a \cdot z^2}{2 \cdot (a^2 + z^2)} \right] \quad (\text{B.68})$$

B.2.1.3 Equivalent subsurface stress

The equivalent Von Mises stress parameter J_2 is defined as

$$J_2 = \frac{1}{6} \cdot \left[(\sigma_x - \sigma_y)^2 + (\sigma_y - \sigma_z)^2 + (\sigma_z - \sigma_x)^2 \right] + \tau_{xy}^2 + \tau_{yz}^2 + \tau_{zx}^2 \quad (\text{B.69})$$

in which the stresses are the summation of the normal and tangential components. In Fig. B.9 the equivalent Von Mises stress in the surface along the centre plane $y = 0$ is plotted.

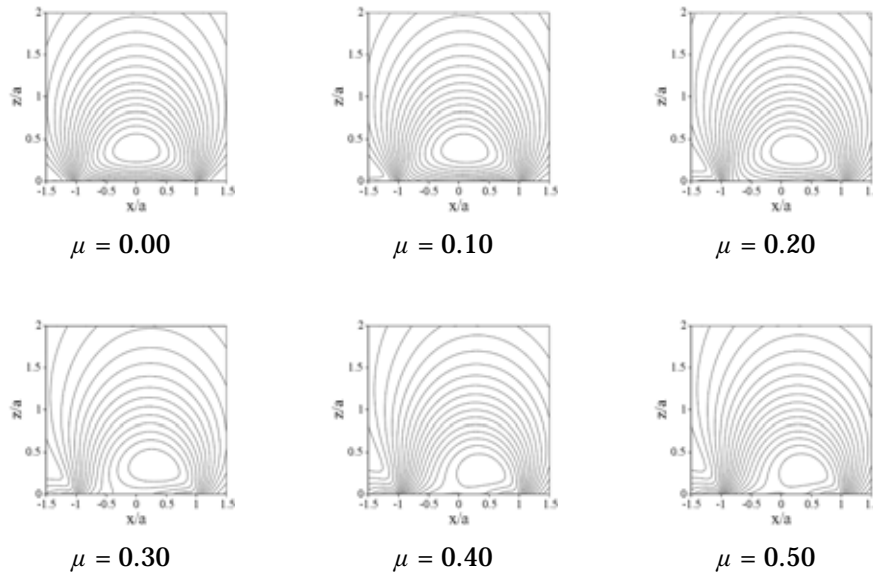


Fig. B.9: Sub-surface stress field in sliding contact.

B.3 Greenwood and Williamson parameters

In the statistical contact model as developed by Greenwood and Williamson [40], three surface parameters are required as input: the standard deviation of the summit heights σ , the summit density n , and the average summit radius R . These so-called Greenwood and Williamson parameters can be obtained from a surface height measurement. According to de Rooij [26], summits are defined as points $z_{x,y}$ in a surface height measurement that are higher than their eight neighbouring points.

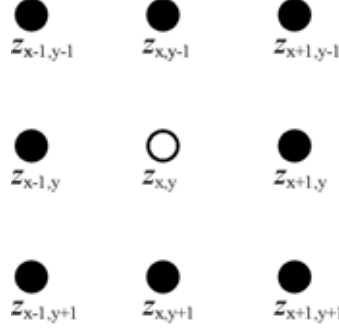


Fig. B.10: Nine point summit definition.

The summit density n equals the number of summits C divided by the area of the surface height measurement A_n .

The summit height data usually shows a near-Gaussian distribution. The standard deviation of the summit heights is calculated from the summits in the surface micro-geometry using eq. (B.70) with d_s the average summit height and C the number of summits in the measured surface micro-geometry.

$$\sigma = \frac{1}{C} \cdot \sum_{i=1}^C (s - d_s)^2 \quad (\text{B.70})$$

The radius of each summit is defined as the reciprocal of the summit curvature, which is determined by finite differences of the height of the summit and the two neighbouring points:

$$R_x = \kappa_x^{-1} = \left(\frac{z_{x-1,y} - 2 \cdot z_{x,y} + z_{x+1,y}}{p_x^2} \right)^{-1} \quad (\text{B.71})$$

$$R_y = \kappa_y^{-1} = \left(\frac{z_{x,y-1} - 2 \cdot z_{x,y} + z_{x,y+1}}{p_y^2} \right)^{-1} \quad (\text{B.72})$$

Appendix C

Photographic impressions of the experimental set-ups

C.1 SEM tribo-system

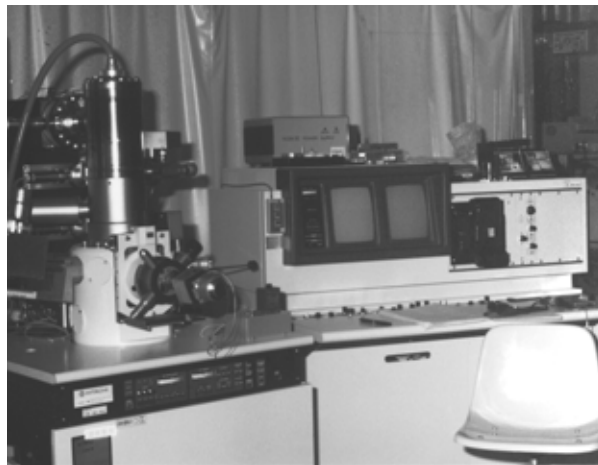


Fig. C.1: Scanning Electron Microscope.

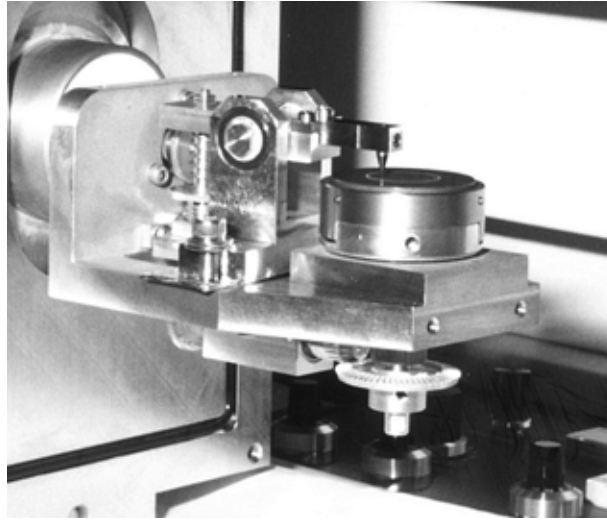


Fig. C.2: SEM Tribo-system.

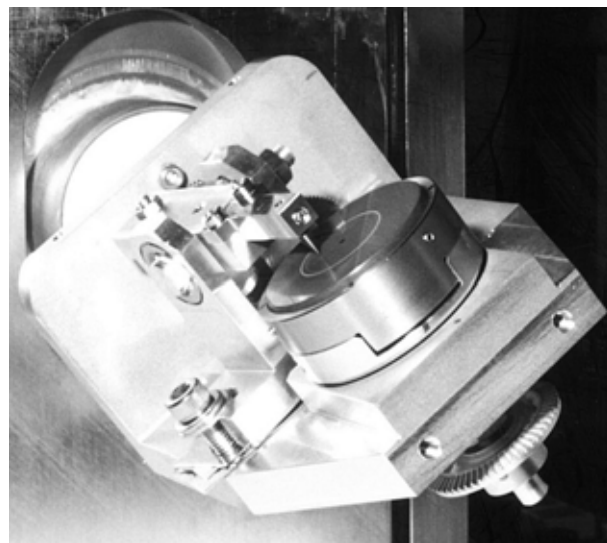


Fig. C.3: SEM Tribo-system.

C.2 Deep drawing simulator



Fig. C.4: Deep drawing simulator - overview of the set-up.

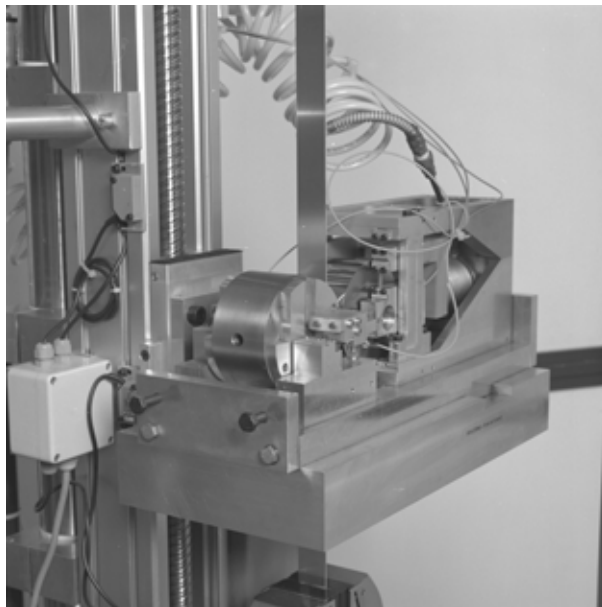


Fig. C.5: Deep drawing simulator - tribo-tester.

References

- [1] Abbott, E.J. and Firestone, F.A., 1933, Specifying Surface Quality, *Mechanical Engineering*, Vol. 55, pp. 569 - 572.
- [2] Alfredsson, B., and Cadario, A., 2003, Discussion of G.M. Hamilton, Explicit Equations for the Stresses Beneath a Sliding Spherical Contact, *Proceedings of the Institution of Mechanical Engineers*, Vol. 217C, pp. 281.
- [3] Andreasen, J.L., Bay, N. and De Chiffre, L., 1998, Quantification of Galling in Sheet Metal Forming by Surface Topography Characterisation, *International Journal of Machine Tools and Manufacture*, Vol. 38, pp. 503 - 510.
- [4] Archard, J.F., 1953, Contact and Rubbing of Flat Surfaces. *Journal of Applied Physics*, Vol. 24, pp. 981 - 988.
- [5] Bhushan, B., 1996, Contact Mechanics of Rough Surfaces in Tribology: Single Asperity Contact, *Applied Mechanics Reviews*, Vol. 49, no. 5, pp. 275 - 298.
- [6] Bhushan, B., 1998, Contact Mechanics of Rough Surfaces in Tribology: Multiple Asperity Contact, *Tribology Letters*, Vol. 4, pp. 1 - 35.
- [7] Bhushan, B., 1999, *Handbook of Micro/Nano Tribology*, Second Edition, CRC Press, Boca Raton, USA, ISBN 0-8493-8402-8.
- [8] Black, A.J., Kopalinsky, E.M. and Oxley, P.L.B., 1988, An Investigation of the Different Regimes of Deformation Which Can Occur When a Hard Wedge Slides Over a Soft Surface: The Influence of Wedge Angle, Lubrication and Prior Plastic Working of the Surface, *Wear*, Vol. 123, pp. 97 - 114.
- [9] Black, A.J., Kopalinsky, E.M. and Oxley, P.L.B., 1992, An Investigation of the Interaction of Model Asperities of Similar Hardness, *Wear*, Vol. 153, pp. 245 - 261.

- [10] Bressan, J.D., Genin, G.M. and Williams, J.A., 1998, The Influence of Pressure, Boundary Film Shear Strength and Elasticity on the Friction Between a Hard Asperity and a Deforming Softer Surface, Proc. 25th Leeds-Lyon Symposium on Tribology, Elsevier Tribology Series 36, pp. 79 - 90.
- [11] Bucaille J.L., Felder, E. and Hochstetter, G., 2001, Mechanical Analysis of the Scratch Test on Elastic and Perfectly Plastic Materials with the Three-Dimensional Finite Element Modeling, Wear, Vol. 249, pp. 422 - 432.
- [12] Burnett, P.J. and Rickerby, D.S., 1987, The Mechanical Properties of Wear-Resistant Coatings I: Modelling of Hardness Behaviour, Thin Solid Films, Vol. 148, pp. 41 - 50.
- [13] Burnett, P.J. and Rickerby, D.S., 1987, The Mechanical Properties of Wear-Resistant Coatings II: Experimental Studies and Interpretation of Hardness, Thin Solid Films, Vol. 148, pp. 51 - 65.
- [14] Busquet, M. and Torrance, A.A., 1999, Investigation of Surface Deformation and Friction when a Hard Cylindrical Asperity Slides Over a Soft Smooth Surface, Proc. 25th Leeds-Lyon Symposium on Tribology, Elsevier Tribology Series 37, pp. 101 - 109.
- [15] Busquet, M. and Torrance, A.A., 2000, A Numerical Slipline Field for the Sliding Cylinder Problem, Wear, Vol. 241, pp. 86 - 98.
- [16] Butnariu, E., 2003, Surface Force Apparatus, University of Twente, The Netherlands, Dept. of Mechanical Engineering, Tribology Group report # TR-03-2266.
- [17] Challen, J.M. and Oxley, P.L.B., 1979, An Explanation of the Different Regimes of Friction and Wear Using Asperity Deformation Models, Wear, Vol. 53, pp. 229 - 243.
- [18] Challen, J.M., Oxley, P.L.B. and Boyle, E.D., 1983, The Effect of Strain hardening on the Critical Angle for Abrasive (Chip Formation) Wear, Wear, Vol. 88, pp. 1 - 12.
- [19] Challen, J.M. and Oxley, P.L.B., 1984, Slip-line Fields for Explaining the Mechanics of Polishing and Related Processes, International Journal of Mechanical Sciences, Vol. 26, No. 6 - 8, pp. 403 - 418.

- [20] Challen, J.M., McLean, L.J. and Oxley, P.L.B., 1984, Plastic Deformation of a Metal Surface in Sliding Contact with a Hard Wedge: Its Relation to Friction and Wear, Proceedings of the Royal Society of London Series A, Vol. 394, pp. 161 - 181.
- [21] Challen, J.M. and Oxley, P.L.B., 1984, A Slip Line Field Analysis of the Transition from Local Asperity Contact to Full Contact in Metallic Sliding Friction, Wear, Vol. 100, pp. 171 - 193.
- [22] Challen, J.M., Oxley, P.L.B. and Hockenhull, B.S., 1986, Prediction of Archard's Wear Coefficient for Metallic Sliding Friction Assuming a Low Cycle Fatigue Wear Mechanism, Wear, Vol. 111, pp. 275 - 288.
- [23] Chang, W.R., Etsion, I. and Bogy, D.B., 1987, An Elastic-Plastic Model for the Contact of Rough Surfaces, Journal of Tribology, Vol. 109, pp. 257 - 263.
- [24] Czichos, H., 1978, Tribology – A Systems Approach to the Science and Technology of Friction, Lubrication and Wear, Elsevier, Amsterdam, ISBN 0 44 41676 5.
- [25] de Pellegrin, D.V. and Stachowiak, G.W. 2004, Evaluating the Role of Particle Distribution and Shape in Two-Body Abrasion by Statistical Simulation, Tribology International, Vol. 37, pp. 255 - 270.
- [26] de Rooij, M.B., 1998, Tribological Aspects of Unlubricated Deepdrawing Processes, PhD thesis, University of Twente, Enschede, The Netherlands, ISBN 90 365 1218 2.
- [27] Dillingh, E.C., 2004, Private Communication.
- [28] DIN 4768, 1999, Ermittlung der Rauheitskenngrößen R_a , R_z , R_{max} mit elektrischen Tastschnittgeräten, Begriffe, Meßbedingungen, Beuth Verlag, Berlin, Germany.
- [29] DIN 50320, 1979, Verschleiß - Begriffe, Systemanalyse von Verschleißvorgängen, Gliederung des Verschleißgebietes, Beuth Verlag, Berlin, Germany.
- [30] DIN 50322, 1986, Verschleiß - Kategorien der Verschleißprüfung, Beuth Verlag, Berlin, Germany.
- [31] DIN EN 10130, 1998, Kaltgewaltzte Flacherzeugnisse aus weichen Stählen zum Kaltomformen - Technische Lieferbedingungen, Beuth Verlag, Berlin, Germany.

- [32] DIN EN 1563, 1997, Gießereiwesen - Gußeisen mit Kugelgraphit, Beuth Verlag, Berlin, Germany.
- [33] Dowson, D., 1998, History of Tribology, Second Edition, Professional Engineering Publishing, United Kingdom, ISBN 1 86058 070 X.
- [34] Emmens, W.C., 1997, Tribology of Flat Contacts and its Application in Deep Drawing, PhD thesis, University of Twente, Enschede, The Netherlands, ISBN 90 3651028 7.
- [35] Eriksen, M., and Wanheim, T., 1997, Wear Optimisation in Deep Drawing, in: K. Dohda, T. Nakamura and W.R.D. Wilson (ed), Proceedings of the 1st international Conference on Tribology in Manufacturing Processes '97 Gifu, Japan, pp. 128 - 133.
- [36] Fallböhmer, P., Altan, T., Tönshoff H.-K. and Nakagawa, T., 1996, Survey of the Die and Mold Manufacturing Industry, Journal of Processing Technology, Vol. 59, pp. 158 - 168.
- [37] Francis, H.A., 1976, Phenomenological analysis of plastic spherical indentation, J. Eng. Mater. Technol., Vol. 98, pp. 272 - 281.
- [38] Gao, H., Chiu, C.H. and Lee, J., 1992, Elastic Contact Versus Indentation Modelling of Multi-Layered Materials, International Journal of Solids and Structures, Vol. 29, No. 20, pp. 2471 - 2492.
- [39] Greenwood, J.A., 1984, A Unified Theory of Surface Roughness, Proceedings of the Royal Society of London Series A, Vol. 393, pp. 133 - 157.
- [40] Greenwood, J.A., and Williamson, J.B.P., 1966, Contact of Nominally Flat Surfaces, Proceedings of the Royal Society of London Series A, Vol. 295, pp. 300 - 319.
- [41] Greenwood, J.A. and Wu, J.J., 2001, Surface Roughness and Contact: An Apology, Meccanica, Vol. 36, pp. 617-630.
- [42] Halling, J. and Nuri, K.A., 1991, Elastic/plastic Contact of Surfaces Considering Ellipsoidal Asperities of Work-Hardening Multi-Phase Materials, Tribology International, Vol. 24, No. 5, pp. 311 - 319.
- [43] Hamilton, G.M., 1983, Explicit Equations for the Stresses Beneath a Sliding Spherical Contact, Proceedings of the Institution of Mechanical Engineers, Vol. 197C, pp. 53 - 59.

- [44] Hamilton, G.M., 1983, Erratum to Explicit Equations for the Stresses Beneath a Sliding Spherical Contact, Proceedings of the Institution of Mechanical Engineers, Vol. 197C, pp. 282.
- [45] Hamilton, G.M. and Goodman, L.E., 1966, The Stress Field Created by a Sliding Circular Contact, Journal of Applied Mechanics, Vol. 88, pp. 371 - 376.
- [46] Handzel-Powierza, Z., Klimczak, T. and Polijaniuk, A., 1992, On the Experimental Verification of the Greenwood-Williamson Model for the Contact of Rough Surfaces, Wear, Vol. 154, pp. 115 - 124.
- [47] Hertz, H., 1881, Über die Berührung fester elastischer Körper, Journal für die reine und angewandte Mathematik, Vol. 92, pp. 156 - 171.
- [48] Hokkirigawa, K. and Kato, K., 1988, An Experimental and Theoretical Investigation of Ploughing, Cutting and Wedge Formation During Abrasive Wear, Tribology International, Vol. 21, No. 1, pp. 51 - 57.
- [49] Hokkirigawa, K. and Kato, K., 1989, Theoretical Estimation of Abrasive Wear Resistance Based on Microscopic Wear Mechanism, Proceedings of the 7th International Conference on Wear of Materials, ed. Ludema, K.C., American Society of Mechanical Engineers, pp. 1 - 8.
- [50] Hokkirigawa, K., Kato, K. and Li, Z.Z., 1988, The Effect of Hardness on the Transition of the Abrasive Wear Mechanism of Steels, Wear, Vol. 123, pp. 241 - 251.
- [51] Horng, J.H., 1998, An Elliptic Elastic-Plastic Asperity Microcontact Model for Rough Surfaces, Journal of Tribology, Vol. 120, pp. 82 - 88.
- [52] ISO 13919-1, 1996, Welding - Electron and laser-beam welded joints - Guidance on quality levels for imperfections - part 1: Steel.
- [53] Jacobson, S., Wallen, P. and Hogmark, S., 1988, Fundamental Aspects of Abrasive Wear Studied by a New Numerical Simulation Model, Wear, Vol. 123, pp. 207 - 223.
- [54] Jamari, 2004, Private Communication.
- [55] Jardret, V., Zahouani, H., Loubet, J.L. and Mathia, T.G., 1998, Understanding and Quantification of Elastic and Plastic Deformation During a Scratch Test, Wear, Vol. 218, pp. 8 - 14.

- [56] Jiang, J., Sheng, F. and Ren, F., 1997, Modelling of Two-Body Abrasive Wear Under Multiple Contact Conditions, *Wear*, Vol. 217, Iss. 1, pp. 35 - 45.
- [57] Jiang, J. and Arnell, R.D., 1998, The Dependence of the Fraction of Material Removed on the Degree of Penetration in Single Particle Abrasion of Ductile Materials, *Journal of Physics D – Applied Physics*, Vol. 31, pp. 1163 - 1167.
- [58] Johnson, K.L., 1985, *Contact Mechanics*, Cambridge University Press, Cambridge, United Kingdom, ISBN 0 521 34796 3.
- [59] Jönsson, B. and Hogmark, S., 1984, Hardness Measurements of Thin Films, *Thin Solid Films*, Vol. 114, pp. 257 - 269.
- [60] Kataoka, S., Murakawa, M., Aizawa, T. and Ike, H., 2004, Tribology of Dry Deep-Drawing of Various Metal Sheets with Use of Ceramics Tools, *Wear*, Vol. 117 - 178, pp. 582 - 590.
- [61] Kato, K. and Hokkirigawa, K., 1985, Abrasive Wear Diagram, *Proceedings Eurotrib '85*, September 9 -12 1985, Elsevier, Amsterdam.
- [62] Kato, K., 1997, Abrasive Wear of Metals, *Tribology International*, Vol. 30, pp. 333 - 338.
- [63] Kato, K., Diao, D.F., and Tsutsumi, M., 1991, The Wear Mechanism of Ceramic Coating Film in Repeated Sliding Friction, *Proceedings of the 8th International Conference on Wear of Materials*, ed. Ludema, K.C., American Society of Mechanical Engineers, pp. 243 - 248.
- [64] Kayaba, T., Hokkirigawa, K., and Kato, K., 1986, Analysis of the Abrasive Wear Mechanism by Successive Observations of Wear Processes in a Scanning Electron Microscope, *Wear*, Vol. 110, pp. 419 - 430.
- [65] Kennedy, F.E., Lidhagen, D., Erdemir, A., Woodford, J.B. and Kato, T., 2003, Tribological Behavior of Hard Carbon Coatings on Steel Substrates, *Wear*, Vol. 255, Iss. 7-12, pp. 854 - 858.
- [66] Kitsunai, H., Kato, K., Hokkirigawa, K. and Inoue, H., 1990, The Transitions between Microscopic Wear Modes during Repeated Sliding Friction Observed by a Scanning Electron Microscope Tribosystem, *Wear*, Vol. 135, pp. 237 - 249.

- [67] Klischat, S., 1996, Alle Straßen führen nach Rom, die Via Appia und andere Römerstraßen,
<http://www.klischat.net/onlinepub/referate/rom/rom.htm>.
- [68] Kral, E.R. and Komvopoulos, K., 1997, Three-Dimensional Finite Element Analysis of Subsurface Stress and Strain Fields Due to Sliding Contact on an Elastic-Plastic Layered Medium, *Journal of Tribology*, Vol. 119, pp. 332 - 341.
- [69] Landels, J.G., 2000, *Engineering in the Ancient World*, Second Edition, Constable, United Kingdom, ISBN 0 09 480490 7.
- [70] Love, A.E.H., 1929, The Stress Produced in a Semi-Infinite Solid by Pressure on Part of the Boundary, *Philosophical Transactions of the Royal Society of London Series A*, Vol. 228, pp. 377 - 420.
- [71] Majumdar, A. and Bhushan, B., 1991, Fractal Model of Elastic-Plastic Contact between Rough Surfaces, *Journal of Tribology*, Vol. 113, pp. 1 - 11.
- [72] Masen, M.A. and de Rooij, M.B., 2002, Abrasive Wear between Rough Surfaces in Deep Drawing, *Wear*, Vol. 256, pp. 639 - 646.
- [73] Masen, M.A., de Rooij, M.B. and Schipper, D.J., 2003, Micro-Contact Based Modelling of Abrasive Wear, *Proceedings International Conference on Erosive and Abrasive Wear ICEAW II*, Cambridge, United Kingdom.
- [74] Malzbender, J., de With, G. and den Toonder, J.M.J., 2000, Determination of the Elastic Modulus and Hardness of Sol-Gel Coatings on Glass: Influence of Indenter Geometry, *Thin Solid Films*, Vol. 372, pp. 134 - 143.
- [75] McCool, J.I., 1986, Comparison of Models for the Contact of Rough Surfaces, *Wear*, Vol. 107, pp. 37 - 60.
- [76] Metselaar, H.S.C., 2001, Thermally Induced Wear Transition in Ceramics, PhD thesis, University of Twente, Enschede, The Netherlands, ISBN 90 365 1599 8.
- [77] Michler, J. and Blank, E., 2001, Analysis of Coating Fracture and Substrate Plasticity Induced by Spherical Indentors: Diamond and Diamond-Like Carbon Layers on Steel Substrates, *Thin Solid Films*, Vol. 381, pp. 199 - 134.

- [78] Mitterer, C., Holler, F., Reitberger, D., Badisch, E., Stoiber, M., Lugmair, C., Nöbauer, R., Müller, Th. and Kullmer, R., 2003, Industrial Applications of PACVD Hard Coatings, Surface and Coatings Technology, Vol. 163 – 164, pp. 716 - 722.
- [79] Moes, H., 2000, Lubrication and Beyond – University of Twente Lecture Notes code 115531, University of Twente, Enschede, The Netherlands.
- [80] Murakawa, M., Koga, N., Watanabe, S. and Takeuchi, S., 1998, Tribological Behavior of Amorphous Hard Carbon Films Against Zinc-Plated Steel Sheets, Surface and Coatings Technology, Vol. 108 - 109, pp. 425 - 430.
- [81] Müller, H. and Sladojevic, J., 2001, Rapid Tooling Approaches for Small Lot Production of Sheet-Metal Parts, Journal of Materials Processing Technology, Vol. 115, pp. 97 - 103.
- [82] Nakagawa, T., 2000, Advances in Prototype and Low Volume Sheet Forming and Tooling, Journal of Materials Processing Technology, Vol. 98, pp. 244 - 250.
- [83] Ogilvy, J.A., 1992, Numerical Simulation of Elastic-Plastic Contact Between Anisotropic Rough Surfaces, Journal of Physics D - Applied Physics, Vol. 25, pp. 1798 - 1809.
- [84] O'Sullivan, T.C. and King R.B., 1988, Sliding Contact Stress Field due to a Spherical Indenter on a Layered Elastic Half-Space, Journal of Tribology, Vol. 110, pp. 235 - 240.
- [85] Pesch, P., Sattel, S., Woestmann, S., Masarczyk, P., Herden K., Stucky, T., Martens, A., Ulrich, S. and Holleck, H., 2003, Performance of Hard Coated Steel Tools for Steel Sheet Drawing, Surface and Coatings Technology, Vol. 163 - 164, pp. 739 - 746.
- [86] Puchi-Cabrera, E.S., 2002, A New Model for the Computation of the Composite Hardness of Coated Dystems, Surface and Coatings Technology, Vol. 160, Iss. 2 - 3, pp. 177 - 186.
- [87] Pullen, J. and Williamson, J.B.P., 1972, On the Plastic Contact of Rough Surfaces, Proceedings of the Royal Society of London Series, Vol. 327, pp. 159 - 173.
- [88] Ravikiran, A. and Jahanmir, S., 2001, Effect of Contact Pressure and Load on Wear of Alumina, Wear, Vol. 251, Iss. 1-12, pp. 980 - 984.

- [89] Reussner, H., 1977, Druckflächenbelastung und Oberflächenverschiebung im Wälzcontact von Rotationskörpern, PhD thesis, University of Karlsruhe, Germany.
- [90] Schedin, E., 1994, Galling Mechanisms in Sheet Forming Operations, Wear, Vol. 179, pp. 123 - 128.
- [91] Schedin, E. and Lehtinen, B., 1993, Galling Mechanisms in Lubricated Systems: A Study of Sheet Metal Forming, Wear, Vol. 170, pp. 119 - 130.
- [92] Schey, J.A., 1983, Tribology in Metalworking – Friction, Lubrication and Wear, American Society for Metals, ISBN 0 87170 155 3.
- [93] Schipper, D.J., 1988, Transitions in the Lubrication of Concentrated Contacts, PhD thesis, University of Twente, Enschede, The Netherlands, ISBN 90 9002448 4.
- [94] Singerling, B.F.S., 2002, De PATAT, MSc Thesis, University of Twente, The Netherlands, Dept. of Mechanical Engineering, Tribology Group report # TR-02-2244.
- [95] Sniekers, R.J.J.M., 1996, Friction in Deep Drawing, PhD thesis, Eindhoven Technical University, Eindhoven, The Netherlands, ISBN 90 386 0417 3.
- [96] Stillwell, N.A. and Tabor, D., 1961, Elastic Recovery of Conical Indentations, Proceedings of the Physical Society of London, Vol. 78, pp. 169 - 178.
- [97] Street, A. and Alexander, W., 1994, Metals in the Service of Man, 10th edition, Penguin, London, England, ISBN 0 14 014889 2.
- [98] Tabor, D., 1951, The Hardness of Metals, Clarendon Press, Oxford, United Kingdom.
- [99] ter Haar, R., 1996, Friction in Sheet Metal Forming, PhD thesis, University of Twente, Enschede, The Netherlands, ISBN 90 9009296 X.
- [100] Torrance, A.A., 1981, An Explanation of the Hardness Differential Needed for Abrasion, Wear, Vol. 68, pp. 263 - 266.
- [101] Torrance, A.A. and d'Art, J.M., 1986, A Study of Lubricated Abrasive Wear, Wear, Vol. 110, pp. 49 - 59.
- [102] Torrance, A.A., 1990, The Correlation of Process Parameters in Grinding, Wear, Vol. 139, Iss. 2, pp. 383 - 401.

- [103] Tuck, J.R., Korsunsky, A.M. and Bull, S.J., 2000, Modelling of the hardness of electroplated nickel coatings on copper substrates, *Surface and Coatings Technology*, Vol. 127, Iss. 1, pp. 1 - 8.
- [104] ULSAB-AVC, 2002, Advanced Vehicle Concepts Overview Report, Safe, affordable, fuel efficient vehicle concepts for the 21st century designed in steel,
http://www.autosteel.org/pdfs/avc_overview_rpt_complete.pdf.
- [105] ULSAC, 2001, UltraLight Steel Auto Closures Overview Report, An overview of the design, materials, manufacturing, structural performance and economic analysis of the UltraLight Steel Auto Closures (ULSAC) Program,
http://www.autosteel.org/pdfs/ulsac_overview_may2001.pdf.
- [106] van der Heide, E., Burlat, M. and Bolt, P.J., 2001 Wear of Alternative Forming Tool Materials due to Sliding Contact with Zinc Coated Steel Sheet in Press Operations, In: *Proceedings Euromat 2001 Conference*, Associazione Italiana di Metallurgia - Milano, Rimini, Italy, ISBN 88 85298 39 7.
- [107] van der Heide, E., Burlat, M., Bolt, P.J. and Schipper, D.J., 2001, Wear of Soft Tool Materials in Sliding Contact with Zinc Coated Steel Sheet, *Journal of Materials Processing Technology*, Vol. 141, Iss. 2, pp. 197 - 201.
- [108] van der Heide, E., Huis in 't Veld, A.J. and Schipper, D.J., 2001, The Effect of Lubricant Selection on Galling in a Model Wear Test, *Wear*, Vol. 251, pp. 973 - 979.
- [109] van der Heide, E., 2002, Lubricant Failure in Sheet Metal Forming Processes, PhD thesis, University of Twente, Enschede, The Netherlands, ISBN 90 365 1724 9.
- [110] van der Heide, E. and Schipper, D.J., 2004, Galling Initiation due to Frictional Heating, *Wear*, Vol. 254, pp. 1127 - 1131.
- [111] Vermeulen, M., 1997, Effect of Pre-Welded Blanks on the Wear of Deep Drawing Tools, Abstracts of papers, 1st World Tribology Congress, London, pp. 333., ISBN 1 86058 109 9.
- [112] Visscher, H., 2001, On the friction of thin film rigid disks, PhD Thesis, University of Twente, Enschede, The Netherlands, ISBN 90 365 1574 2.

- [113] Westeneng, J.D., 2001, Modelling of Contact and Friction in Deep Drawing Processes, PhD thesis, University of Twente, Enschede, The Netherlands, ISBN 90 365 1549 1.
- [114] Whitehouse, D.J. and Archard, J.F., 1970, The Properties of Random Surfaces of Significance in their Contact, Proceedings of the Royal Society of London Series A, Vol. 316, pp. 97 - 121.
- [115] Williams, J.A., 1996, Analytical Models of Scratch Hardness, Tribology International, Vol. 29, No. 8, pp. 675 – 694.
- [116] Xie, Y. and Williams, J.A., 1993, The Generation of Worn Surfaces by the Repeated Interaction of Parallel Grooves, Wear, Vol. 162 - 164, pp. 864 - 872.
- [117] Xie, Y. and Williams, J.A., 1996, The Prediction of Friction and Wear when a Soft Surface Slides Against a Harder Rough Surface, Wear, Vol. 196, Iss. 1 - 2, pp. 21 - 34.
- [118] Zhao, Y., Maietta, D.M. and Chang, L., 2000, An Asperity Microcontact Model Incorporating the Transition From Elastic Deformation to Fully Plastic Flow, Journal of Tribology, Vol. 122, pp. 86 - 93.
- [119] Zhang, S., Hodgson, P.D., Duncan, J.L., Cardew-Hill, M.J. and Kalyanasundaram, S., 2002, Effect of Membrane Stress on Surface Roughness Changes in Sheet Forming, Wear, Vol. 253, pp. 610 - 617.
- [120] Zum Gahr, K.-H., 1987, Microstructure and Wear of Materials, Elsevier, Amsterdam, ISBN 0 444 42754 6.
- [121] Zum Gahr, K.-H., 1988, Modelling of two-Body Abrasive Wear, Wear, Vol. 124, pp. 87 - 108.

Index

Abrasion, low speed	62	Deterministic model	85
Abrasive wear 2, 7, 22, 101, 127, 129		Diamond like carbon.....	13
three body.....	22	Duplex layer.....	75
two body.....	22	Egg-shell phenomenon	13, 72
Abrasive wear mode map	57	Elasto-hydrodynamic... see Lubrication	
Abrasive wear model	123	Elastoplastic recovery.....	32
Adhesive wear	22	Electrochemical deposition.....	13
Aluminium sheet	5	Equivalent stress	154
Archard wear coefficient.....	105	Flaking	65
Asperity	28, 51, 87	Friction	19
cone	32, 137	Full film.....see Lubrication'	
elliptic.....	28, 36, 60, 89, 140	Galvanealed sheet	6
equivalent.....	88, 107	Greenwood and Williamson	
paraboloid.....	36, 142	model	84
elliptic.....	28, 41, 60, 89, 147	parameters	91
representative	88	Hard surface layer	51, 81
representing	107	Hardness	46, 88, 105
Asperity interaction.....	89	Hertz theory	142
Attack angle	23	Hot rolled sheet.....	5
Boundary	see Lubrication	Hybrid layer	75
Boussinesq.....	137	Hydrodynamic..... see Lubrication	
Chapter layout	9	In-situ wear experiment.....	65
Chemical vapour deposition.....	7	Laser cladding.....	14
Chip formation.....	67	Layered surface.....	44
Chipping.....	65	Load bearing capacity.....	105
Chromium nitride	13	Low cycle fatigue.....	61
Cladding	see Laser cladding	Lubricant.....	4, 15
Contact	16	Lubrication.....	19
asperity.....	27, 124, 127	boundary	20
dynamic	28	elasto-hydrodynamic	20
rough surface.....	126, 128	full film	20
sliding.....	28, 47, 50, 128, 152	hydrodynamic.....	20
static	29, 127, 137	micro-EHL.....	21
Contact model	123	micro-PHL.....	21
Deep drawing	3, 24, 25, 109	mixed	20
Deep drawing simulator.....	109	plasto-hydrodynamic	20
Deformation		Metal forming	129
elastic.....	30	Metal-carbon	13
elastoplastic.....	30	Micro-contact.....	18, 27, 85, 87, 107
mode.....	48	Mixed	see Lubrication
mode transition	38, 43	Nodular cast iron	5
modes.....	30	Pac-man.....	32
plastic	30	Physical vapour deposition	7, 13
Degree of penetration	57, 101	Plasto-hydrodynamic... see Lubrication	
Degree of wear	58, 67, 69	Pompeii.....	1
Delamination.....	21		

Pre-welded blank	6	Tailor welded blank ...	14, 109, 127, 129
Random process theory	93	Tailored blank	6
Real surface	83	Titanium nitride.....	13
Road wear	1	Tool	5, 12, 117
Roughness orientation	104, 108	life	4, 7
SEM tribo-system.....	62	Tribochemical wear.....	21
Shear tongue	65	Tribological system	8, 11, 26
Sheet-metal forming	2	Tribology.....	11, 16
Slip-line model.....	54	Tribometer	62
Stribeck diagram.....	19	Unit-event.....	107
Subsurface stress	47	Von Mises stress	39, 47, 51, 154
Surface deformation index.....	99	Wear.....	21
Surface fatigue wear	21	asperity	125, 128
Surface layer.....	7, 51	single asperity	53
Surface layers.....	12, 105, 108	Wear rate, specific.....	103, 106
Surface micro-geometry	108	Wear scar.....	54
Surface roughness	16	Weld	6, 14, 115
Systems approach	15	Young's modulus	44
Systems envelop.....	15		